

# Multifunctional Composite Interphase

Dem Fachbereich Maschinenwesen  
an der Technischen Universität Dresden  
zur  
Erlangung des Grades eines Doktor-Ingenieurs  
(Dr.-Ing.)  
eingereichte

D i s s e r t a t i o n

vorgelegt von

Jie Zhang

geboren am 05.02.1982 in V. R. China

Gutachter: Prof. Dr. rer. nat. habil. G. HEINRICH  
Prof. Dr.-Ing. habil. Dipl.-Wirt. Ing. C. CHERIF

Tag der Einreichung: 07.06.2012





## Acknowledgement

Firstly, I would like to express my gratitude to my supervisors, Prof. Dr. rer. nat. habil. Gert Heinrich and Prof. Dr.-Ing. habil. Edith Mäder for their guidance and valuable suggestions during the last years and for being always supportive, kind and understanding. They offer a free scientific platform and many chances of communication for me, which help me to search my interesting in scientific research. Additionally, I deeply appreciate their patience, tolerance and encouragement throughout my PH.D study.

I would like to thank the members of my dissertation defence committee and Prof. Dr.-Ing. habil. Dipl.-Wirt. Ing. Chokri Cherif as the second referee for my works and Doctoral Dissertation. Thanks for his kind support and professional advices.

I am also specially thankful to Dr. Shang-lin Gao for many helpful suggestions about my research. He is always generously sharing his knowledge and experience with me. For my every publication, he took many time in advising and modifying. He taught me a positive scientific attitude to meet various problem.

I would like to thank Dr. Jian-wen Liu for helping me to do many tensile tests and Dr. Rong-chuan Zhuang for helping me to analysis chemical reaction. They always patiently discussed with me and offered the useful suggestions.

Special thanks go to Dr. Rüdiger Hässler and Dr. Scheffler Christina for DSC measurements as well as Dr. Mikhail Malanin for FTIR measurement. Ms. Teresa Förster, thank you for your helps in SEM measurements. Many thanks go to Mrs. Steffi Pressler and Ms. Alma Rothe for helps in pull-out measurement.

I would like to convey my sincere thanks to Dr. Julius Rausch for help in learning the Germany cultures. He offered many practice suggestions and supports to my life in Dresden.

Many of colleagues in our institute helped me a lot either in my study or in my life in Dresden. Herein, I would like to express my thanks to them, especially Mrs. Gudrun Schwarz, Mrs. Rosemarie Plonka, Dr. Peng-cheng Ma, Prof. De-yi Wang, Mrs. Kalaivani Subramaniam. I would like to thank all colleagues for their kind helpfulness.

I am grateful to my husband, my parents, who have been waiting for me without any complaints. They are a great source of strength all through this work during the time far from home.

Finally, I am grateful for the fellowship from the China Scholarship Council (CSC),

while I would like to thank the German Research Foundation (DFG) for funding within priority program SPP 1369 “Polymer-Solid Contacts: Interfaces and Interphases” (C7).

## Eidesstattliche Erklärung

Hiermit versichere ich, dass ich die vorliegende Arbeit ohne unzulässige Hilfe Dritter und ohne Benutzung anderer als der angegebenen Hilfsmittel angefertigt habe; die aus fremden Quellen direkt oder indirekt übernommenen Gedanken sind als solche kenntlich gemacht. Die Arbeit wurde bisher weder im Inland noch im Ausland in gleicher oder ähnlicher Form einer anderen Prüfungsbehörde vorgelegt

Dresden, den June 7, 2012



## Abbreviation

---

AFM	Atomic force microscopy
ARG	Alkali-resistant glass
ASTM	American Society for Testing and Materials
CNT/CNTs	Carbon nanotube/Carbon nanotubes
CVD	Chemical vapour deposition
DC	Direct current
DLVO	Derjaguin-Landau-Verwey-Overbeek
DGEBA	Diglycidyl ether of bisphenol-A
DMTA	Dynamic mechanical thermal analyzer
DSC	Dynamic scanning calorimetry
EFM	Electric Force Microscopy
EPD	Electrophoretic deposition
FRP	Fibre reinforced plastic
FTIR	Fourier transform infrared spectroscopy
GF	Strain sensitivity factor (or Gauge factor)
GFRP	Glass fibre reinforce plastic
Glymo	3-glycidyloxypropyltrimethoxysilane
ILSS	Interlaminar shear strength
IFS	Interface frictional strength
IFSS	Interfacial shear strength
IR	Infrared light
MDSC	Modulated differential scanning calorimetry
MWNT	Multi-walled carbon nanotube
NEMS	Nanoelectro-mechanical system
NTC	Negative temperature coefficient
PE	Polyethylene
PET	Polyethylene terephthalate
PP	Polypropylene
PVOH	Polyvinyl alcohol
SEM	Scanning electron microscope

---

---

SiO <sub>2</sub>	Silicon dioxide
SSA	Specific surface areas
SWNT	Single-walled carbon nanotube
TEM	Transmission electron microscopy
TGA	Thermogravimetric analysis
UV	Ultraviolet
γ-APS	γ-Aminopropyltriethoxysilan

---

## Symbole

---

$\vec{a}$	Unit vectors of the hexagonal lattice
$\vec{C}_h$	Chiral vector
$j$	Non-zero integer
$V_f$	Fibre volume fraction (%)
$\theta$	Chiral angle
$d$	Fibre diameter
$\sigma_t$	The fibre tensile stress at gauge length
$\sigma_c$	The fibre fracture stress at critical fragment length
$l_a$	The average fragment length of fibre
$l_c$	The critical fragment length of fibre
$\tau$	The interfacial shear strength
$H_U$	The total heat generated in the dynamic scanning of DSC
$H_T$	The total heat generated in the isothermal scanning of DSC
$\alpha$	The degree of conversion during dynamic cure
$\beta$	The degree of conversion during isothermal cure
$E_{CNT}$	The elastic modulus of carbon nanotube
$E_{epoxy}$	The elastic modulus of epoxy
$E_{interphase}$	The interphase modulus
$E_m$	The mean modulus of matrix around fibre
$\nu_m$	The Poisson ratio of matrix
$m$	The Weibull shape parameter
$l_0$	The Weibull scale parameter
$R_0$	The initial resistance of the specimen
$\epsilon$	The tensile strain
$\delta$	The width of microcrack
$G_m$	The shear modulus of matrix
$T$	Absolute temperature
$E_c$	The the activation energy for the conduction process
$T_c$	The temperature of cure
$T_g$	Glass transition temperature
$T_{g\infty}$	The glass transition temperature of the fully cured resin
$\mu$	The mobility of charge carriers in insulative polymer

---

---

$W$	The potential energy barrier
$k$	Boltzmann constant
$e$	Electronic charge
$\rho_{glass}$	Specific volume electrical resistivity of glass fibre
$L_0$	The gauge length in tensile test of single glass fibre
$l_{CNT}$	Average length of CNT
$d_{CNT}$	Average diameter of CNT
$V_{CNT}$	The volume fraction of MWNTs in interphase region
$V_{interphase}$	The volume fraction of interphase in matrix
$E_f$	The fibre tensile modulus
$R_N$	The normalized resistance
$\delta_e$	The displacements of effective regions of fractured fibre in matrix
$\delta_i$	The displacements of ineffective regions of fractured fibre in matrix
$L_i$	The length of ineffective regions of fractured fibre in matrix
$\alpha_T$	The coefficient of thermal expansion in interphase region
$R$	The molar gas constant
$A$	Absorbance of a given functional group
$A_{2962}$	Absorbance of the methyl group
$p$	The nomalized relative intensity of a given functional group
$\Psi$	The heating rate
$E_a$	The activation energy of the cure reaction

---



# Contents

<b>1</b>	<b>Motivation and Approach</b>	<b>1</b>
<b>2</b>	<b>Introduction</b>	<b>4</b>
2.1	Fibre reinforced polymer composites . . . . .	4
2.1.1	Glass fibre . . . . .	5
2.1.2	Polymer matrices . . . . .	8
2.1.3	Interphase between glass fibre and matrix . . . . .	11
2.2	Carbon nanotube modifying composites . . . . .	13
2.2.1	Properties of carbon nanotubes . . . . .	15
2.2.2	CNTs modifying polymer composites . . . . .	22
<b>3</b>	<b>Materials and Methods</b>	<b>24</b>
3.1	Raw materials . . . . .	24
3.2	Depositing MWNTs onto glass fibre . . . . .	25
3.2.1	Electrophoretic deposition . . . . .	25
3.2.2	Dip coating method . . . . .	27
3.3	Single fibre model composites . . . . .	29
3.4	Characterizations . . . . .	29
3.4.1	Topographic morphology . . . . .	29
3.4.2	Single fibre tensile test . . . . .	29
3.4.3	Single fibre electrical resistance measurement . . . . .	30
3.4.4	Interfacial adhesion strength test . . . . .	32
3.4.5	Piezoresistivity of single fibre and single fibre composite . .	34
3.4.6	Thermal analysis . . . . .	37
3.4.7	Infrared analysis . . . . .	37
<b>4</b>	<b>Results and Discussions</b>	<b>39</b>
4.1	MWNTs coating on the glass fibre . . . . .	39
4.2	Interfacial adhesion strength of composites . . . . .	43
4.3	<i>In-situ</i> strain sensor . . . . .	53
4.3.1	Piezoresistivity of single MWNTs-glass fibre . . . . .	54
4.3.2	Single MWNTs-glass fibre as strain sensor in composites .	55

4.4	Electromechanical switch . . . . .	61
4.4.1	Switch actuated by strain . . . . .	61
4.4.2	Switch actuated by thermal source . . . . .	66
4.5	Single MWNTs-glass fibre in polymer as chemical and physical sensor	71
4.5.1	Monitoring the polymerization of thermoset polymer . . .	73
4.5.2	Monitoring the crystallization of thermoplastic polymer . .	83
<b>5</b>	<b>Summary and Outlook</b>	<b>88</b>
5.1	Summary . . . . .	88
5.2	Outlook . . . . .	91
	<b>Appendix</b>	<b>93</b>
	List of Figures . . . . .	93
	List of Tables . . . . .	95
	References . . . . .	96
	<b>List of Publication</b>	<b>110</b>

# 1 Motivation and Approach

Fibre reinforced plastics (FRP), such as glass, notably aramid and carbon fibre reinforced plastics, have a rapid rise in use in the past 30 years due to their high strength; stiffness and light weight compared with more traditional structural materials such as steel and aluminium [1]. These composites now dominate the aerospace, leisure, automotive, construction and sporting industries. Among them, glass fibres are the most widely used fibres to reinforce plastics because of their low cost (compared to aramid and carbon) and fairly good mechanical properties [2]. The reason for the composite's superior performance is the synergistic combination of the two, or more, constituent phases.

It is well known that the interphase between reinforcements and matrix is a controlling element in performance of both bio-composites and man-made composites. As a long-standing problem in fibre-reinforced polymer composites, internal micro-cracks normally occur around the fibre/matrix interphase region that strongly affect fatigue life and damage tolerance of the materials. Consequently, the tailoring of well adhesion, durable interphases between the matrix and reinforcement have become a critical concern with the raised requirement for structural strength of materials. There have been many methods to modify the interphase region, for example, deposition of coupling agent and film former onto the surface of fibre [1, 3]. Recently, various nanoscale materials have been used for enhancing the interfacial strength of composites [4, 5]. On the other hand, the early detection of the microcracks also has been one of the most challenging tasks in materials science. In order to early monitor internal microcracks of a material, immense efforts have been made over the last decades. However,

an embedded sensor usually brings some structural defects into material and the implementation of complex equipment remains a technical challenge for field application [6].

Multifunctional materials offer a promising and simple solution to above problems. Besides the improvement in mechanical properties, some new functions are desired to be integrated into the traditional composites, for instance, *in-situ* sensor. Carbon nanotubes (CNTs) are ideal candidates for introducing new multifunctions into the traditional composites, because of their nanoscale diameter and exceptionally electrical conductivity and high mechanical properties with tensile strength (200 GPa), elastic modulus (200-5000 GPa) and fracture strain (10-30 %) [7–9]. Direct dispersing CNTs into the matrices is a widely used method, which can improve the mechanical properties, electrical or thermal conductivities of composites [10, 11], however, it also sacrifices some unique original characteristics of composite, such as the insulative performance of polymer materials.

Inspired by “optimum” nature biomaterial, such as bone, it is a better path to obtain multifunctional composites that functionalizing the interphase between fibre and polymer matrix utilizing CNTs.

Thus, the experimental routes to fulfil the objectives of this work are listed in the following:

- Depositing multi-walled carbon nanotubes (MWNTs) onto insulative glass fibre surface through dip coating and electrophoretic deposition (EPD) methods, respectively.
- Observing the morphology of the CNTs coating on glass fibre and testing the tensile strength of single MWNTs-glass fibre treated by different conditions.
- Evaluating the interfacial shear strength of composites and the qualities of various interphases.
- Realizing the multifunctional interphase of MWNTs-glass fibre reinforced plastics (GFRP) and developing the new functions in traditional composites.

Figure 1.1 show the overview of the work program in this research, besides improving the interfacial strength, the multifunctional interphase and the new concept miniaturizing devices utilizing excellent comprehensive performance of MWNTs will be developed.

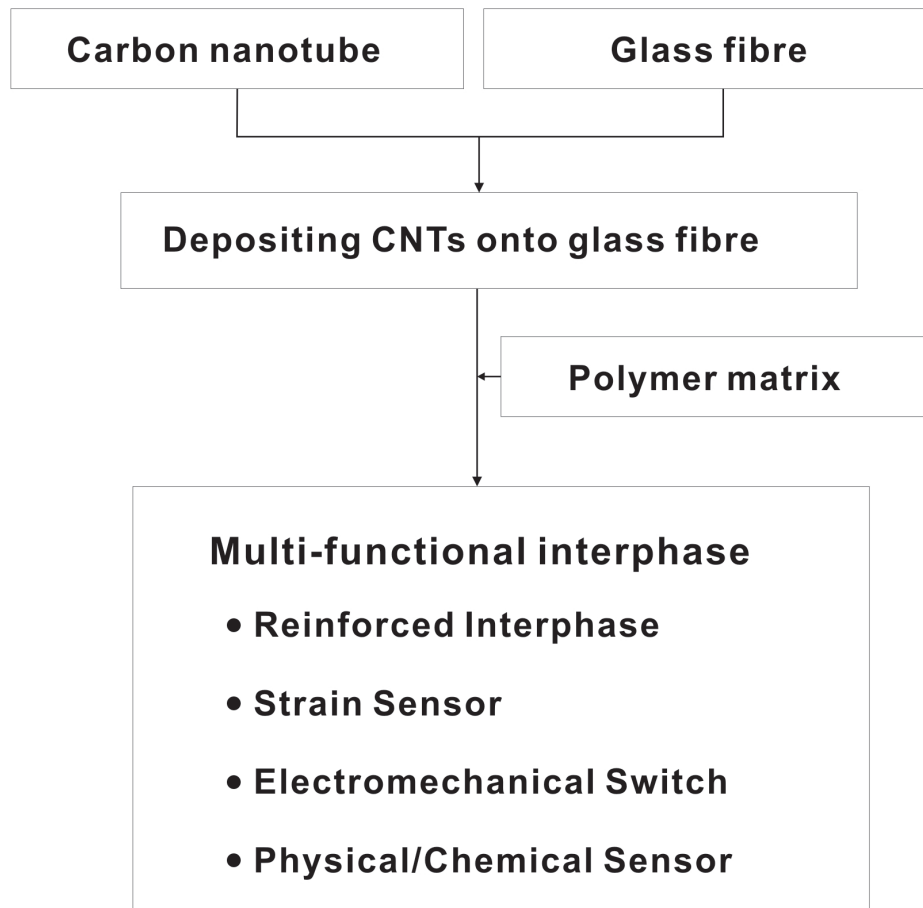


Figure 1.1: Overview of the work plan in this research

## 2 Introduction

### 2.1 Fibre reinforced polymer composites

Until 1940s, the growth of structural composite industry really began and “Synthetic Composite Material Age” came toward us. Up to this time, the main commercial use of fibre reinforced plastics (FRP) was for the construction of aircraft radoms in USA, which was a response to a general call from the using communities for light weight, high strength structural materials. Subsequently, the application of FRP was expanded to the boat hulls, car bodies and lorry cabs. As the development of resin matrix, the production of fibres has been accelerated since the 1950s with the introduction of electrical grade glass ( $E_{glass}$ ), high dielectric glass ( $R_{glass}$ ), magnesia-alumina-silicate glass ( $S_{glass}$ ), special acid- and alkali-resistant glass ( $AR_{glass}$ ) [12, 13]. Glass fibre has been the major reinforcement for FRP industry, combined with polymer matrix system, which currently provides glass fibre reinforced plastics (GFRP) products in a diversity of market areas such as transportation, construction, marine, electric and consumer products, Figure 2.1 shows some examples of GFRP application. Many of these industrial composites are cost competitive with metals, and in many instances GFRPs are able to displace metals due to improved properties (low corrosion and better fatigue resistance), lower tooling costs and ease of fabrication [14].

By definition, composites are the materials composed of a mixture of two or more phases, and their overall behaviour is dependent on the properties and the interaction of the constituent phases. Glass fibre reinforced polymer is one typical composites, of which property is dependent on three elements: i) glass fibre; ii) resin matrix; iii) the



Figure 2.1: Applications of glass fibre reinforced plastics

interphase between fibre and matrix. Since high tensile modulus and strength, the fibres carry the most of the load in composite. The fibres also toughen the brittle matrix by blocking or deflecting any cracks that may propagate through the polymer. In addition, the fibres can be selectively arranged to lie in specific directions and locations where the maximum stresses are likely to occur. The role of the matrix resin is to determine and maintain the shape of the composite, to keep the fibres in position, to prevent the fibres from buckling, and to protect the fibre surfaces from chemical and mechanical damage. The interphase is crucial in controlling composite properties because load is transferred from the matrix to the fibre through the interphase and deformation of the interphase region is critical in absorbing energy during failure [15, 16]. These three components are particularly described in following sections.

### 2.1.1 Glass fibre

Glass fibre is the original fibre reinforcement of modern composites. Though the ancient Phoenicians, Egyptians and Greeks knew how to melt glass and stretch it into thin fibres, it was not until 1930s that the process evolved into the commercial-scale manu-

facturing of continuous fibres, which would later be used as structural reinforcements. [17] The manufacturing processes of continuous glass fibre can be broken down into five basic steps: batching, melting, forming fibre, coating and drying/packageing, Figure 2.2 shows the alkali-resistant glass (AR-glass) fibre spinning device in the institute of Polymer Research Dresden.

The main chemical component of glass fibre is silica,  $\text{SiO}_2$ . Pure silica is a perfectly viable glass and glass fibre, but, it must be worked with at very high temperatures, which is a drawback unless its specific chemical properties are needed. It is usual to introduce impurities into the glass in the form of other materials to lower its working temperature. These materials also impart various other properties to the glass that may be beneficial in different applications, for example alkali-resistant fibre [18–20]. Table 2.1 provides the chemical components and their weight ranges for different types of commercial glass fibres.

Table 2.1: Weight percentage of components in different types of glass fibre [21]

	A Glass	C Glass	D Glass	E Glass	AR Glass	R Glass
	High alkali	Chemical resistance	Hi-dielectric	“Electric” glass	Alkali-resistance	High dielectric
$\text{SiO}_2$	63-72	64-68	72-75	52-56	55-75	55-60
$\text{Al}_2\text{O}_3$	0-6	3-5	0-1	12-16	0-5	23-28
$\text{B}_2\text{O}_3$	0-6	4-6	21-24	5-10	0-8	0-0.35
$\text{CaO}$	6-10	11-15	0-1	16-25	1-10	8-15
$\text{MgO}$	0-4	2-4		0-5		4-7
$\text{ZnO}$						
$\text{BaO}$		0-1				
$\text{Li}_2\text{O}$					0-1.5	
$\text{Na}_2\text{O}+\text{K}_2\text{O}$	14-16	7-10	0-4	0-2	11-21	0-1
$\text{TiO}_2$	0-0.6			0-1.5	0-12	
$\text{ZrO}_2$					1-18	
$\text{Fe}_2\text{O}_3$	0-0.5	0-0.8	0-0.3	0-0.8	0-5	0-0.5
$\text{F}_2$	0-0.4			0-1	0-5	0-0.3

Owing to the high strength-to-weight ratio, glass fibres have been superior reinforcement in applications where high strength and minimum weight are required. In textile form, this strength can be unidirectional or bidirectional, allowing flexibility in design



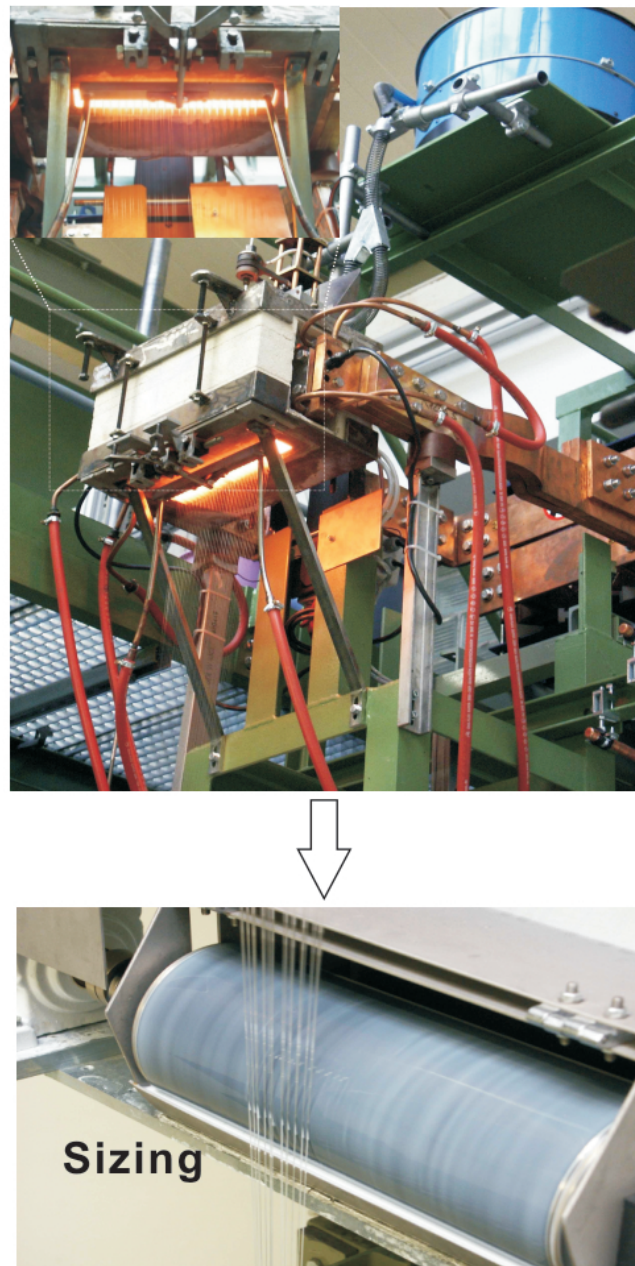


Figure 2.2: Pictures of glass fibre spinning and sizing devices in Leibniz Institute of Polymer Research

and cost. Glass fibre is a dimensionally stable engineering material, which does not stretch or shrink after exposure to extremely high or low temperatures. Glass fibres are also useful thermal insulators because of their high ratio of surface area to weight. Additionally, glass fibre is an excellent electrical insulative material. The combination

of properties such as low moisture absorption, high strength, heat resistance and low dielectric constant makes glass fibre ideal as a reinforcement for printed circuit boards and insulating varnishes [22]. Table 2.2 displays some properties for various types of glass fibre.

Table 2.2: Properties for different types of glass fibre [21]

	A Glass	C Glass	E Glass	AR Glass	R Glass
Density(g/cm <sup>3</sup> )	2.44	2.52	2.58	2.70	2.54
Tensile strength(MPa)	3310	3310	3445	3241	4135
Young's modulus(GPa)	68.9	68.9	72.3	73.1	85.5
Elongation %	4.8	4.8	4.8	4.4	4.8
Durability (%weight loss)					
H <sub>2</sub> O: 24hr	0-6	3-5	12-16	0-5	23-28
10%HCl: 24hr	0-6	3-5	12-16	0-5	23-28
Volume resistivity (ohm·cm)	1.0E+10		4.02E+14		2.03E+14
Surface resistivity(ohms)			4.20E+15		6.74E+13

### 2.1.2 Polymer matrices

Polymeric materials with a range of excellent mechanical properties, low density, durability, and low cost, are widely used in the daily needs, range from simple packaging to heavy construction, and play an important role in the improvement and quality of life. Based on the chain structure, polymer could be classified as linear, branched or cross-linked. In linear polymers, the mer units are from single continuous chain and the mer units in the chain are bonded together by weak van der Waals forces. In the case of branched polymers, additional side branches result from further reaction that occur during synthesis. A consequence of the existence of the side branches is that the packing efficiency of the polymers is reduced, resulting in a lower density. In cross-linked polymers, the side branches join up with adjacent branches chains. These bonds are essentially covalent bonds formed during the synthesis of the polymer or at elevated temperature, and the net result is a cross-linked chain polymer [23].

Polymers can also be classified as either thermosets or thermoplastics. Thermoplas-

tic materials melt upon heating and return their original chemical state upon cooling. Thermoset materials become infusible and insoluble upon heating and, after heating, do not return to their original chemical state upon cooling. Thermoplastics can be further classified as amorphous or semi-crystalline. Amorphous thermoplastics have no long range order on supermolecular level. Semi-crystalline thermoplastics have at least some portion of their bulk (and surface) in a state exhibiting long range order. Thermoset material can be amorphous or semicrystalline [24].

### Epoxy resin

Epoxy resin, containing more than one ethoxyline group, is one of the widest applied thermosetting polymers. Because the epoxy groups are the monomers, the epoxy can be polymerized through reacting with “hardener”. The process of polymerization is called curing, which can be controlled through temperature, choice of resin and hardener compounds, and the ratio of said compounds. There are two main categories of epoxy resins, namely the glycidyl epoxy, and non-glycidyl epoxy resins. Diglycidyl ether of bisphenol-A (DGEBA) is a typical commercial epoxy resin and is synthesised by reacting bisphenol-A with epichlorohydrin in presence of a basic catalyst [25–27]. Figure 2.3 shows the structure of DGEBA, the properties of the resins depend on the value of  $n$ , which is the number of repeating units commonly known as degree of polymerization. Typically,  $n$  ranges from 0 to 25 in many commercial products.

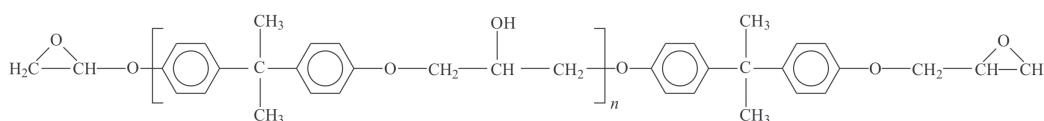


Figure 2.3: The Structure of basic unit of DGEBA

The curing agents for epoxies usually include amines, polyamides, phenolic resins, anhydrides, isocyanates and polymercaptans. The choice of resins and hardeners is available depending on the process and properties required. The stoichiometry of the epoxy-hardener system also affects the properties of the cured material. Employing dif-

ferent types and amounts of hardener which tend to control cross-link density vary the structure. Amines and amine-functional amides are the most commonly used hardeners for high-performance, ambient-cured industrial maintenance epoxy polymers. The typical reactions between epoxy and amine hardener are shown in Figure 2.4. Primary and secondary amines are highly reactive with epoxy. When there is an excess of epoxy groups or when the secondary amines have a low reactivity, a third reaction can compete with the two previous ones [28]. These epoxy polymers are commonly

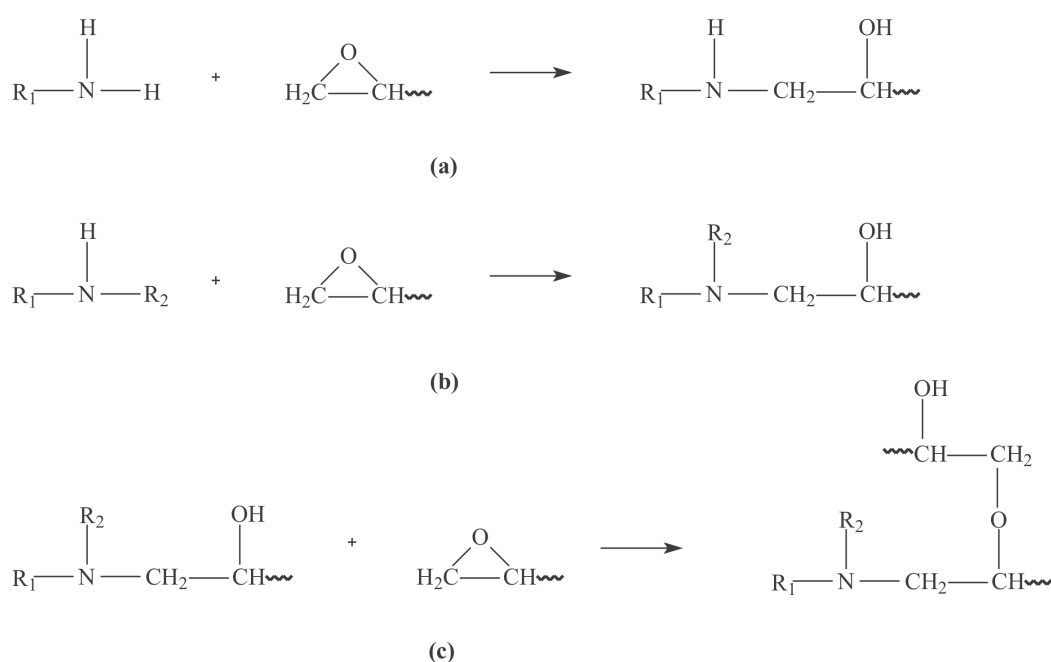


Figure 2.4: Chemical reactions for a epoxy-amine system: (a) epoxide ring-opening reaction with primary amine (b) epoxide ring-opening reaction with secondary amine and (c) etherification reaction between reacted and unreacted epoxy groups

used as adhesives, high performance coatings and potting and encapsulating materials, owing to their excellent electrical insulative properties, low shrinkage, good adhesion to many metals and resistance to moisture, thermal and mechanical shock.

### Poly(ethylene terephthalate)

Poly(ethylene terephthalate), PET, is a slow crystallizing polymer, which besides its wide industrial success has also become a subject of many research activities. The rea-

son of that is its high melting point and good thermal resistance as well as its good electrical and excellent mechanical properties. It can crystallize from the melt over a wide range of supercooling conditions or it may be quenched to the “amorphous” phase and crystallize by simple heating or drawing thus giving a relatively higher possibility of controlling product final structure by acting on processing conditions. The slow crystallization behaviour of PET, on the other hand, offers a broader experimental access to the study of its crystallization kinetics [29]. In this research, the simultaneous direct current (DC) resistance measurement of interphase between fibre and matrix was exploited to monitor the crystallization procedure of PET.

### 2.1.3 Interphase between glass fibre and matrix

The “interphase” is a region where the fibre and matrix phases are chemically or mechanically combined. It is likely a diffusion zone, a chemical reaction zone or a nucleation zone, a thin layer of fibre sizing or coating, or any combination of the above. The formation of such an interphase around the fibre results from local changes of chemical or physical process imposed by fibre surface, namely cross-linking, immobilization, interdiffusion, crystallization. Therefore, the chemical, physical and mechanical properties of interphase region vary either continuously or in stepwise manner between those of the bulk fibre and matrix materials. Figure 2.5 displays the schematic diagram and AFM image of the interphase region in FRP [30, 31].

Understanding the stress transfer mechanism from matrix to fibre is vital to understand composite behaviour and performance. Therefore, the research of the micro-scale interphase phenomena between fibre and matrix has attracted considerable attention over 50 years [32, 33]. In brittle matrix composites, energy can be absorbed from the crack by four basic mechanisms: (1) deviation of the crack from the self-similar direction (which includes the crack following the fibre-matrix interphases), (2) strain reduction in the matrix material in front of the crack by the fibre reinforcement, (3) pullout and fracture of the fibres behind a growing crack, and (4) stretching of bridging fibres

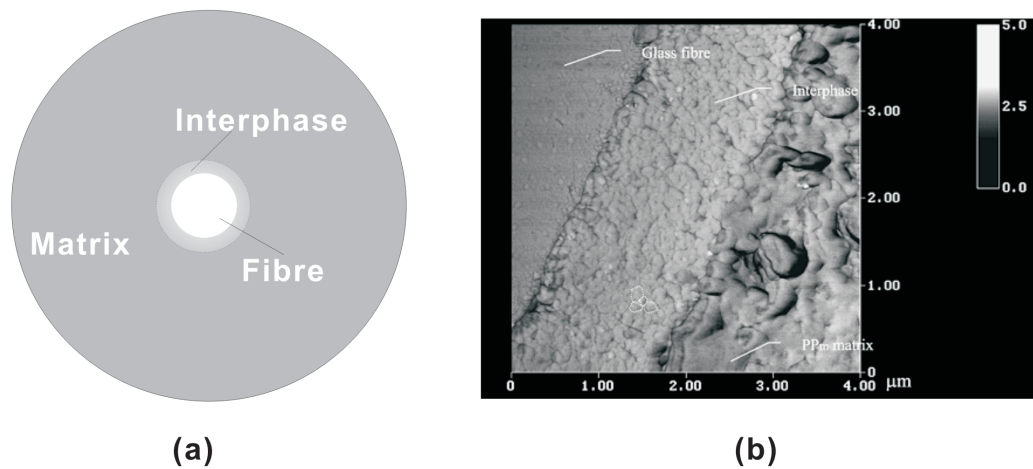


Figure 2.5: The interphase region in FRP: (a) schematic diagram of three elements in FRP (b) AFM phase image of interphase in  $\gamma$ -APS/PP-PPm composites [30]

behind a growing crack. In such a composite, if the fibres are strongly bonded to the matrix, a crack will propagate right through the fibres without deviation, see Figure 2.6a, the opening of large matrix cracks is resisted in part by bridging fibres. Such an arrangement might seem to be favorable, but in fact, the potential for energy absorption by deviation of the crack (Figure 2.6b) may be lost [34]. To summarize, the strength of the interphase is expected to play a dominant role in the off-axis and shear properties, with a higher bond strength giving higher composite strength up to some limit such as the local matrix strength. However, for glass and ceramic matrix composites the longitudinal behaviour may become weak and brittle if the bond strength is too high. The frictional sliding resistance of debonded fibres is of importance in determining the onset of significant matrix cracking in longitudinal tension for some brittle-matrix systems [35]. Therefore, the interphase should be modified based on particular functions, for example, a better interfacial adhesion will impart better properties of the composites, such as the interlaminar shear strength (ILSS), delamination resistance, and fatigue and corrosion resistance [36, 37].

The test of single fibre microcomposites is the widely used method to measure the interfacial strength, in which individual fibres are embedded in specially constructed matrix blocks of various shapes and sizes. Test methods using microcomposites in-

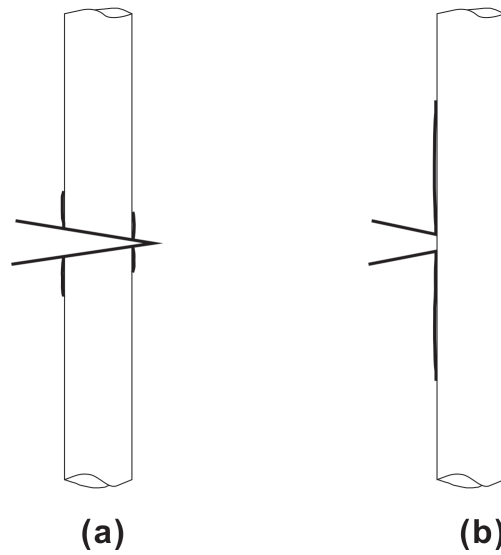


Figure 2.6: Propagations of cracks in composite with different interphase: (a) crack propagate through the interphase in stronger interphase region (b) crack lead to debonding failure between fibre and matrix

clude the single fibre compression test, the fibre fragmentation test, the fibre pull-out test, the fibre push-out (or indentation) test and the slice compression test. These tests have a variety of specimen geometries and scales involved, Figure 2.7 shows some examples of these test methods. In these tests, the bond quality at the fibre-matrix interphase is measured in terms of the interphase fracture toughness, or the interfacial shear strength (IFSS), and the interface frictional strength (IFS), which is a function of the coefficient of friction, and residual fibre clamping stress. These tests are considered to provide direct measurements of interphase properties relative to the test methods based on bulk composite specimens [37].

## 2.2 Carbon nanotube modifying composites

Nano-particles are presently considered to be high potential filler materials for the improvement of mechanical and physical properties of polymer composite. The nanometric size, leading to huge specific surface areas (SSA) of up to more than  $1000 \text{ m}^2/\text{g}$ , and their unique properties (of at least some of these nano-particles) have caused inten-

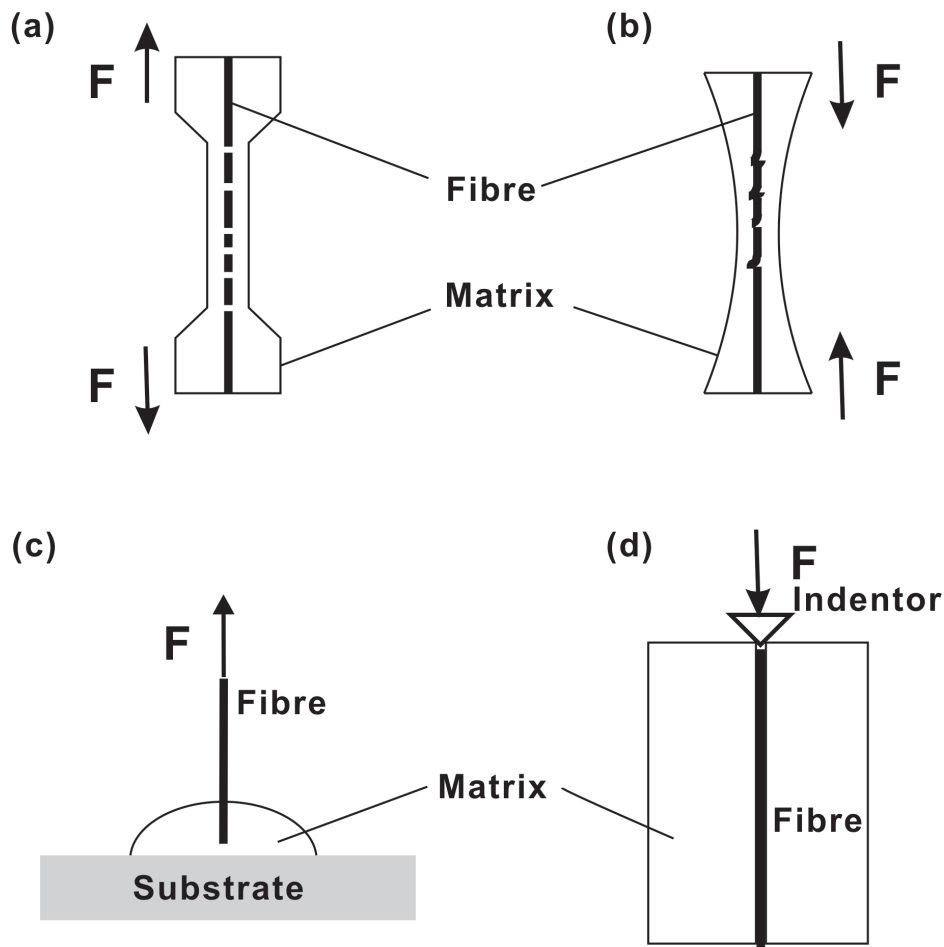


Figure 2.7: Different test methods of interfacial strength for single fibre model composite:  
 (a) Fragmentation test (b) Compression test (c) Pull-out test (d) Push-out test

sive research activities in the fields of natural and engineering sciences. Tsai and Wu [38] investigated the effect of nanoscale organoclay on tensile properties of glass fibre reinforced composites with particles loadings of 2.5-7.5 wt%. They reported 74 % and 67 % improvement in transverse tensile strength and modulus whereas the properties deteriorated in the longitudinal direction. Cho et al. [4] infused 3 wt% and 5 wt% disk-like graphite nanoparticles in epoxy via sonication and reported 10 % and 16 % gain in longitudinal compressive strength of carbon/epoxy composite, respectively with 55 % fibre volume fraction. Carbon nanotubes are the eye-catching candidates as reinforcement in composite due to the combination of excellent mechanical, thermal and electrical properties attributed them.



### 2.2.1 Properties of carbon nanotubes

Carbon nanotubes are hollow cylinders of graphite sheets. They can be considered as single molecules, regarding their small size, (nanoscale diameter and microscale length), or as quasi-one dimensional crystals with translational periodicity along the tube axis. There are two main types of nanotubes available today. Single walled nanotubes (SWNT) consist of a single sheet of graphene rolled seamlessly to form a cylinder with a diameter of an order of magnitude of 1 nm and length of up to centimetres. Multi-walled nanotubes (MWNT) consist of an array of such cylinders formed concentrically and separated by 0.35 nm, similar to the basal plane separation in graphite. MWNTs can have diameters from 2 to 100 nm and lengths of tens of microns [39]. CNTs are produced by three main techniques: electric arc discharge, laser ablation, and chemical vapour deposition (CVD) [40].

The arc discharge technique involves the generation of an electric arc between two graphite electrodes under external electrical field. The anode is usually filled with a catalyst metal powder, such as Fe, Ni, and Co. CNTs can be collected from the cathode. This method can easily produce straight and near-perfect MWNTs.

Laser ablation was first used for the synthesis of fullerene. Over the years, the technique has been improved to produce CNTs. In this technique, a pulsed laser is used to vaporize a composite consisting of graphite and a catalyst (typically Co/Ni alloy) held in a furnace at a temperature near 1200 °C. SWNTs with high purity can be obtained by employing this method. Compared with MWNTs prepared in an arc discharge chamber, the MWNTs grown in a laser-ablation process are relatively short.

CVD is a process in which gaseous molecules, called precursors, are transformed into solid materials on a substrate at a range of temperatures between 550 and 900 °C. In this process, the catalytic particles deposited on the substrate can decompose hydrocarbon gas to form carbon and hydrogen, whereas the carbon dissolves into particles and precipitates out from its circumference to form CNTs. The catalyst acts as a template on which CNTs can grow, and by controlling the catalyst size and the reac-

tion time, the diameter and length of CNTs can be controlled. The CVD-grown CNTs usually show poor crystallinity and a postsynthesis at a high temperature is often applied to improve the product quality. CVD is especially appealing in making electronic devices that require controlled growth of CNTs on prepatterned substrates.

### 2.2.1.1 Structure of CNTs

According to the rolling angle of the graphene sheet, CNTs have three chiralities: armchair, zig-zag, and chiral. The tube chirality is defined by the chiral vector  $\vec{C}_h$  and the chiral angle,  $\theta$  (Figure 2.8(a)). The chiral vector, often known as the roll-up vector, can be described by:

$$\vec{C}_h = n\vec{a}_1 + m\vec{a}_2 \quad (2.1)$$

where the integers  $(n, m)$  are the number of steps along the unit vectors  $a_1$  and  $a_2$  of the hexagonal lattice. The chiral angle determines the amount of twists in the tube. The two limiting cases exist where the chiral angle is at  $0^\circ$  and  $30^\circ$ , which are referred to as armchair and zig-zag, shown in Figure 2.8(b) and (c), respectively, based on the geometry of the carbon bonds around the circumference of the nanotube [41]. The chirality of the carbon nanotube has significant implications on the material properties. In particular, tube chirality is known to have a strong impact on the electronic properties of CNTs.

### 2.2.1.2 Mechanical properties of CNTs

The mechanical properties of CNTs are closely related to the nature of the chemical bonds between the carbon atoms. The bonding mechanism of CNTs is similar to that of graphite (or graphene for SWNTs). A carbon atom consists of six electrons outside the nucleus, and its electronic structure can be expressed as  $1s^2 2s^2 2p^2$ . When carbon atoms are combined to form graphite, one  $s$  orbital and two  $p$  orbitals are combined to form three hybrid  $sp^2$  orbitals at  $120^\circ$  to each other within a plane. The in-plane bond is known as a sigma bond ( $\sigma$  bond), a strong covalent bond with a bond energy

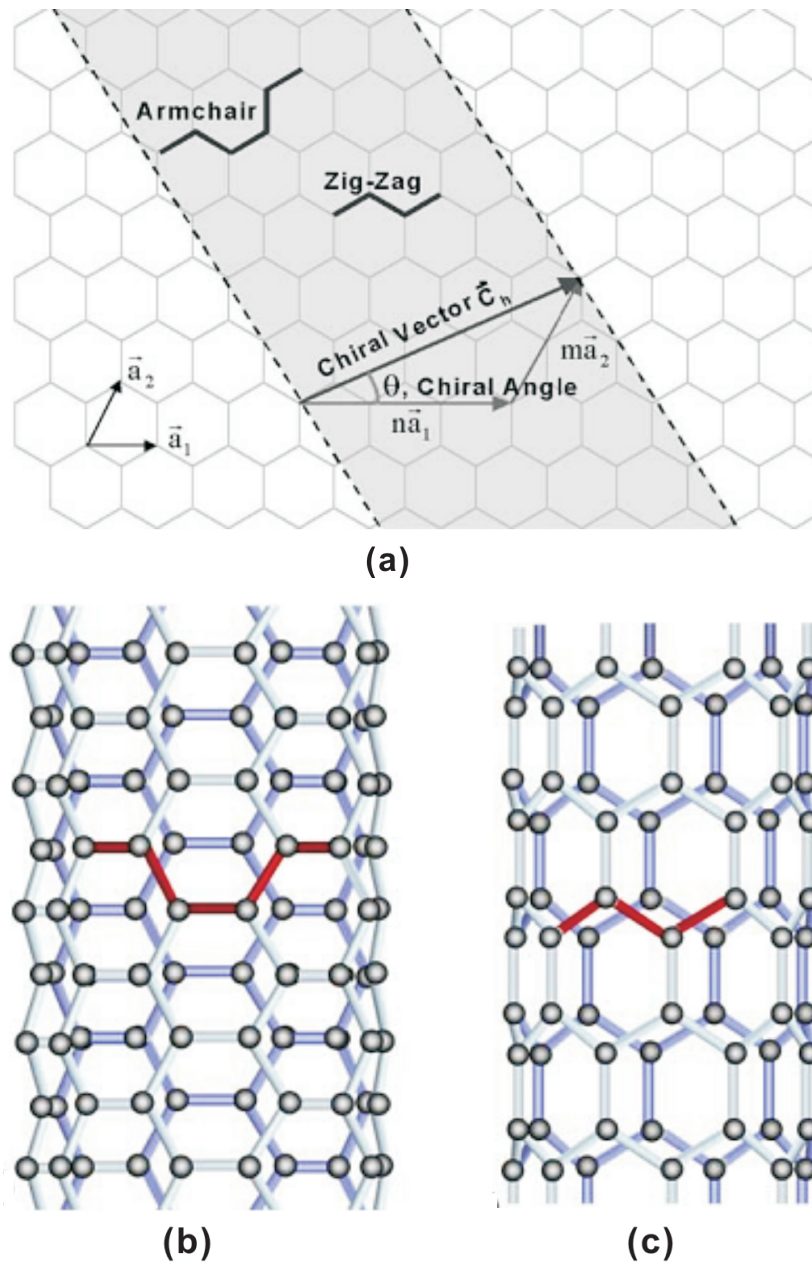


Figure 2.8: Structures of CNTs (a) Schematic diagram showing how a hexagonal sheet of graphite is 'rolled' to form a carbon nanotube. Illustrations of the atomic structure of (b) an armchair and (c) a zig-zag nanotube [41]

of 346 KJ/mol, which is responsible for the high stiffness and high strength of a CNT. The remaining  $p$  orbital is perpendicular to the plane of the  $s$  bond, contributing mainly to the interlayer interaction. It is called a  $\pi$  bond ( $\pi$  bond) and is much weaker than

the  $\sigma$  bond.

The tensile rupture of CNTs has been studied and the plastic deformation has been investigated theoretically by tight binding and ab initio molecular dynamic studies. M.B. Nardelli et al. demonstrate that a “transverse” tension applied perpendicularly to a C-C bond, as in tensile strain to an armchair tube, gives rise to a ductile deformation [42]. In contrast to that a “longitudinal” tension in parallel to the C-C bond as in tensile strain to a zig-zag tube leads to a brittle rupture. The transverse tension finds a natural release in the rotation of the C-C bond perpendicular to it, Stone-Wales transformation which produces two pentagons and two heptagons coupled in pairs (5-7-7-5), see Figure 2.9 [43]. The Stone-Wales transformation plays a key role in the nanotube plastic deformation under tension. The appearance of the (5-7-7-5) defect can be interpreted as nucleation of a dislocation loop in the planar hexagonal network of the graphene sheet. Tubes with  $n, m \leq 14$  are calculated to be completely ductile while larger tubes are moderately or completely brittle [44]. The first experimental measure-

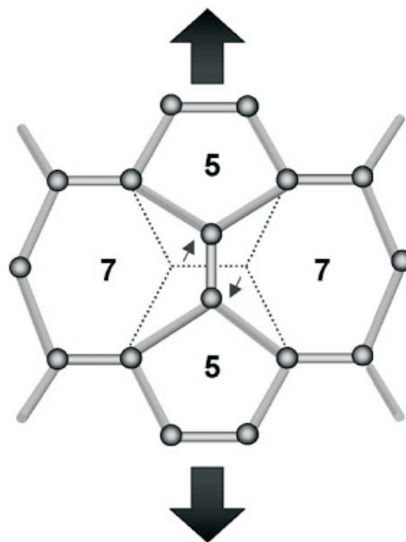


Figure 2.9: The Stone-Wales transformation occurring in an armchair nanotube under axial tension [41]

ment of the Young's modulus of MWNTs was conducted by Treacy and coworkers [8] through monitoring the amplitudes of thermal vibrations of an individual MWNT

inside a TEM chamber. From such measurements the Young's modulus could be inferred if the nanotubes were supposed to behave as hollow cylinders with a given wall thickness. Treacy et al. obtained an average value of 1.8 TPa out of a sample of 11 different nanotubes, for which individual values ranged from 0.4 to 4.15 TPa. For the first time, Wong et al. [9] directly measured the stiffness constant of arc-MWNTs by atomic force microscope (AFM). This gave an average value for Young's modulus of 1.28 TPa. More importantly they also managed to make the first measurement, obtaining an average bending strength of 14 GPa. Additionally, Salvétat et al. [45] used an AFM to bend an arc-MWNT that had been pinned at each end over a hole obtaining an average modulus value of 810 GPa.

Measurements on SWNT took longer due to the difficulties in handling them. The first measurements were carried out by Salvétat et al. [46] using their AFM method, reporting a tensile modulus of about 1.0 TPa for small-diameter SWNT bundles. The properties of large-diameter SWNT bundles were dominated by shear slippage of individual nanotubes within the bundle. Yu et al. [47] reported that Young's modulus and strength are in the range of 0.32-1.47 TPa and 13-52 GPa, respectively, through the same method. Failure occurred at a maximum strain of 5.3 % giving a toughness of approximately 770 J/g. In addition they observed that failure occurred for the nanotubes on the perimeter of the bundle only with the rest of the tubes slipping apart. Intertube slippage within bundles presents a serious limitation to their mechanical properties. The low shear modulus means that effective moduli and strengths for bundles are far below those expected for individual SWNT.

### 2.2.1.3 Electrical properties of CNTs

The electrical properties of CNTs are affected by their chirality and diameter as referred to in Sect. 2.2.1.1. The reason is that the electrons of carbon atoms are confined in the singular plane of the graphene sheet in the radial direction. The conduction occurs in the armchair tubes through gapless modes because the valence and conduction bands

always cross each other at the Fermi energy, showing a metallic behaviour of CNTs. However, for the helical tubes with different chiralities, there are a large number of atoms in their unit cell, and the one-dimensional band structure shows an opening of the gap at the Fermi energy, thus leading to semiconducting properties [48]. The general rules for carbon nanotubes are as follows:  $(n, n)$  tubes are metal;  $(n, m)$  tubes with  $n - m = 3j$ , where  $j$  is a non-zero integer, are very tiny-gap semiconductors. All others are large-gap semiconductors [12, 48].

Tans and coworkers [49] made the first measurement of the transport properties of individual SWNTs using the two-probe method. They found that SWNTs indeed acted as genuine quantum wires, in which electrical conduction occurred via well-separated, discrete electron states that were quantum-mechanically coherent over long distances. Dai and coworkers reported that the lowest single-tube resistance measured with individual metallic SWNT is about 12 k $\Omega$  [50]. For individual semiconducting SWNTs grown on surfaces, relatively low resistance devices on the order of hundreds of kilo-ohms can be made by their approach, and the resistance increases with the diameter of SWNT decreasing [51].

Compared with SWNTs, the electrical properties of MWNTs are quite complex, as each MWNT contains a multilayer of graphene, and each layer can have different chiralities. Furthermore, the interactions between the graphene layers within a MWNT were found to disturb the current along the tube axis. In the first electrical resistance measurements of an individual MWNT down to  $T = 20$  mK by Langer et al. [52], in zero magnetic field a logarithmic decrease of the conductance with decreasing temperature and saturation below  $T \approx 0.3$  K were observed. In the presence of a magnetic field, perpendicular to the tube axis, a pronounced and positive magnetoresistance was measured. The results of de Heer and coworkers [53] suggested that the current mainly flows through the outermost shell. These results characterize that both the geometric variations of CNTs (e.g., defects, chirality, number of graphene layers, and tube diameter) and the degree of crystallinity (i.e., hexagonal lattice perfection) played a key

role in determining the electrical response of CNTs [40].

#### 2.2.1.4 Thermal properties of CNTs

It is well known that the graphite (in-plane direction) is a highly thermal conductive material, thus the longitudinal thermal conductivity of CNTs is expected to behave in the similar way. However, since the tube diameter is orders of magnitude lesser than that of a unit crystal of graphite, the thermal behaviour of CNTs is much different. Besides, other elements also affect the thermal behaviour of CNTs, for example, the increased stress induced in the CNT walls from the increased curvature of the tube [54]. Berber et al. [55] simulated the thermal conductivity of carbon nanotubes using equilibrium and non-equilibrium molecular dynamics. The results suggest an unusual high value of  $\approx 6600$  W/mK for an isolated (10, 10) nanotube at room temperature, comparable to the thermal conductivity of graphite. Kim et al. [56] showed that the thermal conductivity of a single MWNT with a diameter of 14 nm was about 3000 W/mK using a microfabricated suspended test device. This value is much higher than that of graphite at room temperature, and two orders of magnitude higher than those obtained for MWNT mats. Pop et al. [57] investigated the thermal properties of a single metallic SWNT by extracting its high-bias (I-V) electrical characteristics at 300 - 800 K. The thermal conductivity was reported as a remarkable 3500 W/mK at room temperature for a SWNT with a length of 2.6  $\mu\text{m}$  and a diameter of 1.7 nm. In fact, those reported results are drastically different, it is necessary to clarify which is reliable and what are the conditions for obtaining such values, and the theoretical research for the transportation of thermal phonons needs to be promoted either [58].

Besides the excellent thermal conductivities, CNTs also exhibit remarkable thermal stability. Pang et al. [59] studied the oxidation of carbon nanotubes and nanoparticles by thermogravimetric analysis (TGA) in air. The result showed that the nanotubes and nanoparticles are more resistant to oxidation than other forms of carbon (diamond, soot, graphite, and  $\text{C}_{60}$  studied previously under identical conditions. The TGA of

the nanotubes/nanoparticles in argon showed no weight change or detectable thermal transformation up to 1000 °C.

### 2.2.2 CNTs modifying polymer composites

The excellent comprehensive properties of CNTs have attracted considerable attention to a wide range of application. Following the first report on the preparation of CNT/polymer nanocomposites in 1994 [60, 61], a number of research papers have appeared in open media to study their interesting properties, including the structure-property relationship and potential applications in many different fields [61]. In particular, CNTs are considered to be the promising candidates to develop the new multifunctional composite. The first study using nanotubes for reinforcement of solution based composites was made by Shaffer and Windle in 1999 [62]. They carried out DMTA measurements on CVD-MWNT-PVOH films with nanotube weight fractions of up to 60 %. The storage modulus increasing from approximately 6 GPa for the polymer to 12 GPa for the 60 wt% composite film. While better results were observed above the polymer glass transition temperature, this is a reflection of the fact that it is easier to reinforce softer matrices. Schadler et al. [10] made the first true mechanical study for a MWNT-epoxy composite. In tension, the modulus increased from 3.1 GPa to 3.71 GPa on addition of 5 wt% nanotubes. However, the better results were seen in compression with an increase in modulus from 3.63 to 4.5 GPa. Ruan et al. [11] reported that a loading of 1 wt% MWNTs, randomly distributed in an ultra-high molecular weight polyethylene film, was reported to increase the strain energy density by 150 % and increase the ductility by 140 %. Secondary crystallites, which nucleated from the MWNTs, were attributed to the large ductility increase in PE. Grimmer and Dharan [63] have shown that the addition of 1 wt% of CNTs to the polymer matrix can improve the fatigue life of woven glass fibre/epoxy composites by 60 %, from 1450 cycles to 2300 cycles.

Since their small diameters, CNTs could act as metals or semiconductors, which are



gradually opening the door to future low-power fabrication of microdevices. Baughman et al. [64] first reported electromechanical actuators based on sheets of single-walled carbon nanotubes, which were shown to generate higher stresses than natural muscles and higher strains than high-modulus ferroelectrics. Cha et al. [65] fabricated a nanoelectromechanical switch/transistor consisting of suspended CNTs and self-aligned electrodes. That nanoscale switching device was operated by changing electrostatic forces between a suspended CNT and self-aligned electrodes and the possibilities for real applications using nanoelectro-mechanical system (NEMS) has been confirmed. The development of novel multifunctional polymer composites incorporated with CNTs has become a popular theme for recent years. Through embedding CNTs in a sizing or polymer matrix to form conductive pathways, the achieved non-uniformly and uniformly dispersed CNTs in composites have successfully been used as health sensors to monitor damage. Gao et al. [66] then studied the damage mechanism under cyclic loading in cross-ply laminates through the carbon nanotube network. Recently, a CNT yarn strain sensor with excellent repeatability and stability was developed by directly embedding the yarn in an epoxy resin [67].

As a new approach, here, it is attempted to introduce MWNTs into interphase between glass fibre and polymer matrix in order to form a multifunctional interphase. Utilizing the nano structured interphase, some new applications could be explored and achieved in conventional glass fibre composites.

## 3 Materials and Methods

### 3.1 Raw materials

The alkali-resistant glass (ARG) fibres with an average diameter of 12  $\mu\text{m}$  utilized in this work as control fibre were manufactured by a continuous spinning process without sizing at the Leibnitz Institute of Polymer Research. Commercially available carboxy-functionalized MWNTs (NC3101, Nanocyl S.A., Belgium) with an average diameter of 9.5 nm and an average length of 1.5  $\mu\text{m}$  were used rather than SWNTs, not only because of the relatively low cost but also because of their comparatively easier dispersion and the enhanced interfacial adhesion in composites is achieved with modifying the outer wall [68–70]. Nonionic surfactant Igepal CO 970 was used to disperse CNTs. Silane coupling agent 3-glycidyloxypropyltrimethoxysilane (Dynasylan<sup>®</sup> Glymo, Evonik Degussa Corporation, Germany) was added into CNT dispersion to introduce functional groups onto fibre surface and to improve the interfacial shear strength. Commercial DGEBA-based epoxy resin (resin EPR L20 and hardener EPH 960 in a weight ratio of 100:34, manufactured by Hexion Specialty Chemicals Stuttgart GmbH) was used as polymer matrix in the present study.

Polyethylene terephthalate (PET) multi-filament yarns (Wilhelm Walker GmbH, Illertissen, Germany) with a fineness of 50 dtex were used to analyse of the crystallization, which were in a state after removing the spin-finish by washing in hot water. To easier measurement, the PET yarns were prepared into film through hot pressing.

## 3.2 Depositing MWNTs onto glass fibre

### 3.2.1 Electrophoretic deposition

Preparation of a stable dispersion of MWNTs in a suitable solvent is a prerequisite for successful electrophoretic deposition. Firstly, 150 mg Igepal CO 970 was dissolved in 100 ml deionized water. Then, 100 mg MWNTs were added to the solution and dispersed employing a tip sonicator (Hielscher UP200S) at constant output power of 180 W equipped with a cylindrical sonotrode (3 mm) for 180 min. Figure 3.1(a) shows schematically Igepal CO 970 dispersed MWNTs in a stable dispersion (pH 6-7) [71]. Besides, we also mixed the dispersion of MWNTs with Glymo hydrolyzate for 1 h, which was stored overnight. Finally, the concentration of MWNTs was 0.05 wt.%, the Glymo concentration was 0.5 wt.%.

One very promising technique being developed for possibly manipulating CNTs on a variety of substrates is electrophoretic deposition, in which charged particles dispersed in a stable suspension are driven by a DC electric field to move towards an oppositely charged electrode. The electrophoretically deposited materials exhibit high packing density with homogeneous microstructure. The interest in the EPD technique is driven by its simplicity, cost-efficiency and its applicability to a great variety of materials such as porous substrates, fibrous bodies and textile structures [72–75]. It is being increasingly considered for the production of nanostructured coatings and layers on a variety of substrates, i.e. coatings for wear and oxidation resistance, bioactive coatings for biomedical implants, and functional coatings for photocatalytic, electronic, magnetic and related applications [76, 77]. The basic phenomena involved in EPD on a conductive substrate are well known and most conventional EPD processes are carried out on electrically conductive metallic or carbon/graphite substrates. However, the specific EPD mechanisms of the non-conducting substrates are yet less documented [77]. Recently, there are some interesting reports in the literature on the use of EPD technique for coating carbon nanotube-containing oxide films on non-conducting porous

tubular alumina substrates where the substrate was polished and covered with a thin film of silver by sputtering [78, 79]. To the best of our knowledge, exploiting EPD for coating CNTs onto insulative glass fibre surface has been rarely reported in the literature. Thus, the development of novel EPD process on glass fibre surface will stimulate and realize a broad range of surface modification applications for non-conducting fibres.

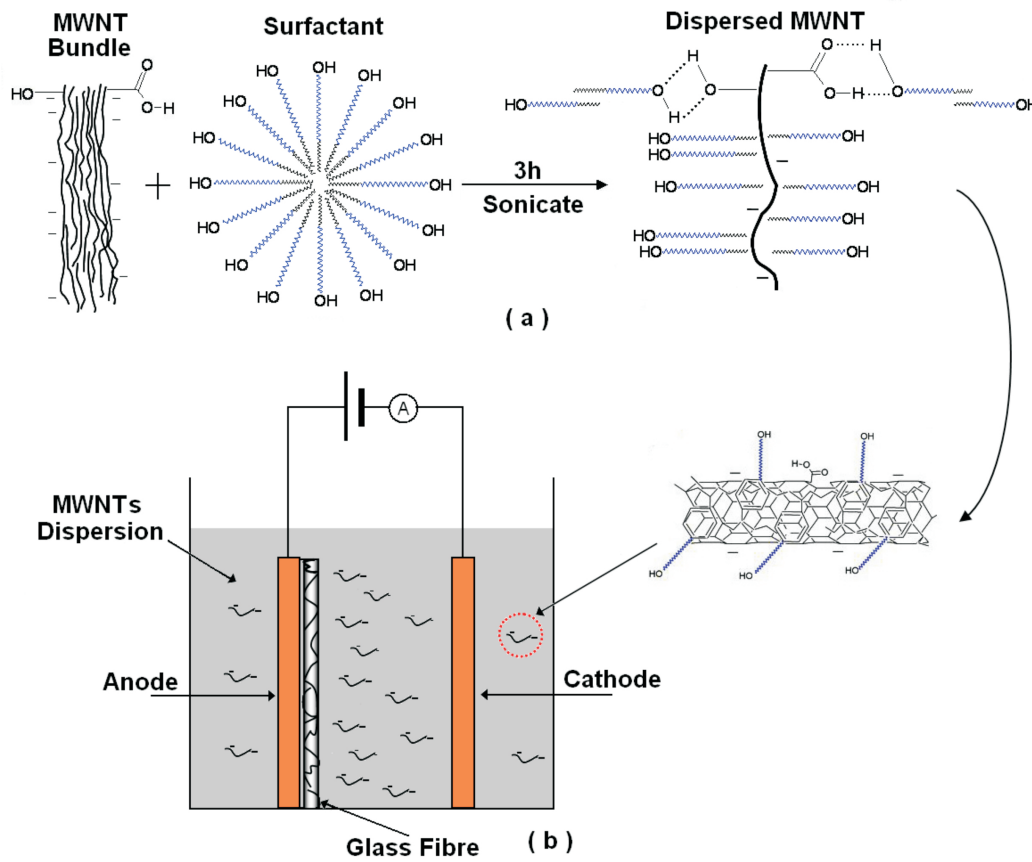


Figure 3.1: Schematic illustrations of (a) MWNTs dispersion process in water with surfactant and (b) deposition of MWNTs onto insulative glass fibre surface by the electrophoretic deposition cell [71]

Unlike carbon fibre, the glass fibre can not be used as electrode directly, due to its insulating property. Instead, we used two parallel copper plates with rectangular-shape ( $7\text{ cm} \times 2.5\text{ cm} \times 0.1\text{ cm}$ ) as cathode and anode. According to streaming potential results in Figure 3.2, the dispersed MWNTs and the hydrolyzed Glymo showed neg-

ative charge and would migrate towards the positive electrode, the anode was used as deposition electrode. The glass fibres were fixed on a thin plastic frame, and then the frame was mounted on the anode, the test set-up is schematically shown in Figure 3.1(b) [71]. EPD was carried out for 10 min at constant voltages of 4.5 V between two parallel copper plates as cathode and anode at a distance of 8 mm. With this potential difference, water dissociates slowly and potential gas formation as a result of hydrolysis in front of the electrode surface is not observed. The coated samples were dried at 40 °C vacuum oven for 8 h. Due to their very small size and well-dispersed state, the carbon nanotubes were able to penetrate into the spaces between the fibres and coagulate on the whole surface of fibre. In general, it is expected that one side of the fibre was always preferentially exposed to the “depositing” carbon nanotubes and the EPD technique has an inherent difficulty to achieve a homogeneous distribution of the carbon nanotubes on the round glass fibres. For optimization of coating morphology and thickness, the reverse side of the coated sample was deposited for the second time under the same conditions as the first cycle.

### 3.2.2 Dip coating method

To compare the quality of coating with EPD, dip coating method was utilized to deposit CNTs onto the glass fibre, which is the simplest and least expensive technology. Likewise, we firstly prepared the CNTs dispersion for forming conductive networks with more homogeneous and continuous nanotube distribution on the glass fibre surface. The weight ratio of MWNT versus Igepal CO970 is still 2:3, but the concentration of MWNT in dispersion is 0.5 wt%. Then, the glass fibres were dipped into a MWNT dispersion with the pH value of 5-6, withdrawn with their axes perpendicular to the solution surface, and dried in a vacuum oven at 40 °C for 8 h. Finally, the concentration of nanotubes on the glass fibre surface measured with an electronic balance was 2.3 wt% [80].

The different treatment conditions are summarized in Table 3.1. To check how many

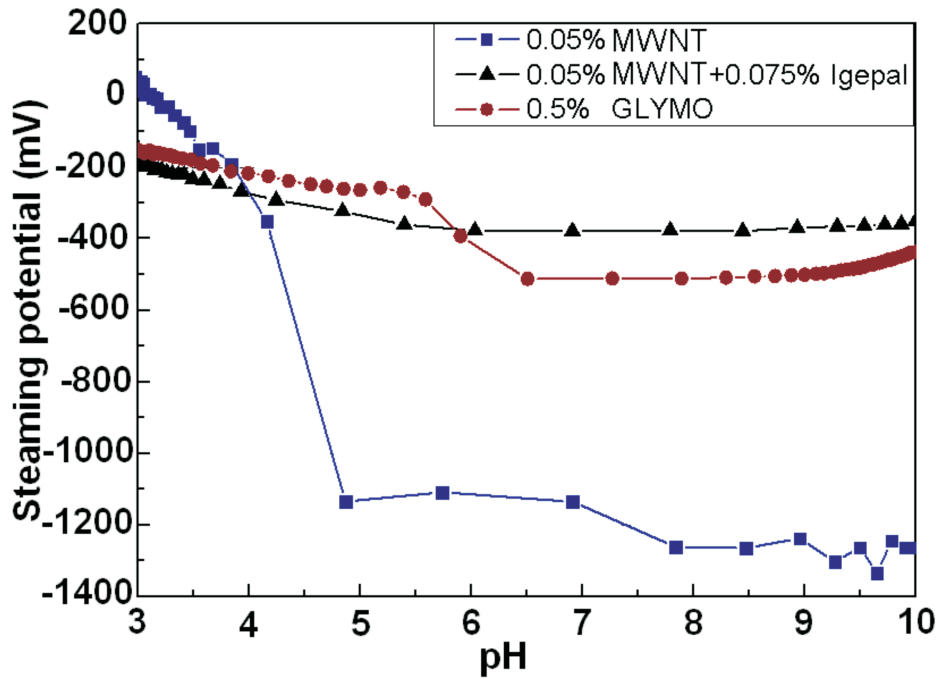


Figure 3.2: Streaming Potential tests. The MWNTs dispersions and Glymo solution are dependent electronegative on pH 6 - 7

MWNTs were successfully deposited onto glass fibres, the fibre mass was measured before and after depositing MWNTs. The mass increases of EPD-C fibre, EPD-G fibre and DIP fibre were 1.0, 0.96 and 1.8 wt%, respectively. Accordingly, taking as a rough estimate the mass density of MWNTs,  $\rho_{CNT} = 2 \text{ g/cm}^3$ , [81] the density of glass,  $\rho_{glass} = 2.7 \text{ g/cm}^3$  and aforementioned size parameters of MWNTs and glass fibre, the numbers of MWNTs per  $\mu\text{m}^2$  surface area of glass fibre could be calculated, which are 380, 360, and 680 for EPD-C, EPD-G and DIP fibres, respectively.

Table 3.1: Surface treatment conditions of AR glass fibres

Designation	Surface treatment conditions
Control	Unsize
DIP	Dip coated with 0.5 wt.% CNT
EPD-C	EPD coated with 0.05 wt.% CNT without Glymo
EPD-G	EPD coated with 0.05 wt.% CNT and 0.5 wt.% Glymo

### 3.3 Single fibre model composites

Single filaments were picked from various fibre bundles and were mounted within a dog-bone shaped silicone rubber mould. The epoxy resin and curing agent were thoroughly mixed and degassed prior to pouring in the mould. The samples were isothermally cured at 80 °C for 12 h and then slowly cooled down to room temperature. The dimensions of single fibre composite specimens for fragmentation tests were: 20 mm gauge length, 1.8 mm width, and 1.5 mm thickness.

### 3.4 Characterizations

#### 3.4.1 Topographic morphology

The morphologies of MWNT coatings on the glass fibres surfaces were investigated using an Atomic Force Microscopy (AFM) (Digital Instruments D3100, USA) and a Scanning Electron Microscope (SEM) (Ultra 55, Carl Zeiss SMT AG, Germany). The samples for SEM observation were coated by a 5 nm thick platinum layer.

Image mean roughness and maximum height roughness within the cursor box derived from ASME B46.1 are calculated for six fibre surfaces of AFM images. In tapping mode, a piezo stack excites a silicon cantilever's substrate vertically at its resonant frequency with a drive amplitude of 200 mV. As the cantilever is oscillated vertically, the reflected laser beam reveals information on the deflection of the cantilever and therefore indirectly or vertical height of the sample surface can be obtained.

#### 3.4.2 Single fibre tensile test

Tensile tests of single filaments were conducted on a FAVIGRAPH semiautomatic equipment (Textechno GmbH, Germany) at a strain rate of 0.5 min<sup>-1</sup>. Approximately 50 single fibres for each treated surface were used to determine the strength of fibre

at gauge lengths of 30, 20 and 10 mm, respectively. Based on a vibration method [82] in accordance with ASTM-D-1577-96 and DIN EN ISO 53812, the diameter of each selected fibre was determined.



Figure 3.3: The picture of the tensile test device for single filament: FAVIGRAPH semiautomatic equipment

### 3.4.3 Single fibre electrical resistance measurement

The technique applied to operate and measure the electrical properties of a single MWNT-glass fibre has been realized, as schematically outlined in Figure 3.4, where one fibre bridges two Cu electrodes on an epoxy substrate with small gap distances of 0.3, 0.5, 1.0, 2.2 or 3.0 mm. Without using conductive silver paste, the fibre was assembled carefully along a narrow channel ditch on the relatively soft Cu electrodes,



which was prefabricated by surface indentation using the same kind of glass fibre. In this configuration a large amount of MWNTs on the fibre surface was forced to attach to the electrodes under compression. Besides the surface forces, van der Waals and capillary forces are enough to establish a sufficiently intimate electrical and mechanical contact between the nanotubes and the electrodes. [83] Approximately forty fibre specimens for each condition were measured. Two-point conductivity measurements were carried out with an LCR-digital multimeter (VC-4095) for resistance values of the single MWNT-glass fibre.

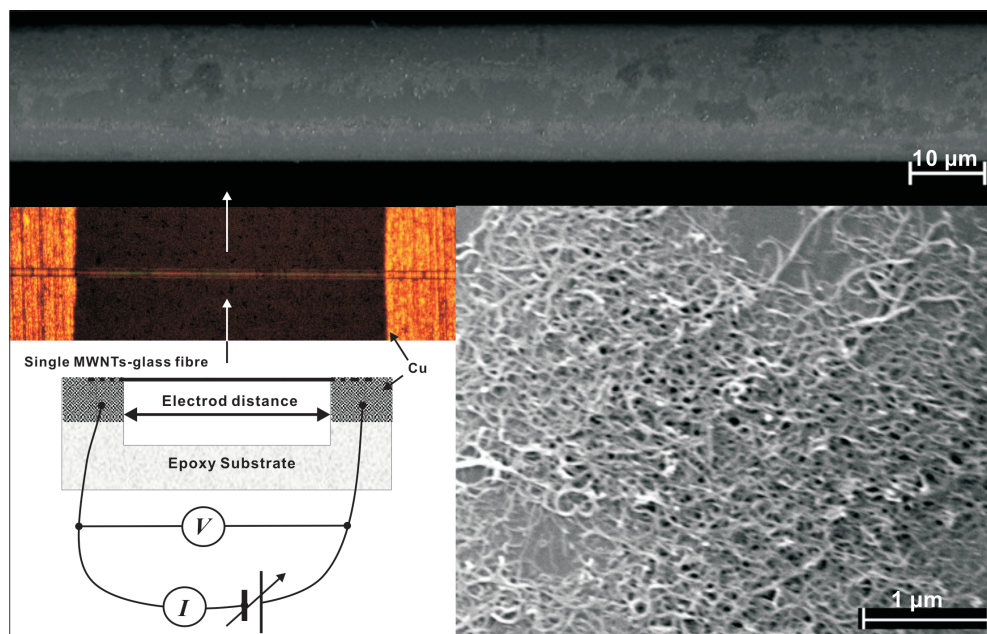


Figure 3.4: Schematic drawing for the resistant measurements of single MWNTs-glass fibre. The upper optical image of the glass fibre between two Cu electrodes. The low and high-magnification FE-SEM images highlight an inhomogeneous distribution and randomly oriented interpenetrating MWNT network structure on the glass fibre surface [80]

### 3.4.4 Interfacial adhesion strength test

#### Single fibre model composite fragmentation test

The fragmentation test has been used for assessing interfacial shear strength, where the tensile load in the specimen is transferred to the fibre by shear stresses in the matrix through the interphase. The fibre keeps breaking until the fragments become too short to build up sufficiently high tensile load to cause further fragmentation with increasing specimen strain. Based on a force balance in a micro-mechanical model of Kelly and Tyson [84, 85], the interfacial shear strength is given by:

$$\tau = \frac{\sigma_c}{2(l_c/d)} \quad (3.1)$$

where  $d$  is the fibre diameter,  $\sigma_c$  is the fibre fracture stress at critical fragment length of fibres  $l_c$ .  $\sigma_c$  is usually obtained through a linear extrapolation of experimental data on the fibre strength measured in single fibre tensile tests at longer gauge length. Here,  $l_c$  is calculated by  $l_c = 4/3l_a$ ,  $l_a$  is the average fragment length [86]. The ratio  $(l_c/d)$  is referred to as the critical aspect ratio at constant fibre strength, which is an inverse measure of the interfacial shear strength. More than five specimens for each kind of fibre surface treatment were measured.

Regarding the fragmentation configuration, it is known since Mullin et al. [88] that three modes of fracture may arise in a single fibre composite during a fragmentation experiment, based on the degree of interfacial adhesion: (i) In the case of a relatively strong interface, the initial fibre break is followed by a disk-shaped matrix crack, as shown in Figure 3.5(a). (ii) In the presence of a relatively weaker interface, the initial fibre break is immediately followed by a limited interfacial debonding break (Figure 3.5(b)). (iii) In the case of a relatively strong interface but with a matrix that has relatively lower shear than tensile strength capability, the initial fibre break is followed by a double cone matrix crack (Figure 3.5(c)) [87, 88]. Sometimes, mixed failure modes could be observed, it indicates that the interphase adhesion strengths are het-

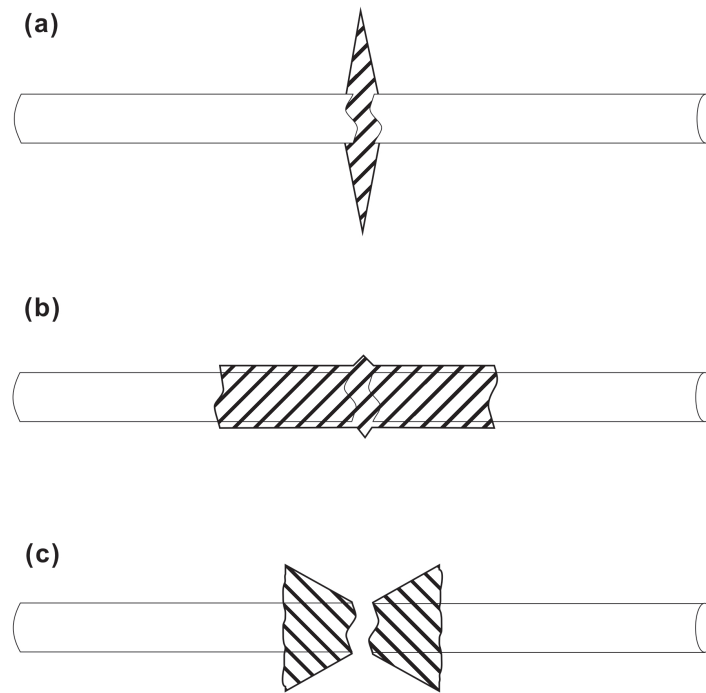


Figure 3.5: The three modes of fracture that arise in a single-fibre composite during a fragmentation experiment: (a) strong interface-the initial fibre break is followed by a disk-shaped matrix crack (b) weak interface-the initial fibre break is simultaneously accompanied by interfacial debonding; (c) strong interface but with a matrix that has relatively lower shear than tensile strength capability-the initial fibre break is followed by a double cone matrix crack [87, 88]

erogeneous in composites. Optical microscopes (Nikon Optiphot-2, Keyence VHX-600) with transmitted polarized light were used to in situ detect the lengths and fringe patterns of fibre fragmentation within the epoxy matrix.

### Pull-out test

In this test, one end of a single fibre is embedded vertically in a resin matrix to a controlled depth. This sample is placed in a special built specimen carrier of the pull-out apparatus and the other end of fibre is fixed with a special glue to the force sensor of the machine. The fibre is pulled from the cured matrix and the load as well as extension is recorded in a force-displacement curve. The quality of interfacial bonding is characterized by calculating the apparent interfacial shear strength (apparent IFSS,

$\tau_{app}$ ):

$$\tau_{app} = \frac{F_{max}}{\pi d_f l_e} \quad (3.2)$$

where,  $F_{max}$  is the maximum force,  $l_e$  is the embedded length. The pull-out test was carried out on a home-made pull-out apparatus (see Figure 3.6) with force accuracy of 1 mN and displacement accuracy of  $0.07 \mu\text{m}$ . The test was done with a loading rate of  $0.01 \mu\text{m/s}$  at  $23^\circ\text{C}$  and 50 % RH. Every type of fibre was evaluated by about 15 to 20 samples.

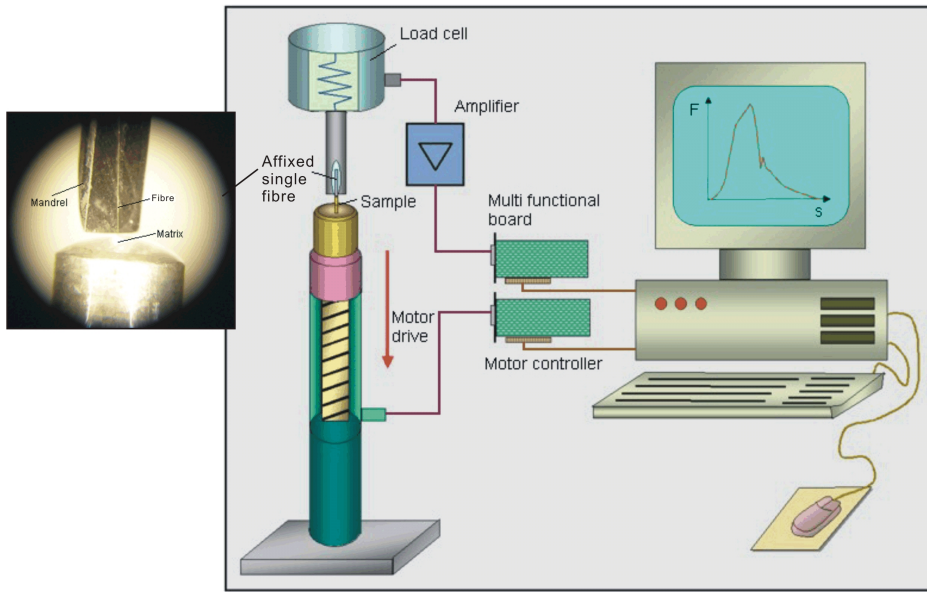


Figure 3.6: The schematic diagram of single fibre pull-out test equipment in Leibnitz Insitute of Polymer Research

### 3.4.5 Piezoresistivity of single fibre and single fibre composite

To investigate the piezoresistive effect, the electrical resistance was recorded as the single glass fibre underwent uniaxial tensile or cyclic loading using the Favigraph semiautomatic fibre tensile tester (Textechno, Germany) equipped with a 1N load cell, according to DIN EN ISO 5079 and DIN 53835-2, respectively. Assuming a circu-

lar cross-section, a relation between the resonance frequency  $\gamma$  and the fineness  $\sigma_t$  at known pre-load  $F_\gamma$  and gauge length  $L$  is defined as: [89, 90]

$$\sigma_t = \frac{F_\gamma}{4 \cdot \gamma^2 \cdot L^2} \quad (3.3)$$

The tests have a gauge length of 20 mm and a cross-head velocity of  $0.2 \text{ mm min}^{-1}$  for both loading and unloading with a strain amplitude of 2 %, where EPD-C fibre was used for testing at 50 % RH and 23 °C. To ensure good electrical contact, gold was sputtered to a thickness of about 60 nm on the two ends of the single MWNT-glass fibre; the middle part of fiber (with a length of 5 mm) was left uncovered. The specimen was in turn clamped between two plates coated with conductive silver paste (Acheson Silver DAG 1415M) serving as electrodes.

A single or three individual fibres were mounted within a dog-bone shaped mould. A commercial DGEBA-based epoxy resin and curing agent were thoroughly mixed and degassed prior to pouring in the mould as polymer matrix. The samples were isothermally cured at 80 °C for 12 h and then slowly cooled down to room temperature with the dimension of 5 mm gauge length, 1.5 mm width and 0.5 mm thickness, the content of MWNTs is less than  $4 \times 10^{-4} \text{ wt\%}$  in the composite. The properties of fibre and cured epoxy are listed in Table 3.2. The electrical resistance of the single fibre model

Table 3.2: Mechanical properties of AR-glass fibre and epoxy matrix

Fibre	
Axial modulus (GPa)	75
Transverse modulus (GPa)	75
Axial Poisson's ratio	0.17
Transverse Poisson's ratio	0.17
Matrix	
Young's modulus (GPa)	2.7
Poisson's ratio	0.34

composite under tensile load was monitored simultaneously with mechanical stress-strain behavior (Figure 3.7). The stress-strain curve was detected by FAVIGRAPH

Semiautomatic Equipment (Textechno GmbH, Germany) with a test velocity at 0.2 mm/min. A Keithley 2000 multimeter with constant test current ( $10\ \mu\text{A}/700\ \text{nA}$ ) and a Keithley 6517 A high resistance meter with constant source voltage ( $40\ \text{V}/400\ \text{V}$ ) were used for electrical resistance measurements. The ends of the samples and test grips were painted with silver paste in order to form an ohmic contact. To demonstrate a potential application for detecting the propagation of microcracks in the glass facade, the single MWNT-glass fibre was glued onto the surface of a glass slide by epoxy, and one end of the glass slide with a small surface scratch was stretched to about 40 N until the crack propagation was observed. The experiments of the resistance changing

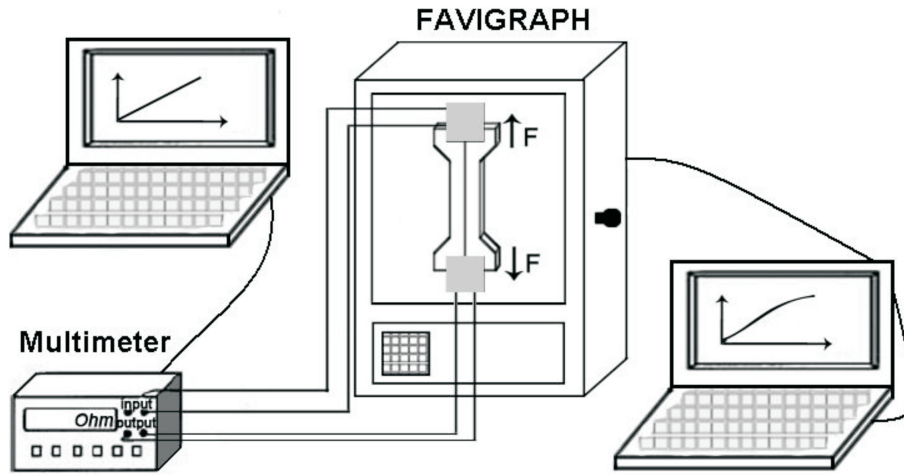


Figure 3.7: Schematic of experimental setup of electrical resistance measurement for the single fibre model composites subjected to tensile loading

with temperature were carried out in a hot-stage (Linkam LTS350 Heating/Freezing, UK) from  $25\ ^\circ\text{C}$  to  $80\ ^\circ\text{C}$  with a heating rate of  $5\ \text{K/min}$ . At room temperature, the resistance of the switch was immeasurable (above  $210\ \text{G}\Omega$ ), which was acquiesced to equal with the resistance value of epoxy ( $10^{15}\ \Omega$ ) in order to normalize the resistance value. Additionally, the observation of switch actuated by illumination was conducted under a lamp of 60 W. The distance between lamp and sample was about 200 mm.

To investigate the interphase evolution during tensile loading, the specimens were polished until the fibres were exposed on the surface. The break junction of MWNTs

networks in the interphase were observed using a SEM (Ultra 55, Carl Zeiss SMT AG, Germany), after sputtering a 5 nm thick platinum layer onto samples. Optical microscopes (Nikon Optiphot-2, and Keyence VHX-600) with transmitted polarized light were used to detect photoelastic phenomena with the strain.

### 3.4.6 Thermal analysis

The curing of epoxy and crystallization of PET were measured by the modulated differential scanning calorimetry (MDSC) (Q2000 MDSC, TA Instruments, USA) during isothermal or dynamic processes. Samples used for DSC experiments were sealed in aluminum hermetic pans. To compare with the resistance results, MDSC was conducted at the same heating and cooling rate as hot-stage. From the results of the DSC experiments, the governing equations to calculate the degree of conversion of dynamic cure  $\alpha$  and the degree of conversion of isothermal cure  $\beta$  of thermosetting resin were determined as follows [91]:

$$d\alpha/dt = (1/H_U)(dQ/dt) \quad (3.4)$$

$$d\beta/dt = (1/H_T)(dQ/dt) \quad (3.5)$$

where  $dQ/dt$  is the instantaneous rate of generated heat;  $H_U$  and  $H_T$  are total heat generated in the dynamic and isothermal scanning of DSC, respectively.  $\beta$  was treated as a reference parameter in the investigation of isothermal curing to compare with the resistance results.

### 3.4.7 Infrared analysis

Fourier transform infrared spectroscopy (FTIR) was chosen to analyze the chemical reaction during dynamic polymerization. Infrared analysis was performed using a Fourier transform infrared spectrometer (Equinox 55, Bruker) equipped with a temperature-

controlled cell which was continuously purged with nitrogen gas. A series of spectra on epoxy mixers sandwiched between two potassium bromide (KBr) pellets was obtained at each cure temperature, which ranged from ambient temperature to 200 °C, at 3 K/min. Each spectrum from 4000 to 600  $\text{cm}^{-1}$  was averaged over 32 scans taken, at 2  $\text{cm}^{-1}$  resolution. The methyl group absorbance peak,  $\nu_{C-H} = 2962 \text{ cm}^{-1}$ , was used as an internal standard. The nomalized relative intensity,  $p$  of a functional group versus temperature is calculated by:

$$p = \frac{A_{band}/A_{2962}}{2} \quad (3.6)$$

where  $A$  is the absorbance at various temperature, subscripts “*band*” refer to the wavenumber of a given functional group.



## 4 Results and Discussions

### 4.1 MWNTs coating on the glass fibre

Through visual inspection, both EPD and Dip coating methods have successfully deposited MWNTs onto the glass fibre, but the qualities of coatings are different. The electrical resistivity of the single coated fibre is dependent on the distribution and the structure of CNTs network, thus the measurement of resistivity can be used to evaluate the quality of coating. The DC electrical resistance  $R$  of a single glass fibre with MWNT networks was measured. As shown in Figure 4.1, the DC resistance  $R$  of the single fibre was in the range of  $10^4$  up to  $10^8 \Omega$ , and the resistance increased with increasing electrode-electrode distance,  $L$ . Accordingly, the calculated specific volume resistivity  $\rho_{glass} = \pi d^2 R / (4L_e)$ , for the MWNT coated glass fibre with a diameter of  $d = 12 \mu\text{m}$ , was approximately  $10^4 \Omega \text{ cm}$ , which was in the semiconductive range and significantly lower than the volume resistivity over  $10^{15} \Omega \text{ cm}$  of the common electrical insulating glass fibre. This is attributed to the excellent conductivity of carbon nanotubes. Thus, depositing MWNTs onto the glass fibre surface by either EPD or dip coating methods, the electrically semiconductive glass fibres can be obtained, both processes achieve the similar order of magnitude of resistance. However, note that the actual quantity of MWNTs deposited onto the glass fibre surface through the EPD method is significantly lower than those obtained from dip coating method, which based on the results of weight increase after deposition. It reflects that the EPD method deposited much more homogeneous nanotubes networks onto the fibre sur-

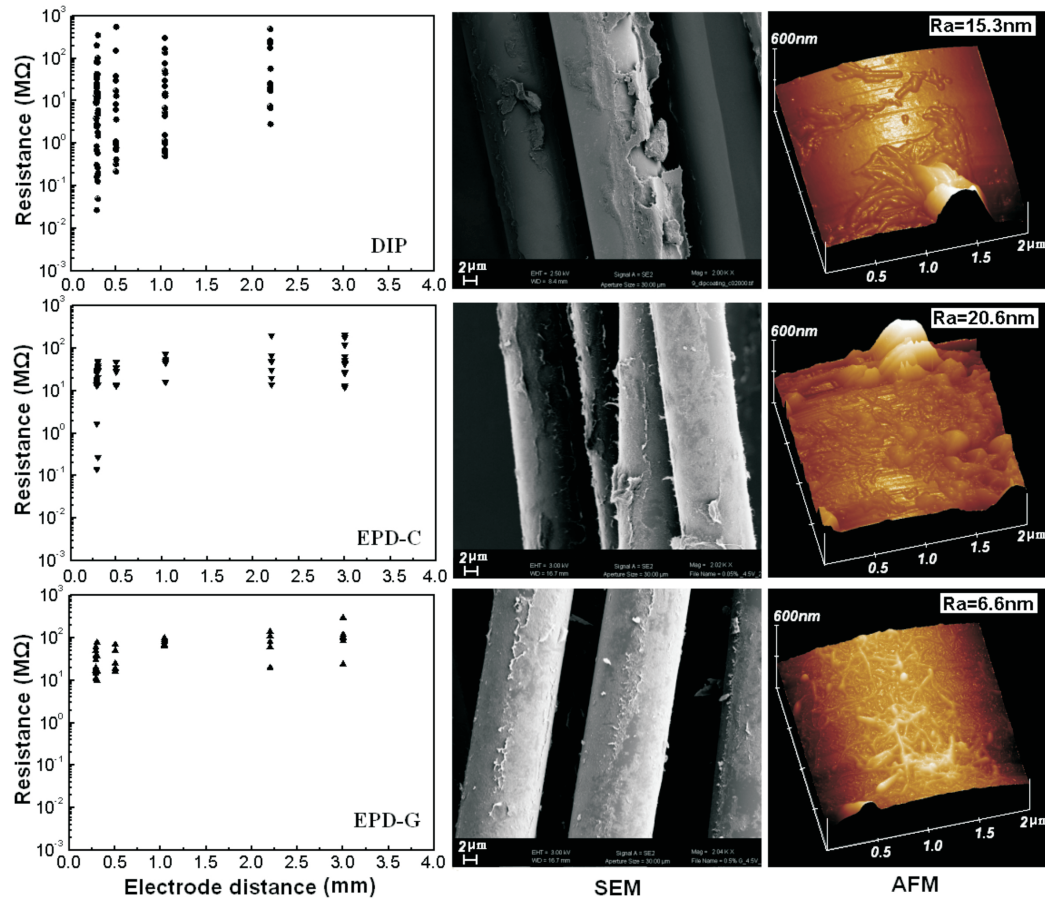


Figure 4.1: The DC electrical resistance of single fibres as a function of electrode distance (left) together with SEM (middle) and AFM (right) topographic images of differently coated fibres [71]

faces and merits further optimization of the deposition process. The suggested mechanism for EPD in the case of carbon nanotubes is the particle double layer distortion due to induced electric fields and particle coagulation on the substrate which is based on the Derjaguin-Landau-Verwey-Overbeek (DLVO) theory. A quantitative estimate of the relationship between stability of suspension in terms of interparticle forces and energies of interactions that exist between colloidal particles and other surfaces in a liquid has been described by the classical DLVO theory established by Derjaguin and Landau [92] and Verwey and Overbeek [93]. It assumes that the effect of two forces is additive, and by combining the effect of electrostatic repulsion and Van der Waals attraction between two particles [94]. When the particle lyosphere system (the counter

ions from liquid around the charged particle forms what is called diffuse double layer or lyosphere) moves, fluid dynamics and applied electric field will distort the double layer envelope in a way such that it becomes thinner ahead, and wider behind the particle. The counter ions in the extended “tail” will tend to react with these accompanying cations in high concentration around them. As a result of this reaction, the double layer around the “tail” of the particle will thin so that the next incoming particle (which has a thin leading double layer) can approach close enough for London Van der Waals (LVDW) attractive force to dominate and induce coagulation/deposition [75, 94]. During deposition electro-hydrodynamic or electro-osmotic effects assemble MWNTs into arrays.

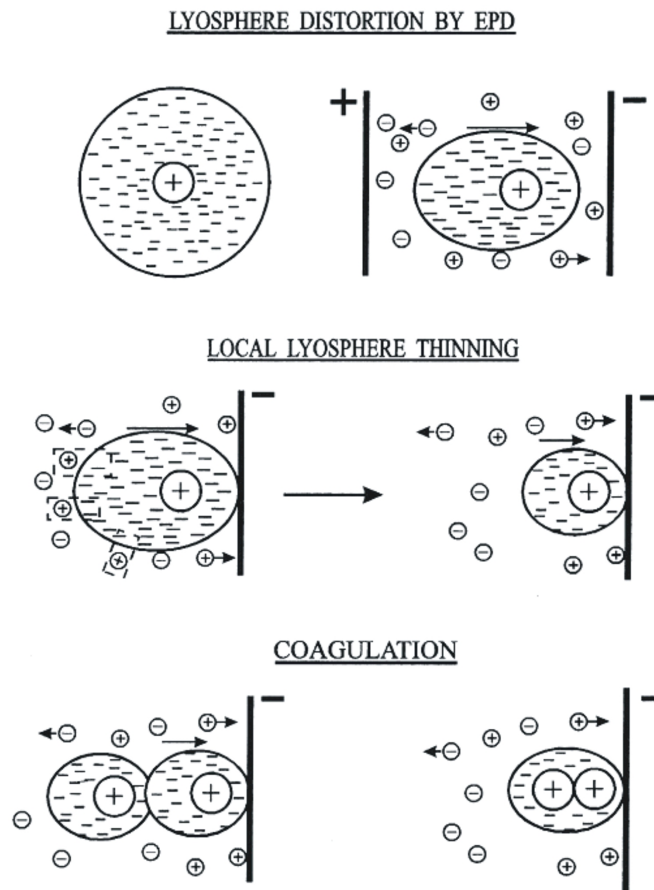


Figure 4.2: Electrical double layer distortion and thinning mechanism for electrophoretic deposition [75, 94]

The variation and distribution of the resistance datum were compared to identify whether the resistance was affected by coating morphology. The distinguishable fibre surface characteristics determined by SEM and AFM (Figure 4.1) under various treatment conditions confirm that the EPD method deposited much more homogeneous nanotubes network onto the fibre surfaces, while the dip coating method deposited inhomogeneous nanotubes networks. The more uniform and homogeneous MWNT coating is largely responsible for the resistance values of the fibre prepared by EPD method distributing significantly narrower than those by dip coating. Altogether, it was found that the EPD method provides an efficient process for depositing MWNTs onto the glass fibre surface [71].

## 4.2 Interfacial adhesion strength of composites

Biological material is an indubitably perfect composite, its structure is generally hierarchical, spanning many length scales. Bones serve as an example of those hierarchically structured biomaterials which is a fracture-resistant composite of collagen, a comparatively soft fibrous protein, and brittle calcium phosphate mineral [95, 96]. They have been studied with the fibre-reinforced composite model [97] which shows features of multi-scale fibres and heterogeneous interphases (Figure 4.3). The nanometer-scale interphase of mineral-protein strongly influences the mechanical property of bone, where the apparent reinforcement effect is related to the cooperation of the strong interfacial adhesion strength and the weak interphase serving to inhibit crack propagation or as mechanical damping elements [98]. For materials scientists, there is much to be learned from studying how the structural organization of biological materials relates to their extraordinary properties. Accordingly, it is reasoned that an appropriate nanoscale interphase by CNTs as minerals as in biological bone may improve the interfacial adhesion strength of traditional glass fibre-reinforced plastics. The results of the fibre

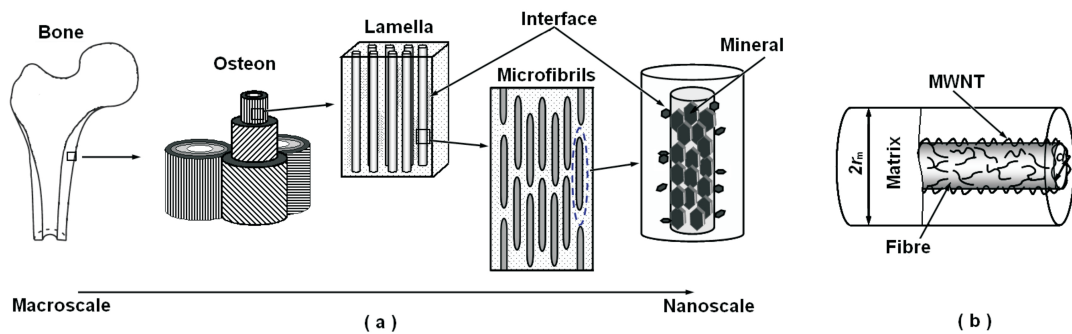


Figure 4.3: (a) Hierarchical structural organization of bone in a macroscopic, microscopic, and nanoscale point of view [98, 99]; (b) the schematic illustration of the composite cross section model mimicking the biological bone with concentric layers of fibre, MWNTs and matrix [71]

fragmentation tests for the differently treated fibre specimens are shown in Figure 4.4. As expected, the control fibre has the highest critical aspect ratio, which corresponds to the lowest interfacial shear strength (see section 3.4.4) for the fibres with simi-

lar values of tensile strength (Table 4.1). In contrast, the interfacial shear strength is

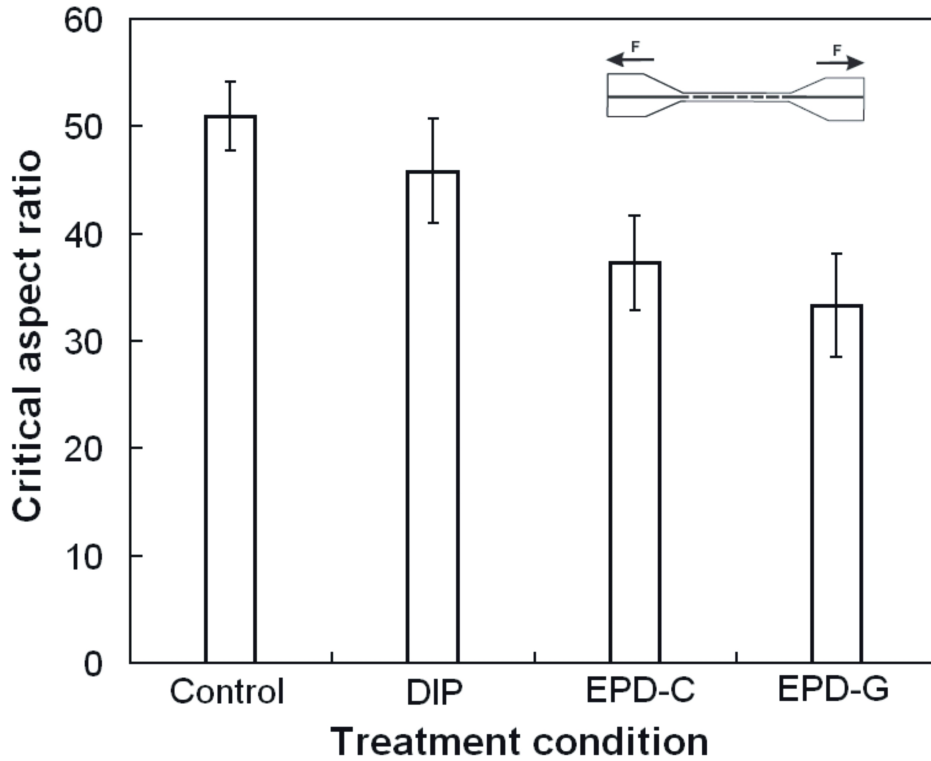


Figure 4.4: Comparison of the critical aspect ratios of single fibre composites with different surface conditions in fragmentation test. The error bars represent standard deviations. The inserted figure is a schematic diagram of single fibre model composite under tensile load

enhanced by the MWNT coating through EPD method, particularly the sample with Glymo achieves the maximum interfacial shear strength as indicated by the lowest critical aspect ratio, which is consistent with the results of pull-out test. The reason of enhancement might arise from different nanotube related toughening mechanisms [100], including glass fibre/nanotube/matrix interfacial debonding, nanotube pull-out, interfacial crack bridging and so on. The micro-mechanical interlocking contributes mainly to the frictional bond after fibre debonding, an effect similar to the clench of gears may exist between CNTs and cross-linked epoxy molecules [101], which can be explained by the AFM images of the fibre surfaces after pull-out test, in Figure 4.5, the more amounts of matrix are adhered onto the EPD fibre than that of control fibre. It is clear that, if glass fibres were unevenly etched so that their surface roughness was

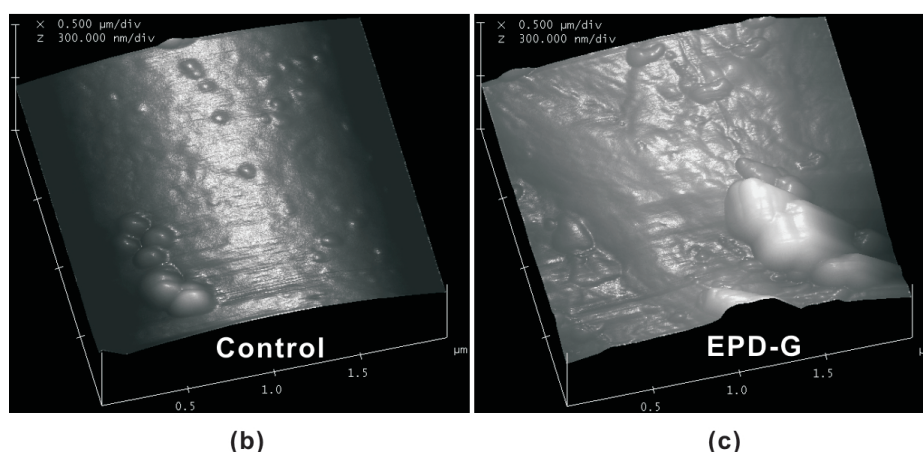
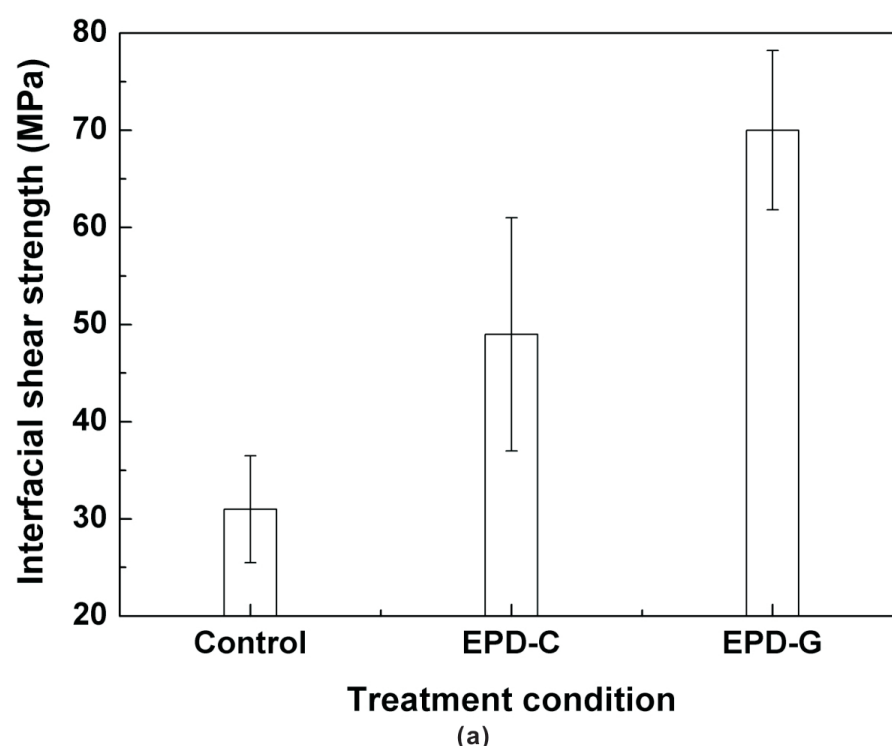


Figure 4.5: (a) The interfacial shear strength based on pull-out test under different treatment conditions. The fracture surfaces are observed through AFM Tapping mode after pull-out test: (b) the surface of Control fibre; (c) the surface of EPD-G fibre

greatly increased, the composites should have different interfacial strength from the present case due to the MWNTs related complex mechanisms. The potential chemical reactions between epoxy and the carboxy functionalized MWNTs as well as hydrogen bonding contributed to the improvement of the interfacial strength either. In presence of silane coupling agent, the reactions of epoxide-carboxy, epoxy-amine, and silanol-

silanol gave rise to chemically covalent bonds around glass fibre, MWNT, surfactant, and epoxy [102, 103]. Additionally, the coating on the surface of the fibres by EPD did

Table 4.1: Average single fibre tensile strength for different gauge length ( $L_0$ )

Designation	Average single fibre tensile strength (MPa)		
	$L_0 = 10 \text{ mm}$	$L_0 = 20 \text{ mm}$	$L_0 = 30 \text{ mm}$
Control	$2102 \pm 321$	$1999 \pm 260$	$1890 \pm 243$
DIP	$1473 \pm 321$	$1333 \pm 219$	$1301 \pm 247$
EPD-C	$2014 \pm 307$	$1974 \pm 268$	$1840 \pm 284$
EPD-G	$2035 \pm 256$	$1864 \pm 218$	$1829 \pm 293$

not lead to any discernable decrease in single fibre tensile strength as revealed in Table 4.1. However, the DIP fibre strength was decreased. The same findings of reduced strengths of glass fibres due to agglomerated carbon nanotube-epoxy coatings have also been reported [104]. This can be understood by noting that the bigger the flaw arising from irregular coating present in the surface layer, the lower is the expected value of the ultimate tensile strength of the fibre [105]. Consequently, the inhomogeneous and agglomerated MWNT coating causes an irregular stress distribution along interphase region which will be discussed in the following part.

From mechanics point of view, the stress transfer behaviour between fibre and matrix should be strongly affected by interfacial crack initiation and propagation when MWNTs were extensively distributed in the interphase region. Basing on the fraction of the phases in the composites, we could consider the simplest analysis of our composites with MWNT-rich interphases as schematically shown in Figure 4.3(b). Since the carbon nanotubes were generally randomly distributed onto the fibre, the interphase could be considered as randomly oriented discontinuous MWNTs-epoxy layer. Taking a rough estimate, the interphase modulus,  $E_{interphase}$ , could be calculated using the following equation [106]:

$$E_{interphase} = \left[ \frac{3}{8} \left( \frac{1 + 2(l_{CNT}/d_{CNT})\eta_L V_{CNT}}{1 - \eta_L V_{CNT}} \right) + \frac{5}{8} \left( \frac{1 + 2\eta_T V_{CNT}}{1 - \eta_T V_{CNT}} \right) \right] E_{epoxy} \quad (4.1)$$



where,

$$\eta_L = \frac{(E_{CNT}/E_{epoxy}) - 1}{(E_{CNT}/E_{epoxy}) + 2(l_{CNT}/d_{CNT})}$$

$$\eta_T = \frac{(E_{CNT}/E_{epoxy}) - 1}{(E_{CNT}/E_{epoxy}) + 2}$$

and  $E_{CNT}$ ,  $E_{epoxy}$  are the elastic modulus of MWNT and epoxy, respectively,  $E_{CNT}$  is about 1.8 TPa [9].  $l_{CNT}$  and  $d_{CNT}$  are the average length (1.5  $\mu\text{m}$ ) and diameter (9.5 nm) of MWNTs in this research. In accordance with the average and maximum roughness determined by AFM, we assumed the range of thickness of MWNT layer and associated thickness of interphase are ranging from few tens to few hundreds of nanometers. The cross-sectional observation of MWNT-glass fibre/epoxy composite by SEM and AFM confirmed that most nanotubes are located in the interphase region, see Figure 4.6 [80]. When the fibres are mixed with the epoxy, the MWNTs do not recognisably migrate away from the glass fibre surface due to the entangled network nature of nanotubes. The volume fraction  $V_{CNT}$  of MWNTs in interphase region can be estimated according to the weight fraction and density [107]. Using these equations, the  $E_{interphase}$  could be calculated obviously higher than epoxy, which was also experimentally confirmed by AFM-nanoindentation. We further considered the mean elastic modulus of matrix  $E_m$  around fibre, when the MWNTs have not been introduced into the interphase,  $E_m$  was equal to  $E_{epoxy}$ . Because of the high modulus MWNT-interphase,  $E_m$  was increased to  $E'_m$  according to the rule of mixtures,

$$E'_m = E_{interphase}V_{interphase} + E_{epoxy}(1 - V_{interphase}) > E_{epoxy} \quad (4.2)$$

where  $V_{interphase}$  is the volume fraction of interphase in matrix. When the yield stress is assumed to be constant, the critical fibre length  $l_c$  based on the shear lag theory could be related to the fibre and matrix properties, as was derived by Galiotis et al. [108] and

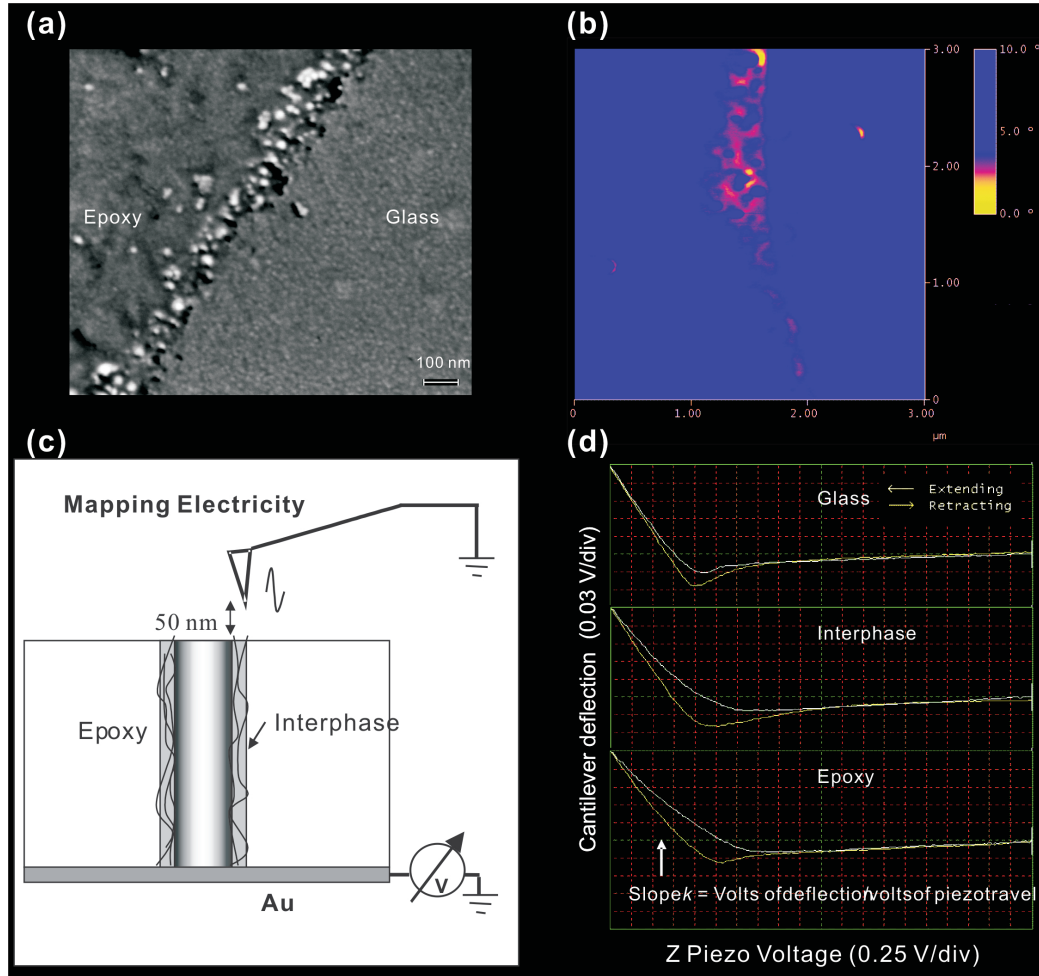


Figure 4.6: (a) FE-SEM and (b) EFM images of MWNT-rich interphase in MWNTs-glass/epoxy composite; (c) schematic diagram for electrical mapping cross-section of composites with MWNT-rich interphase by EFM; (d) typical nanoindentation force curves on fibre, interphase, and epoxy represent the cantilever deflection signal for one complete extension/retraction indentation cycle of the piezo. The initial slope  $k$  of the retracting curve represents the cantilever deflection signal versus voltage applied to the piezo (i.e., indentation displacement in the vertical direction). A softer material would result in less deflection of the cantilever under a given indentation displacement, which provides qualitative information about the elasticity of specimen surface. The slope of indentation on the interphase showing higher value than that of indentation on the epoxy matrix actually demonstrates the higher stiffness of interphase [80]

Asloun et al. [109]:

$$\frac{l_c}{d} = \left[ \frac{(1 + \nu_m)(E_f - E_m) \ln(2r_m/d)}{E_m} \right]^{1/2} \quad (4.3)$$

where  $r_m$  is the radius of the cylindrical matrix around the fibre;  $E_f$  is the fibre tensile modulus; the Poisson ratio of matrix  $\nu_m$  is considered as invariable after interphase being introduced. Qualitatively and consequently,

$$\frac{l_c}{d}|_{E_m=E'_m} < \frac{l_c}{d}|_{E_m=E_{epoxy}} \quad (4.4)$$

the critical aspect ratio was decreased when the interphase strength between fibre and bulk matrix was enhanced by MWNTs. This caculated result offers a theoretical evidence for the previous fragmentation test. Furthermore, the morphology of MWNT coating on the fibre surface influenced not only electrical resistance as aforementioned but also interfacial shear strength. The fibre fragment lengths under the different treatment conditions were examined using Weibull distribution analysis in Figure 4.7. In

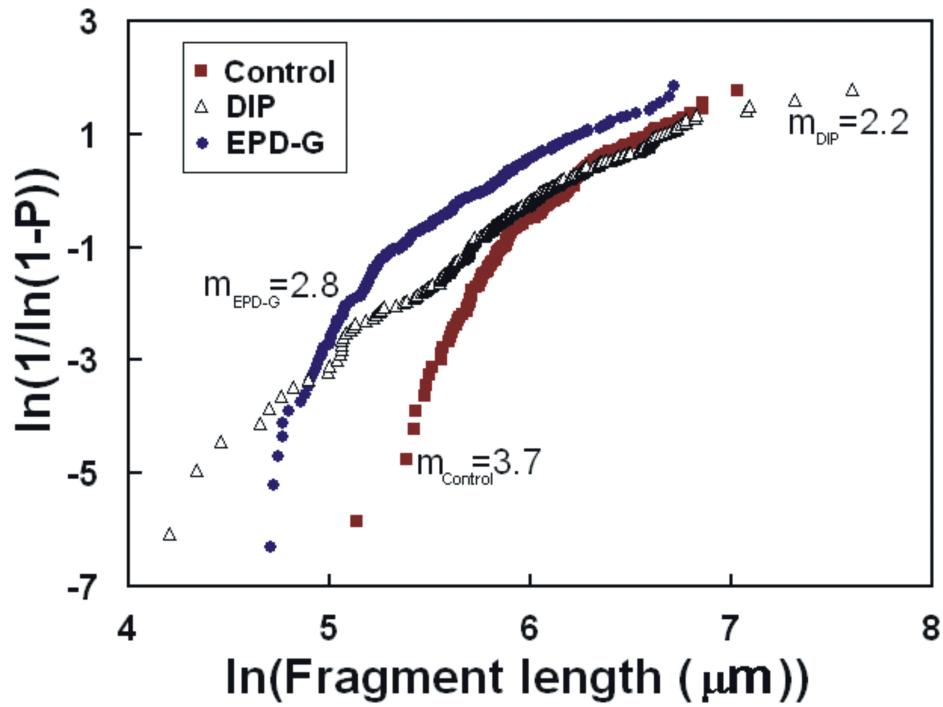


Figure 4.7: Comparison of the Weibull distribution of fibre fragmentation behaviour in single fibre composites with different surface conditions. The fragment length distribution of DIP fibre is the widest with the smallest  $m$ , which designates the Weibull shape parameter. The error bars represent standard deviations

these cases, the irregular MWNT distribution along the fibre causes non-uniform inter-

phase structures and properties (strength/stiffness). The cumulative distribution function  $F(l)$  of the fibre fragment lengths for single fibre composite tensile test is assumed to have the Weibull distribution form [84]:

$$F(l) = 1 - \exp\left[1 - \left(\frac{l}{l_0}\right)^m\right] \quad (4.5)$$

where  $m$  is Weibull shape parameter and  $l_0$  is Weibull scale parameter,  $l$  is the fibre fragment length. Associated with larger variation of interfacial shear strength, the larger  $m$  the more uniform is the fibre fragment length distribution, the more homogeneous are the structures and properties of interphase.

Then three different interphase structures were proposed: (1) homogeneous interphase; (2) mid-homogeneous interphase; (3) inhomogeneous interphase. Figure 4.8 shows the birefringence patterns under polarized light of single fibre model composites together with the schemes for these proposed interphases and the stress profiles along the fibre when the fragment number reached saturation. Clearly, the stress birefringence of control fibres and DIP fibres suggests that the interphases suffered from extensive shear stresses and the crack tended to expand along the interphase. Through focusing on the fibre break point, the apparent matrix crack failure mode could be observed in the coated fibre samples, which indicated improved interfacial strength due to the presence of the MWNT coating [87, 88]. The control fibre with homogeneous surface possessed the highest value of the Weibull shape parameter  $m$ , suggesting uniform interfacial adhesion. The interphases for fibres treated by EPD method were classified into the mid-homogeneous, since their Weibull shape parameter value is between control fibre and DIP fibre. Due to the differences in thickness of the MWNT layers or the heterogeneous adhesion modes from MWNTs or Glymo, the reinforcement effect was unequal along the whole fibre. Both strong bonding and relatively weak bonding coexist, leading to wider distribution of fragment lengths. It is interesting to note that the coexistence between strong interphase and weak interphase is similar to the biological bone structure. Besides the apparent reinforcement effect from the strong interphase,

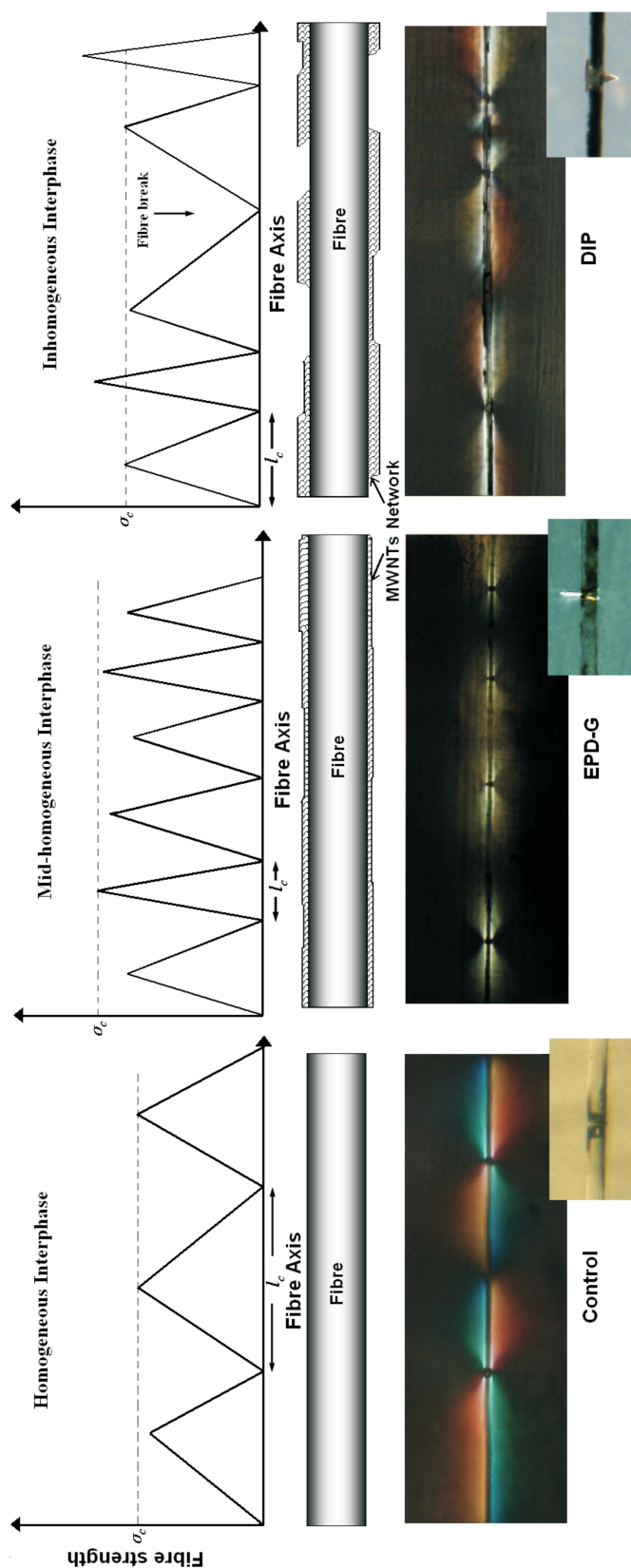


Figure 4.8: Three kinds of stress profiles along the fibre axis as a function of position when fracture number reaches its saturation; the birefringence patterns are shown by cross-polarized light for saturation at a magnification of ten. Insert images are the enlarged views of broken points, the interfacial debonding failure mode for control and the matrix crack failure mode for EPD-G and DIP systems were observed [71]

the weak interphase serves to inhibit crack propagation or acts as mechanical damping elements [98]. Consequently, the mid-homogeneous interphase with EPD fibre has the strongest interfacial strength which was confirmed by the shortest fragment length. In contrast, DIP fibre was defined as the inhomogeneous interphase with the lowest Weibull shape parameter  $m$ , which was strongly consistent with the aforementioned discontinuous coating topographic morphology and data scatter in electrical resistance of single fibre.

In summary, the EPD fibres gained higher interfacial shear strength without degradation of the fibre strength compared with the control fibre and DIP fibre. The interfacial shear strength of single EPD fibre composites exhibited more than 30 % improvement, irrespective of whether the coating includes silane coupling agent or not.

### 4.3 *In-situ* strain sensor

It is well known that most materials are susceptible to damage in the form of microcracks, which are usually considered negative and detrimental to the overall mechanical properties of the material [110–112]. The initiation and growth of microcracks induced by mechanical stresses as well as thermal fatigues are difficult to detect at an early stage. In absence of an advance warning, the prevention of catastrophic failure of materials is thus almost impossible. Early detection and eventually even the utilization of microcracks remain two of the most challenging tasks in materials science.

In order to early monitor internal microcracks of a material immense efforts have been made over the last decades. Experiments have been reported on embedding optical fibres, piezoelectric sensors/actuators as well as conductive fillers in polymer to check the variations of time-frequency, acoustic emission, Raman band shift signals and so on [113–115]. However, an embedded sensor has detrimental effects on the integrity of the structure and the implementation of complex equipment remains a technical challenge for field application [116, 117]. Through embedding CNTs in a sizing or polymer matrix to form electric pathways, the achieved non-uniformly and uniformly dispersed CNTs in composites have successfully been used as health sensors to monitor damage. [66, 118, 119] Recently, a CNT yarn strain sensor with excellent repeatability and stability was developed by directly embedding the yarn in an epoxy resin [67]. As a long-standing problem in FRP composites, internal microcracks that normally occur around the fibre/matrix interphase region strongly affect fatigue life and damage tolerance [37, 120]. In order to avoid the degradation of mechanical strength, it was attempted to embed the micro-scale MWNTs-glass fibre as an *in-situ* strain sensor for monitoring the damage process of composite utilizing the semiconductive interphase.

### 4.3.1 Piezoresistivity of single MWNTs-glass fibre

Firstly, it was investigated whether a semiconductive MWNTs-glass fibre is sufficient to show similar piezoresistivity for strain sensing as carbon fibres for a basic ability of smart structures. The simultaneous measurements of the single MWNTs-glass fibre resistance change, stress and strain,  $\epsilon$ , were conducted during tension up to fracture or cyclic tension. It was found that the fractional resistance increase ( $\Delta R/R_0$ ) of the fibre increases approximately linearly with tensile strain, which can be empirically described as:

$$\epsilon = \frac{1}{GF} \frac{\Delta R}{R_0} + \epsilon_0 \quad (4.6)$$

where  $R_0$  is the initial resistance of the specimen without applying stress,  $\Delta R/R_0$  is the relative resistance change, and the parameter  $\epsilon_0$  refers to the initial strain for piezoresistivity effect of CNT network.  $GF$  is the strain sensitivity factor (or known as gauge factor), i.e, the ratio of relative change in electrical resistance to the mechanical strain  $\epsilon$ . The  $GF$  determined by the regression analysis is 23.3 (Figure 4.9). It is well known

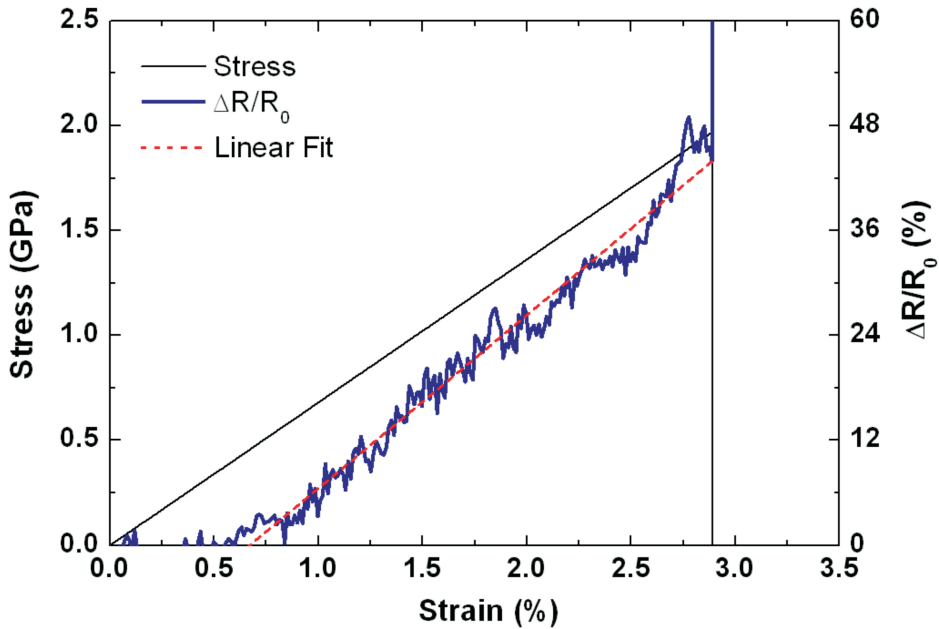


Figure 4.9: The fractional resistance increase  $\Delta R/R_0$  and linear regression based on Equation 4.6 of a single MWNTs-glass fibre during static tensile stress up to fracture



that the common technique for measuring strains on the surface of a structure is the use of commercially available metallic strain gauges. However, these conventional gauges can only measure strains at relatively large scale and at specific locations and directions, and they exhibit a relatively low and narrow range of sensitivity with usual gauge factors of 2.0 - 3.2 [121]. Thus, the  $GF$  value of the MWNTs-glass fibre is much higher than those of metallic strain gauges with geometrical piezoresistive effect. In general, the significant resistance change of nanotube network on the glass fibre surface can be attributed to not only the stress-dependent resistivity of the nanotube structure, but also the stress-dependent change of the nanotube network geometry, nanotube-nanotube interspace, contact area, and density (junction point per unit volume). This high sensitivity for micro-strain offers an opportunity for *in-situ* sensor.

#### 4.3.2 Single MWNTs-glass fibre as strain sensor in composites

Figure 4.10 characterizes the piezoresistive response of the composite with a single MWNT-glass fibre to the external loading, the electrical resistance monotonously increases with the applied strain, behaving like a variable resistor, but the fractional resistance increase ( $\Delta R/R_0$ ) curve with strain is identified basically into three stages: (i) liner, (ii) non-linear, and (iii) abrupt changes. At the first stage, the relative electrical resistance increases almost linearly proportional to strain up to approximately 1.5 %, caused by dimensional change of MWNT networks in the interphase. At higher strains, the slope of the resistance-strain curve increases exponentially proportional to strain, suggesting an irreversible resistance transition, associated with extensive concentration of stresses in the interphase, increase of nanotube-nanotube interspace and loss of junction points arising from irreversible change in network connection during loading. At the third stage, owing to the initiation and growth of microcracks in composite, the MWNT networks nearby are completely disconnected and the resistance jumps to “infinity” (out of measurable range) at a strain of 3.0 %. Finally, the microc-

racks continue to propagate leading to the fracture of composite at a strain of about 3.4 %. The micromechanisms of damage in composites have been extensively studied for

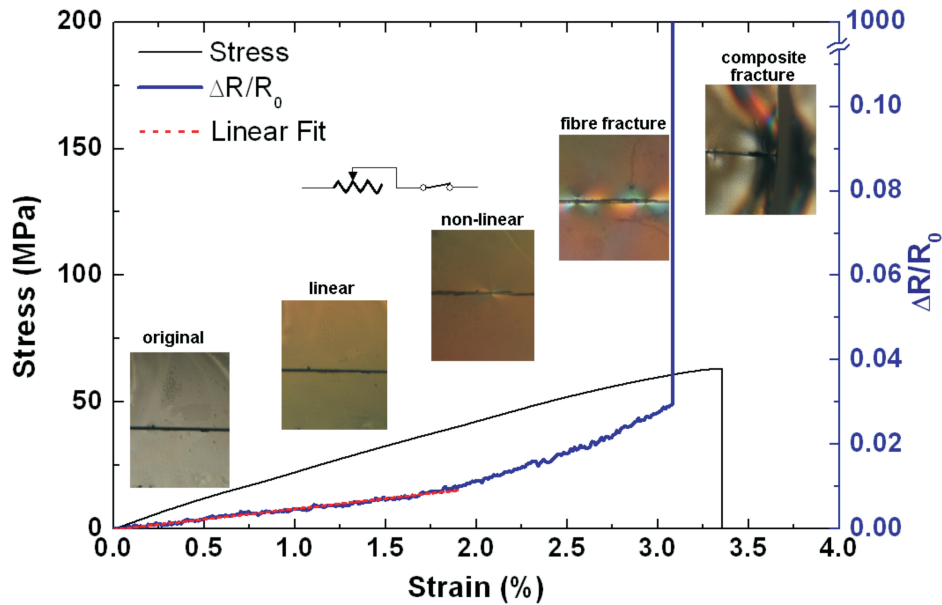


Figure 4.10: Simultaneous change of electrical resistance and tensile stress as a function of tensile strain for a single fibre/epoxy composite, the straight fitted line is the simulation of  $\Delta R/R_0$  at the linear increasing stage. Inserted images are the photoelastic profiles during tensile process corresponding to the  $\Delta R/R_0$  value at various stages

decades and the interphase has always been recognized as a key region in the failure process. Briefly, the microcracks in composites can propagate preferentially along the fibre-matrix interphases or transversely right through the fibre and matrix as shown in Figure 3.5. Thus the interphase is very sensitive to the internal damage in composites. For these cases if using conductive fibres such as carbon fibre as sensor, it may not provide information of microcracks earlier than fibre fracture. By dispersing CNTs into polymer matrix as another way to detect early development of a small number of cracks in the fibre/polymer matrix interphase, the resistance change of the whole CNT network should be very limited. Additionally, in the case of MWNTs-glass fibre, the electric current only passes through the interphase region and both the fibre and the surrounding matrix remain their own properties, such as electrically insulating, thereby the electric conduction mechanism is different from traditional CNT composites fabri-

cated by dispersing CNTs into polymers or inserting an electric wire/carbon fibre. As a consequence, the unique ability for detecting microcracks in an interphase using a MWNTs-glass fibre sensor is highlighted, whichever fibre or matrix breaks first.

To get a more timely predictive signal, three individual fibres were embedded into the matrix and the variation of resistance was monitored (Figure 4.11). The resistance increases sharply and step-wise with the three fibres broken one by one, which acted as three variable resistors connected parallelly. Hypothetically, the initial resistant values of these three fibres are equal, when the first fibre broke, the relative resistance ( $\Delta R$ ) would be 50 % of the original resistance ( $R_0$ ); subsequently, the relative resistance would reach to 200 %, when the second fibre broke, the experimental result is almost coincident with this calculation. Obviously, the multi-individual fibre composite improves the early warning capability and sensitivity with regards to the “material’s health”. Since their small size, the MWNT-glass fibres are minimally invasive to and

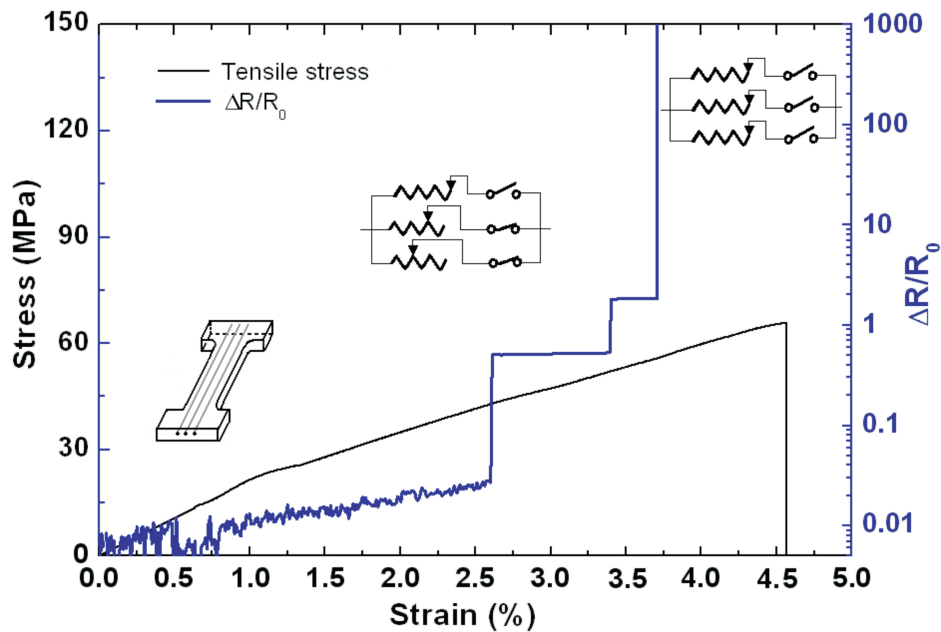


Figure 4.11: The function of early warning is optimized through three individual fibres in the composite

can be seamlessly used in material structures. Here, we demonstrate a potential application for detecting the propagation of microcracks in the glass facade. Modern

glass facades inform the architecture of major cities throughout the world, but there have been cases of collapsing facades endangering passers-by [122, 123]. The glass fibre sensor could be integrated into laminated glass such as the recently developed piezoelectric sensor [124] that detects micro fissures-earlier than the whole glass actually breaks. As illustrated in Figure 4.12, even without the glass fibre breakage, the resistance data demonstrates high-sensitivity observation of microcrack propagation through the glass slide. This fibre reinforcement together with sensor function can be applicable to other nonconductive fibres (i.e., jute fibre [125]) utilized as embedded sensors or surface-mount strain gauges for critical components required maintenance and inspection in wind turbine, aircraft and automobile manufacturing, paint, touch panel, antistatic and self-diagnosis applications.

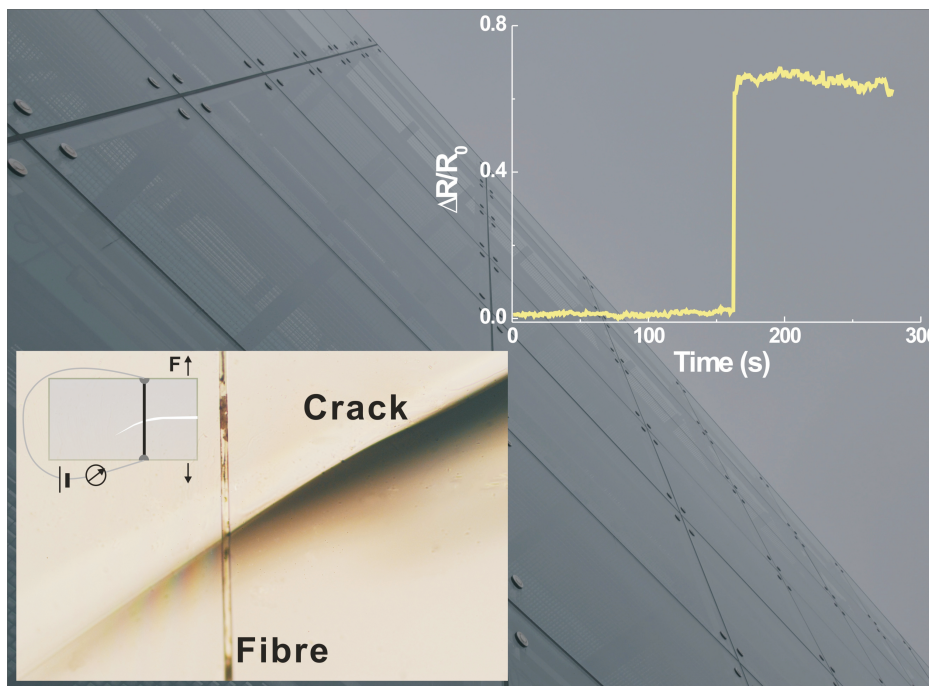


Figure 4.12: The resistance of the single fibre sensor varied significantly when the microcrack in the substrate glass slide passed through the vicinity of fibre which affected the fibre/epoxy interphase structure without the fibre breakage

To further investigate the response of *in-situ* sensor to the interphase damage process, it was monitored that the resistance variation of the single fibre composite under

cyclic loading with progressively increasing the strain peaks (Figure 4.13). The relatively large difference in deformation among each cycle highlights the accumulation of damage, which gives insight into the mechanism of resistance change. Clearly, when the peak of strain in the first and second cycles is less than 1.5 % (in the range of linear stage, as aforementioned and shown in Figure 4.10), the variation of resistance closely follows the strain which returns to the original point after unloading. However, the strain exceeds the value of linear stage during the third cycle, the value of resistance start to deviate the curve of strain, suggesting the occurrence of permanent structural deformation/damage of CNT networks caused by microcracks of interphase. With further increase of the strain peak, the enlarged microcracks eventually break the last conductive pathway of the nanotube bridges, the resistance jumped to “infinity”. After that, the microcracks would keep on growth under loading condition, resulting in the eventual fracture of composite specimen. The results show that the single glass fibre as an *in-situ* sensor with the ability of real-time tracking damage accumulation and early warning material failure under a cyclic loading condition.

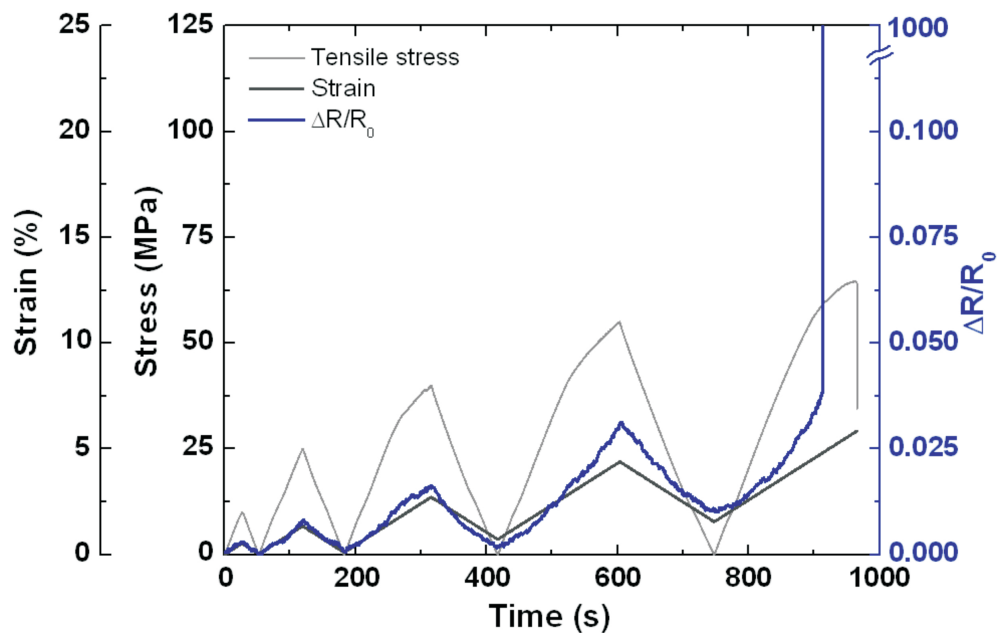


Figure 4.13: The sensor response to cyclic tensile loading. The variation of electrical resistance with progressive increase of peak values of tensile strain/stress in a single fibre model composite

In summary, the single fibre coated by MWNTs has shown the high sensitivity to strain and an opportunity for *in-situ* strain sensor. The embedded single MWNTs-glass fibre into epoxy matrix is able to monitor the damage process in composite. The formation of MWNT-concentrated interphases in the composite is a promising way to realize continuous self-monitoring for internal microcrack and structural integrity, and the *in-situ* strain sensor can report the fracture of material in advance. Next, a more timely sensor was achieved through embedding multi-individual fibres into a matrix. Furthermore, an application of the *in-situ* sensor in glass facades is proposed, which can detect micro fissures earlier than the whole glass actually breaks.

## 4.4 Electromechanical switch

### 4.4.1 Switch actuated by strain

As above mentioned, microcrack is always considered as a negative aspect for mechanical property of composites. Early detection and eventually even the utilization of microcracks remain two of the most challenging tasks in materials science. In this research, besides an *in-situ* strain sensor, MWNTs-glass fibre was manufactured to be an electromechanical switch utilizing the microcrack. As schematically shown in Figure 4.14, a rational use of the microcrack associated with fibre breakage was made as a trench structure, which is bridged with carbon nanotubes concentrated in the fibre/matrix interphase. Owing to MWNT network bridges across microcrack connecting/breaking corresponding to unloading/loading of external forces, the electric circuit presented the states: ON/OFF, which actually fabricated an electromechanical micro switch.

It is examined whether the disconnected MWNT networks bridging across microcracks could be connected repeatedly under cyclic loading conditions. An alternative function the electromechanical “switch” was found, where the electrical signal turns ON and OFF states with a variation of strain (see Figure 4.15(a)). During the first cycle loading, the local microcrack is enlarged (see Figure 4.15(b)) to completely break any junctions of carbon nanotube networks, where a natural trench structure is formed and the switch presents the “OFF” state. During the unloading, subsequently, the microcracks are closing and the disconnected nanotubes are approaching each other. Whenever the microcrack is less than the critical gap (microcrack width), some of disconnected carbon nanotubes reconnect to rebuild ohmic contacts or approach very near to each other to form tunnelling current, the switch turns into “ON” state. The conversion of ON-OFF states occur at almost same strains of all cycles, except the first cycle associated with the structure formation of the switch.

In Figure 4.16, SEM images indicate that the carbon nanotubes bridge the trench at

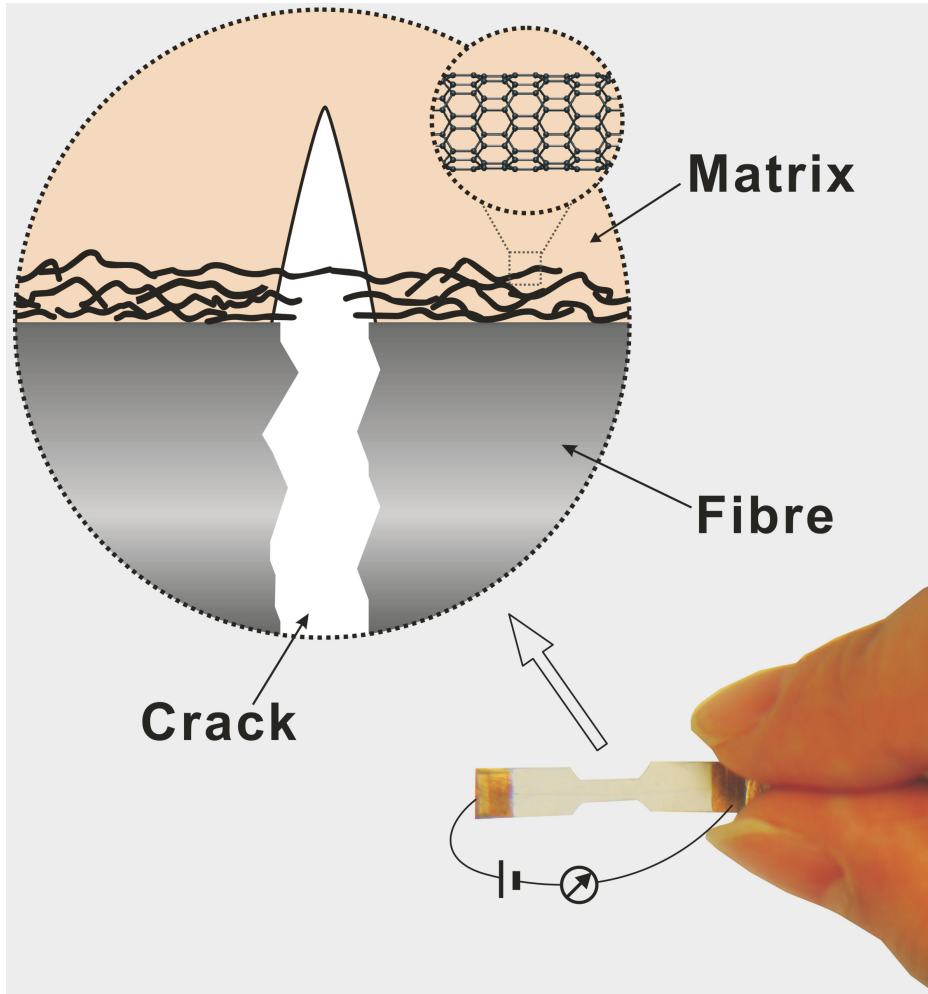


Figure 4.14: Schematic of a microcrack bridged by MWNTs in a single fibre/epoxy composite

less than the critical gap. With the microcracks expanding at a higher strain, the junctions of the carbon nanotubes around the microcrack can be totally detached. Correspondingly, in contrast to the generally designed gap in the electromechanical devices through complicated micro-fabrication processes [126], the MWNTs bridging microcracks result in a micro switch with the “junction-break” (connection-disconnection of CNTs network) mechanism, which integrates the electrode and contact gap structure in one single fibre model composite.

In order to accurately control the switch, we attempted to evaluate quantitatively the critical gap,  $\delta_c$ , at the critical strain according to the axial fibre stress distribution in the



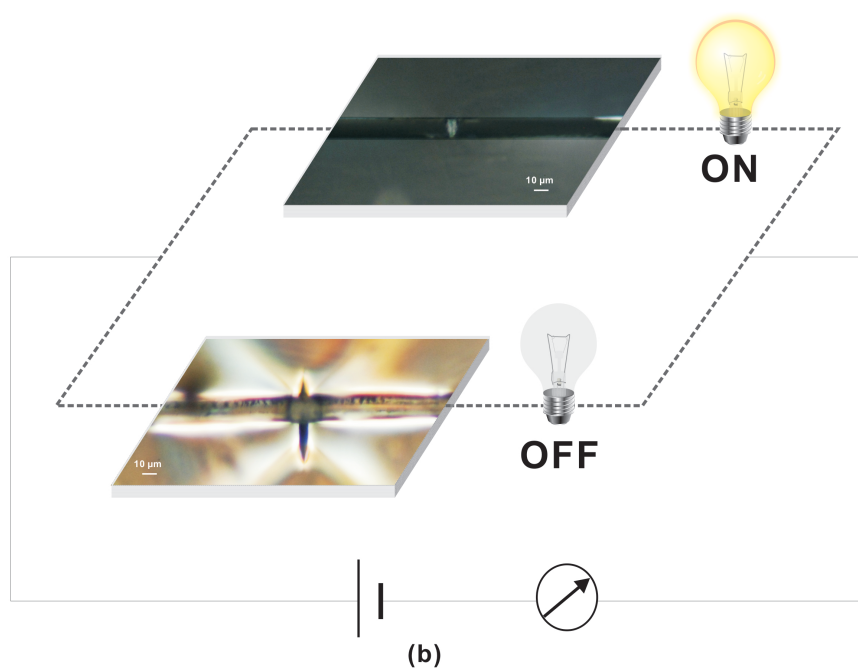
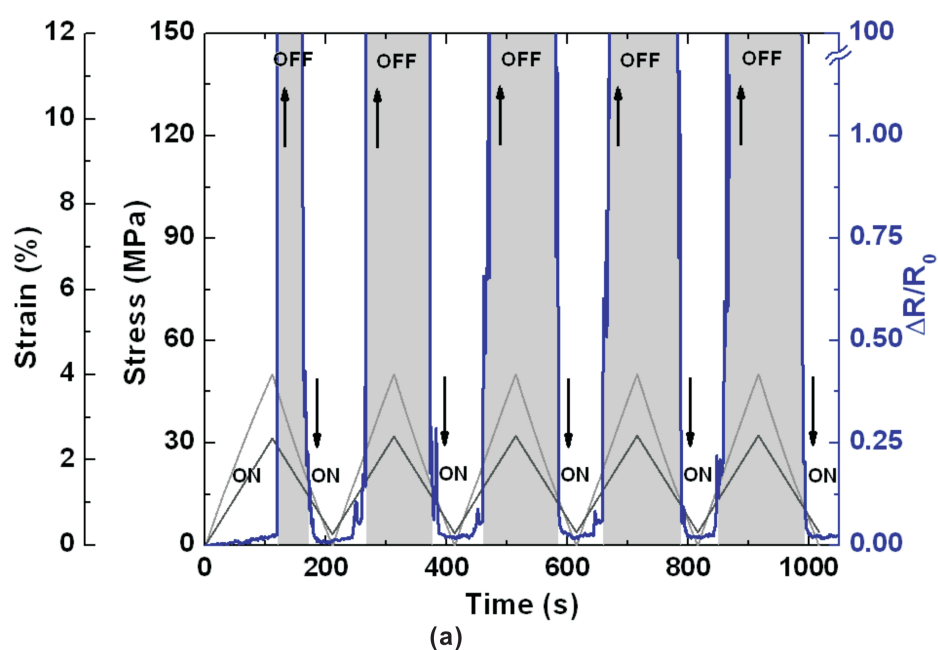


Figure 4.15: (a) The electromechanical switch acts during cyclic tensile. The resistance in ON state is around 48 MΩ, while the resistance in the OFF state is about 10 GΩ. The black and grey lines are the strain and stress curve, respectively. (b) The circuit schematic of the switch, the switch turns ON or OFF state with the closing or opening of microcrack

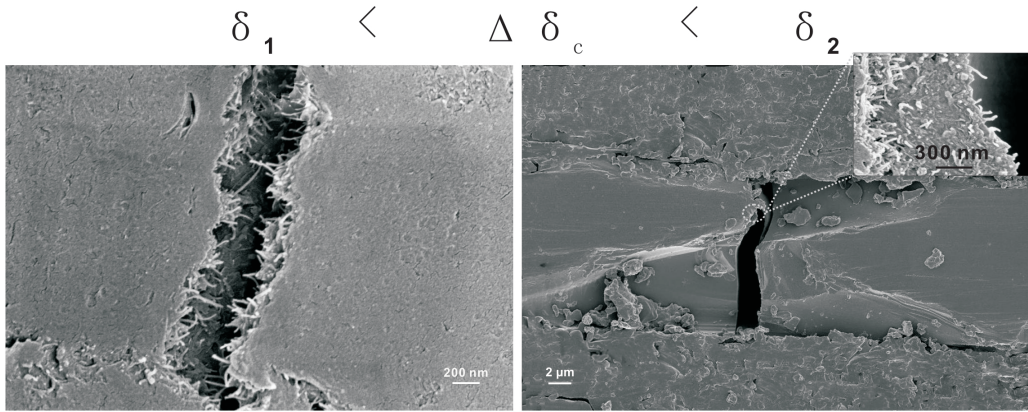


Figure 4.16: SEM images display the CNT network bridging or disconnecting based on the size of microcrack, which is smaller or larger than the critical gap  $\delta_c$

single fibre composite (illustrated in Figure 4.17):

$$\Delta\delta_c = \delta_t - (\delta_e + \delta_i) \quad (4.7)$$

where  $\delta_t$  is the experimentally detected total displacement of composite for the gauge length,  $\delta_e$  and  $\delta_i$  are the displacements of effective and ineffective regions, respectively. After the fibre breaks, it does not carry load at the break point. The stress anal-

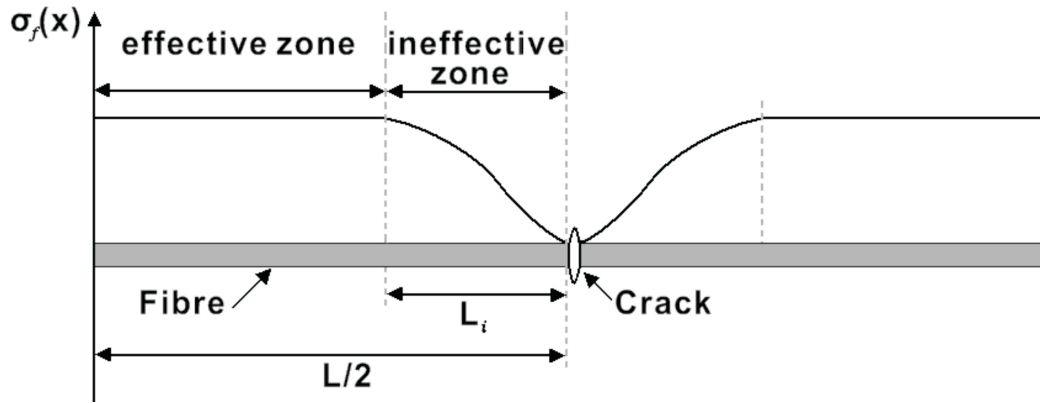


Figure 4.17: Schematic of the fibre stress distribution in a single fibre model composite after a fibre break for the case of no debonding

ysis developed by Whitney and Drzal [127] provides the following expression for the

ineffective length  $L_i$ :

$$L_i = 2.375 \frac{d_f}{2} \sqrt{\frac{E_{1f}}{G_m} - 4\nu_{1f}} \quad (4.8)$$

where  $d_f$  is the diameter of fibre,  $E_f$ ,  $\nu_{1f}$  are the axial modulus and Poisson's ratio of the cylindrically orthotropic fibre,  $G_m$  is the shear modulus of matrix. In the effective region, the fibre tensile stress  $\sigma_f$  is constant, therefore,

$$\delta_e = \frac{\sigma_e}{E_{1f}} (L - 2L_i) \quad (4.9)$$

where  $L$  is the total length of the embedded fibre. The displacement of the ineffective region is given by:

$$\delta_i = 2 \int_0^{L_i} \epsilon_i(x) dx \quad (4.10)$$

The strain variation is here based on the continuous phase (fibre),

$$\epsilon_i = \frac{\sigma_i(x)}{E_{1f}} \quad (4.11)$$

where the fibre stress in the ineffective region is obtained according to an axisymmetric model developed by Whitney and Drzal [127, 128],

$$\sigma_f(x) = [1 - (4.75 \frac{x}{L_i} + 1)e^{(-4.75 \frac{x}{L_i})}] A_1 \epsilon_0 \quad (4.12)$$

where  $x$  is the distance from the fibre break point along the fibre axis ( $0 < x < L_i$ ), the far field strain,  $\epsilon_0$ , of the specimen is the strain of composite, and  $A_1$  is a material property constant defined as:

$$A_1 = E_{1f} + \frac{4K_f G_m \nu_{1f}}{K_f + G_m} (\nu_{1f} - \nu_m) \quad (4.13)$$

where  $K_f$  is the plane strain bulk modulus of the fibre,

$$K_f = \frac{E_{2f}}{2(2 - E_{2f}/G_{2f} - 2\nu_{2f}E_{2f}/E_{1f})} \quad (4.14)$$

$E_{2f}$  and  $\nu_{2f}$  are the transverse moduli and Poisson's ratios of the cylindrically orthotropic fibre,  $G_{2f}$  is the transverse shear modulus of the fibre. The displacement of the ineffective region is obtained from above Equations. Taking the stress analysis for an estimate, the critical gap for crack bridging,  $\delta_c$ , could be figured out, for the specimen in Figure 4.15(a), the calculated critical gap is about  $2.7 \mu\text{m}$  [6]. It is worthwhile to note that the effective service life of the switch should be influenced by multiple factors, such as, magnitude of loading force, speed, temperature and so on. Under the peak stress of 50 MPa, the observed service life of our switch could reach up to 50 times indicating a reasonable good repeatability [6].

#### 4.4.2 Switch actuated by thermal source

It was subsequently further confirmed the “junction-break” mechanism by a thermal actuated switch, since the microcrack shrinking to the critical gap through thermal expansion might also achieve the conversion of ON-OFF states. In order to quantify this idea, the switch was fixed onto a clamp and stretched to OFF state, then heated, the normalized resistance change ( $R/R_0$ ) is shown in Figure 4.18(a). With the increase of temperature, the composite starts to expand and the microcrack on interphase shrinks where the disconnected carbon nanotubes would approach each other. Once the disconnected carbon nanotubes rebridged, the electric circuit is immediately conducted and the resistance drops down sharply, at which the temperature is defined as the switch temperature. Notably, the variation of the resistance during cooling is opposite to that during heating. Thus, the switch could be reproducibly actuated through heating and cooling. It should be mentioned that the temperature dependence of the electrical resistance of the intrinsic properties of our MWNTs shows a typically semiconducting behavior with a negative temperature coefficient (NTC) [80]. The variation of resistance is less than 10 % in 60 °C temperature change (see also Figure 4.19) [129, 130], which thereby ignores the influence on the actuating switch. Another concern is that polymer chains usually relax and tend to move with increased temperature, and there-

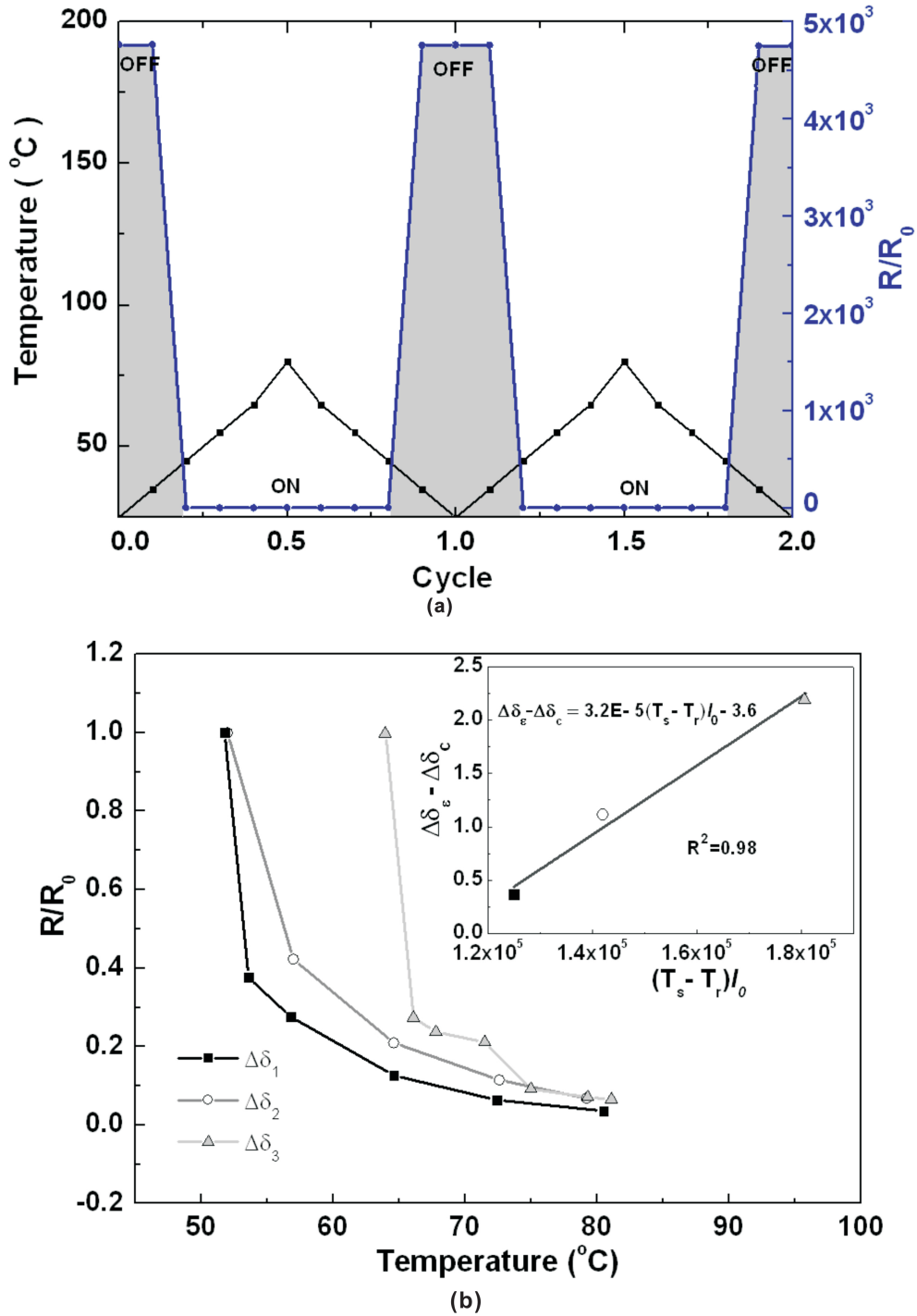


Figure 4.18: The behavior of electromechanical switch actuated by temperature. (a) The relative variation of the resistance and temperature dependence on cycle time ( $R_0$  is 210  $\Omega$ ). (b) The relative variations of the resistance during heating show different switch temperatures, since difference initial gaps ( $\Delta\delta_1$ ,  $\Delta\delta_2$ ,  $\Delta\delta_3$  are 2.2, 3.0, 4.0  $\mu\text{m}$ , respectively) induced by tensile strains. The inserted figure is the straight fitted line of shrinking distances from the initial gap to the critical gap ( $\Delta\delta_c$ , is 1.8  $\mu\text{m}$ ) based on Equation 4.15

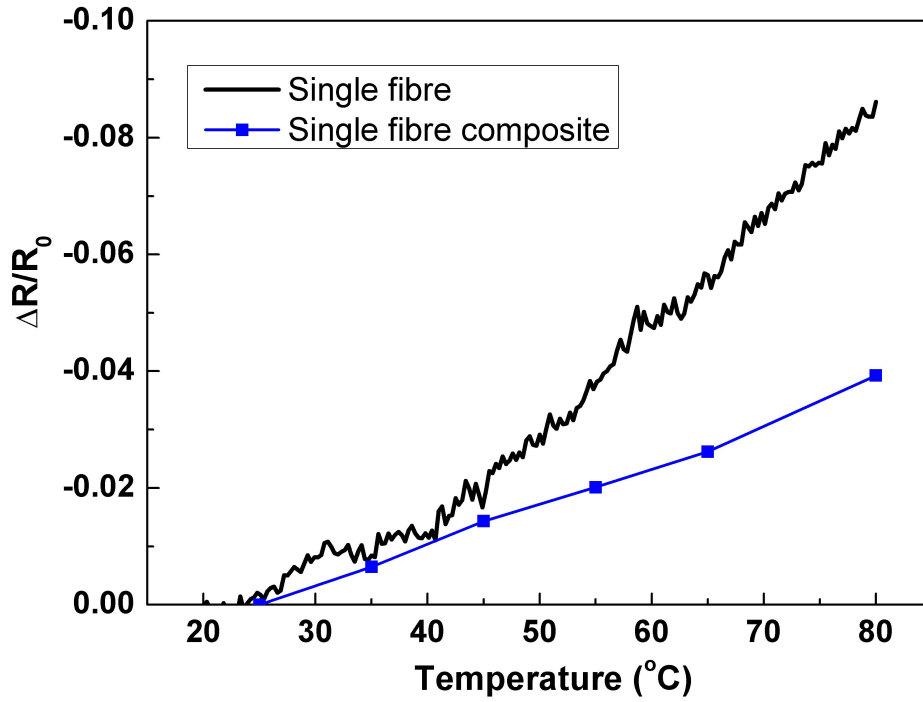


Figure 4.19: Dependence of the electrical resistance on temperature of the single MWNTs-glass fibre and single MWNTs-glass fibre composite indicates the negative temperature coefficient of MWNTs

fore the propagation of a crack is possible but not remarkable due to the restriction effects from the CNT/glass fibre, and the slow relaxation of crosslinked epoxy molecules at a temperature below  $T_g$  [131]. Thus, the bulk plastic experiences expansion mainly by closing of the microcrack as mentioned above. The following equation is proposed for the shrinking distance of the microcrack from the initial gap to the critical gap:

$$\Delta\delta_\epsilon - \Delta\delta_c = \alpha_T \cdot (T_s - T_r) \cdot l_0 \quad (4.15)$$

where  $\Delta\delta_\epsilon$  is the width of initial gap under strain  $\epsilon$ ,  $\alpha_T$  is the coefficient of thermal expansion in interphase region,  $l_0$  is the total length of fibre before heating,  $T_s$ ,  $T_r$  are switch temperature and room temperature, respectively. Correspondingly, the switch temperature could be controlled by adjusting the initial gap size. Figure 4.18(b) shows that the resistance of the switch changes with temperature under various initial gaps.

Clearly,  $T_s$  shifts to the higher temperature with larger  $\Delta\delta_e$ , which is consistent with the trends based on Equation 4.15. The inset shows the equilibrium shrinking distances as functions of  $(T_s - T_r) \cdot l_0$  and the fitted curve is in good agreement with the predicted linear relationship of Equation 4.15. The coefficient of thermal expansion in the interphase can be obtained through the slope of the fitted curve, which is  $32 \times 10^{-6} \text{ }^\circ\text{C}^{-1}$  and marginally less than the value of the matrix ( $48 \times 10^{-6} \text{ }^\circ\text{C}^{-1}$ ), possibly caused by the constricting effect from the glass fibre and CNTs [132, 133]. Owing to the sensitivity for micro-strain and temperature, this electromechanical switch demonstrates an unique opportunity to be used as a micro-control/monitor device. While little is known about the response time so far, which should be dependent on factors such as speed of microcrack propagation, creep of the composite, and the quality of the CNT coating. Thus, it is still necessary to explore whether the “re-bridged CNT network” mechanism can be *in-situ* observed through nanotomography with possible future development of resolutions down to a few nanometers.

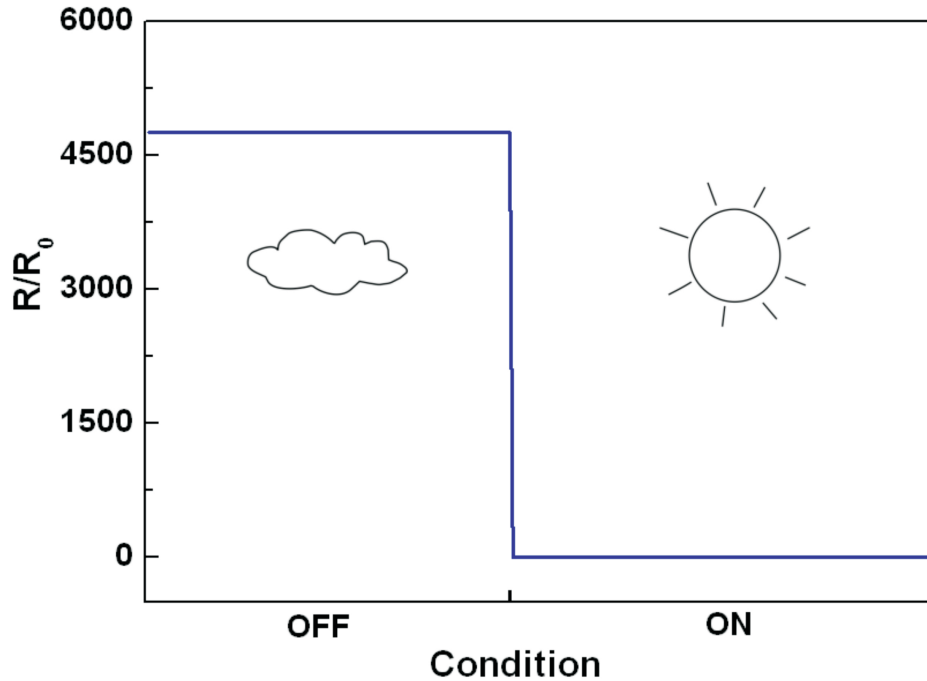


Figure 4.20: The switch presents ON or OFF state with turning on or off the visible light illumination (a lamp of 60 W)

Further work along these lines will be needed to explore whether the switch is possibly actuated by other kind of sources, such as laser, ultraviolet (UV), visible and infrared (IR) light and so on. It is confirmed by the preliminary results of the small thermomechanical deformation caused by visible light illumination driving the switch (Figure 4.20).

Overall, this micro switch represents an innovative concept for further development of miniaturized device, which use the microcrack bridged by CNTs as a trench structure in composite. Owing to good repeatability and low actuated power, it is also beneficial to achieve the environmentally friendly and low-cost goals for realization of a wide range of micro control applications in conventional materials.



## 4.5 Single MWNTs-glass fibre in polymer as chemical and physical sensor

High performance thermosetting resins such as epoxy/amine resin systems are used extensively as matrices for advanced fibre reinforced composites. The rate and degree of curing are important parameters as they have a significant influence on the matrix dominated properties of the fibre reinforced composites. The magnitude and temperature dependence of the electrical resistivity (or conductivity) of a polymer is a function of the molecular structure of the polymer, the nature and number of the charged carriers, and the temperature. Therefore, the measurement of electrical resistance has been considered as a direct method to on-line monitor the polymerization in thermoset and the crystallization in thermoplastic [134, 135]. However, most of the polymers are insulative materials and the resistance measurement needed to employ high electrical field or alternating current, which leads to difficulties and doubtful factors for the experimental and analysis procedures. Some researchers dispersed the conductive powders into polymer matrix to improve conductivity in order to follow polymerization [136, 137], but this method destroyed the original insulating property of polymers.

In above sections, single glass fibres coated by carbon nanotubes could be used as a multifunctional micro-scale sensor or switch in composites. Besides the microstrain and microcracks, the carbon nanotube network distributed in the interphase has shown the high sensitivity to humidity and temperature [6, 66, 71]. Due to the distortion of the electron clouds of CNTs from a uniform distribution in graphite to asymmetric distribution around cylindrical nanotubes, a rich  $\pi$ -electron conjugation forms outside of the CNTs, making them electrochemically active [138, 139], suggesting the electrical properties of CNTs are extremely sensitive to charge transfer and chemical doping effects by various molecules.

Here, a carbon nanotube network distributed in the interphase between glass fibre and matrix was utilized as a *in-situ* chemical/physical sensor which monitors the cur-

ing or crystallization process of polymers. Because of the high sensitivity of CNTs network, the resistance could characterize the change of viscosity and different stages of reaction in a polymer system. For various hardener ratios and crystallization temperatures, the plots of resistance showed distinctive features. Especially, the electrical properties of nanotube networks are highly sensitive to the motion of molecular chains for the cured or crystallized polymers.

### 4.5.1 Monitoring the polymerization of thermoset polymer

#### 4.5.1.1 Isothermal curing

The epoxy resin is a commercial product based on diglycidyl ether of bisphenol-A (DGEBA, resin EPR L20, Hexion Specialty Chemicals Stuttgart GmbH, Germany) with an epoxy equivalent of 179 g/equiv., cured by a diamine agent, 2,2'-dimethyl-4,4'-methylene bis(cyclohexylamine) (EPH 960) with an amine equivalent weight of 60 g/equiv. Three mixtures with different weight ratios of epoxy to hardener were prepared: a stoichiometric system 100:34, hardener-rich system 100:45, epoxy-rich system 100:25. Single MWNTs-glass fibre was mounted on a glass slide with silver paste, which was put on a hot-stage (Linkam LTS350 Heating/Freezing, UK) in a nitrogen atmosphere. Epoxy mixture was dropped onto the fibre surface, and then hot-stage was sealed. Two conductive wires fixed on glass slide with MWNTs-glass fibre were connected with the Keithley 2000 multimeter with constant test current ( $10\ \mu\text{A}$  /  $700\ \text{nA}$ ).

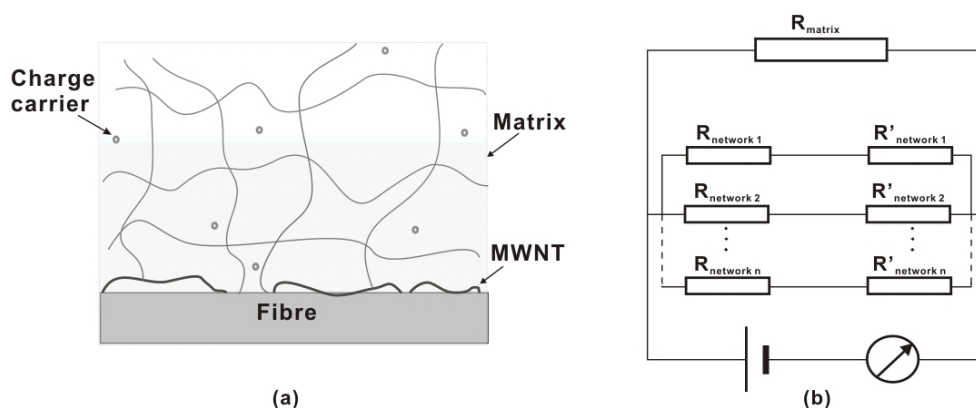


Figure 4.21: The schematic diagram of chemical sensor. (a) The electrical conductive mechanism of monitored polymer; (b) the equivalent circuit of measured system

Figure 4.21 is the schematic diagram for conductive mechanism of measured system. Electrical conduction of polymer is believed to be an ionic mechanism [130], the main source of ions consists of impurities which are not part of the structure of the polymer. The concentration of impurities was expected to remain fairly constant dur-

ing the curing [140]. Some functional groups in molecular chains could be the other part of charge carriers, the concentration of which are expected to decrease during the curing. Since the mean free path of ions becomes comparable with the molecular separations, conduction can be pictured as a “hopping” process, where each ion hops between neighbouring molecular sites by thermal activation over a potential energy barrier. Equation 4.16 is used to express the relationship between the resistance of polymer and the activation energy  $E_c$  for the conduction process [141]:

$$R_{matrix} = A_0 \exp\left(\frac{E_c}{RT}\right) \quad (4.16)$$

where  $A_0$  is a temperature independent constant,  $R$  is the molar gas constant. The potential barrier against the hopping process between molecular sites, will increase as the amount of freedom in the structure is decreased by cross-linking. Therefore, the conductivity decreases during polymerization owing to the gradual immobilization of the system. While the process of the polymerization or the rapid crystallization is completed,  $R_{matrix}$  would become too huge to observe some small changes of composites, such as the glass transition.

According to the  $R$ - $T$  curve of single MWNT-glass fibre, see Figure 4.22, the resistance of single MWNTs-glass fibre,  $R_{CNT-fibre}$ , approximately linearly decreases with an increment in temperature, hence,

$$R_{CNT-fibre} = -k_1 T + B \quad (4.17)$$

where,  $k_1$  and  $B$  are constant values dependent on the quality of network.  $T$  is the absolute temperature. However, in the liquid polymer, the conductivity of CNT network on glass fibre is influenced by the ions, the tube-molecule interaction with organic molecules that act as electron donors or acceptors [142, 143].

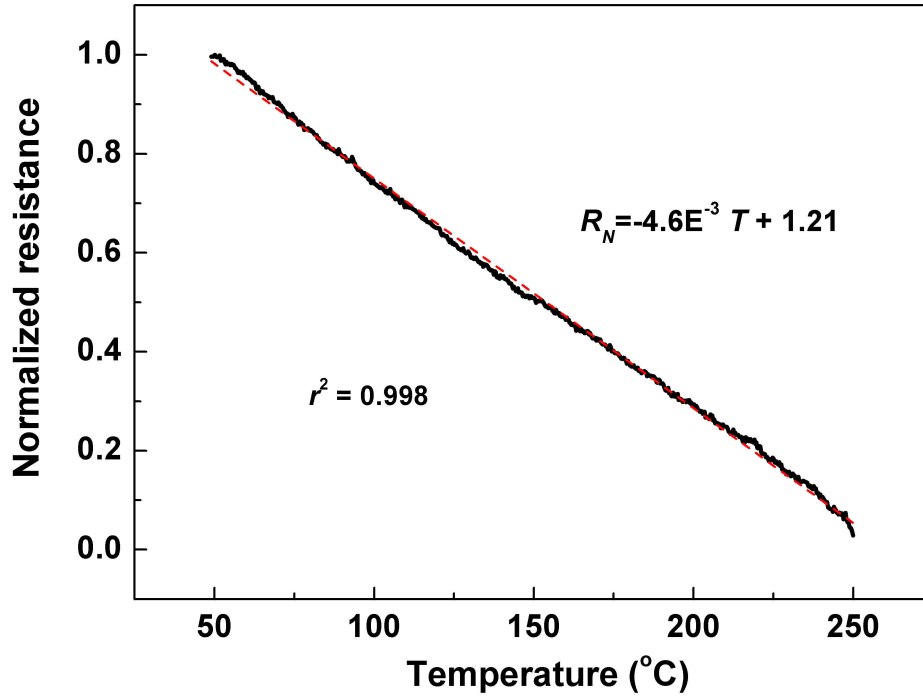


Figure 4.22: The change of electrical resistance of single MWNTs-glass fibre with increasing temperature. The red dash line is a fitted line;  $r^2$  is the variance

$$\frac{1}{R_{interphase}} = \sum_{i=1}^n \left( \frac{1}{R_{networki} + R'_{networki}} \right) \quad (4.18)$$

$R_{matrix}$  is the resistance of matrix.  $R'_{matrix}$  is the resistance of matrix inside the interphase;  $R_{network}$  is the resistance of a part of CNTs networks without the structure influence caused by curing, where we assume the thickness of insulating layer in the contact area of crossing CNTs to be uniform and neglect the variation of barrier height along the thickness [130]. In contrast,  $R'_{network}$  is the resistance of the other part of CNTs networks destroyed by thicker polymer layers.

$$R_{total} = \begin{cases} \frac{1}{1/R_{matrix} + 1/R_{interphase}} & \text{before polymerization or crystallization} \\ R_{interphase} & \text{after polymerization or crystallization} \end{cases} \quad (4.19)$$

where  $R_{interphase}$  is the total resistance in interphase region.  $R_{total}$  is the total resis-

tance of measured system which directly characterize the internal information of composites even though  $R_{matrix}$  is hardly measured.

Figure 4.23 is the resistance-time curve for isothermal curing process of epoxy, the temperature was raised to 80 °C in 10 min and held for 8 hours, and the resistance was normalized for convenient analysis,  $R_N = (R_t - R_{max}) / (R_{max} - R_{min})$ , where  $R_N$  is the normalized resistance;  $R_t$  is the resistance at  $t$  min;  $R_{max}$ ,  $R_{min}$  are the maximum and minimum resistances, respectively. During the polymerization, the transfer of migrating charges corresponds to the viscosity and crosslink density of epoxy mixture, the change of resistance could be divided into three stages. Initially, the resistance decrease with an increase in temperature (see the inserted figure in Figure 4.23). At this stage, the curing reaction of resin is negligible, whereas rising temperature results in significant drop of viscosity and increase in the mean kinetic energy of the charge carriers that facilitate conduction, thus the minimum resistance value corresponds to the minimum viscosity point of curing process, which can be treated as the on-set point of accelerated curing reaction.

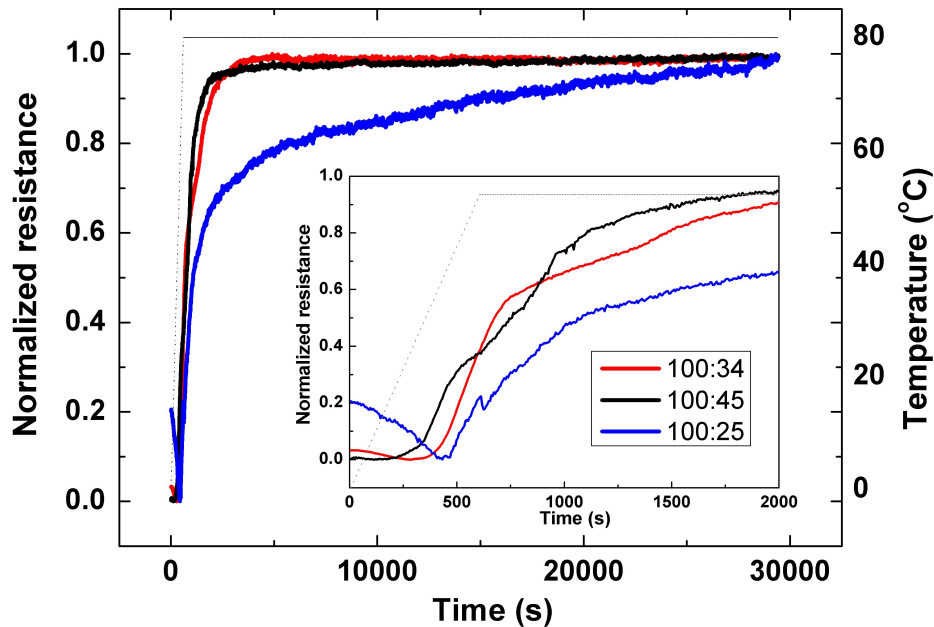


Figure 4.23: The resistance change with time during isothermal polymerization. Inserted figure is the magnified initial part of resistance-time plot

Subsequently, the resistance starts to linearly increase with curing time which is caused by reduced mobility of charge carriers and the amount of functional groups helping conduction. This stage characterizes that the rate of reaction accelerates between reactive monomers and the viscosity ascends. The on-set points of accelerated curing reaction for these three systems shift to early time with increase of the hardener amount (the hardener-rich first occur, followed by stoichiometric and epoxy-rich systems). With consumption of epoxy and amine functional groups, an infinite network of crosslinked polymer molecules is gradually formed, which inhibit the mobility of charge carriers through the matrix and the concentration of functional groups doping CNTs network is reduced. It is another reason that the matrix in interphase blocks the tunneling current between CNTs. Therefore, the slope of resistance-time curve decrease and the exponential increase in resistance are an indicative signal of gelation.

The most obvious discrepancy among three systems occurred at the third stage, where the resistances in both of the stoichiometric system and hardener-rich system almost approach an asymptotic level, however, the resistance of epoxy-rich system keeps increasing though the rate is lower, which is likely caused by vitrification process. A time-temperature-transformation (*TTT*) cure diagram (Figure 4.24) is a plot showing the times required to reach gelation and vitrification, respectively, during isothermal cure as a function of cure temperature. During polymerization, glass transition temperature,  $T_g$ , keeps increasing due to continuous increasing of the crosslink density as well as the number-average molecular weight (of the sol/gel mixture) and the decrease in chain ends.  $T_{g\infty}$  is the the glass transition temperature of the fully cured resin. In the case of that the temperature of isothermal cure,  $T_c$ , below  $T_{g\infty}$ , vitrification occurs, which involves a physical transformation from a liquid or rubbery state to a glassy state as a result of an increase in the crosslinking density of the material. [145, 146] The segmental mobility is substantially decreased in the vicinity of the glass transition, and the overall rate of the reaction may become progressively controlled after vitrification by the limiting diffusion of reacting specimens, therefore, the reaction rate

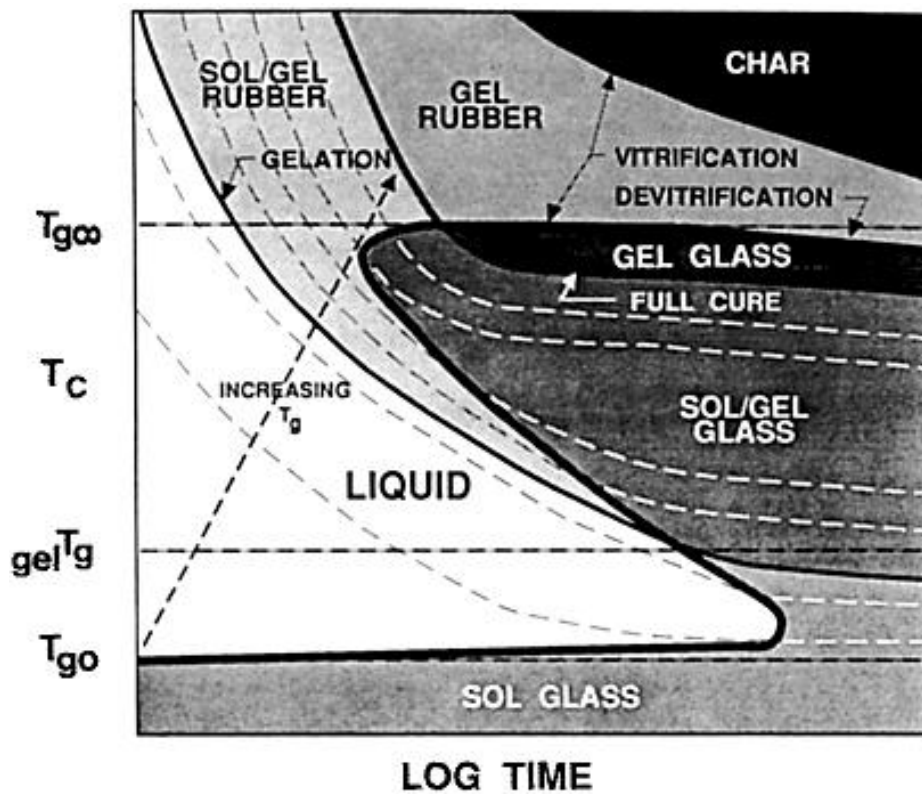


Figure 4.24: The generalized time-temperature-transformation ( $TTT$ ) isothermal cure diagram [144]

becomes very low. In this investigation, based on dynamic cure results, both of  $T_{g\infty}$  of the stoichiometric system and hardener-rich system are above  $80\text{ }^{\circ}\text{C}$ , therefore, the rates of the chemical reaction and the resistance change become very low at the third stage. However, the resin will not vitrify on isothermal cure if the cure temperature  $T_c$  is above  $T_{g\infty}$ , in this case, the chemical kinetics governs the progress of the reaction. The cure can then proceed to completion since it will not be quenched prematurely as it would be below  $T_{g\infty}$ , although 100 % conversion is rarely achieved because some reactive sites may be isolated in the network [145]. For the epoxy-rich system in this investigation,  $T_{g\infty}$  (about  $70\text{ }^{\circ}\text{C}$ ) is below the temperature of isothermal cure ( $80\text{ }^{\circ}\text{C}$ ) (based on dynamic cure results), so a continuous increase in resistance of epoxy-rich system is found out at the third stage. Additionally, hardener-rich system earlier occur speed-down than stoichiometric system, and the resistance of hardener-rich system



slightly rise relative to the stable stoichiometric system during vitrification, which is associated with higher hardener amount.

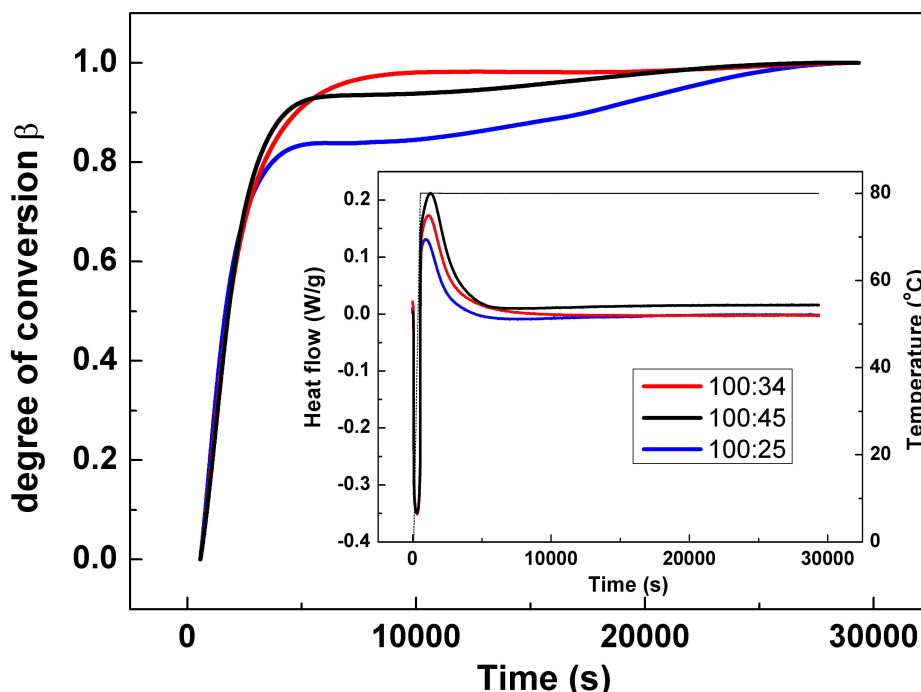


Figure 4.25: The relative degree of conversion for polymerization during isothermal DSC measurement. Inserted figure is the heat flow for the whole heating process

Figure 4.25 shows the relative degree conversions of three systems from DSC results, the inserted figure is the heat flow during isothermal curing which is hard to observe the reaction during rapidly heating. When the “plateau” region was magnified, a small exothermal peak was found in epoxy-rich and hardener-rich systems, respectively, which are consistence with the resistance slightly rising during this region. So, two baselines per system were used to calculate the relative degree of conversion, in which the measured onset time is later than that of the real reaction due to a lack of initial exothermal. The tendency and shape of degree of conversion curve is basically similar with the resistance curve, but, the transition time is different, which is caused by different heat device, measurement mechanism and the influence of physical process to DSC test. Consequently, the on-line curing process can be evaluated by embedding single MWNTs-glass fibre, and more detailed information about various stages of re-

action can be observed without complex calculation, at the same time, the  $R_N$  could be used as relative curing index.

#### 4.5.1.2 Dynamic cure

Dynamic runs of normalized resistance and DSC are shown in Figure 4.26, during

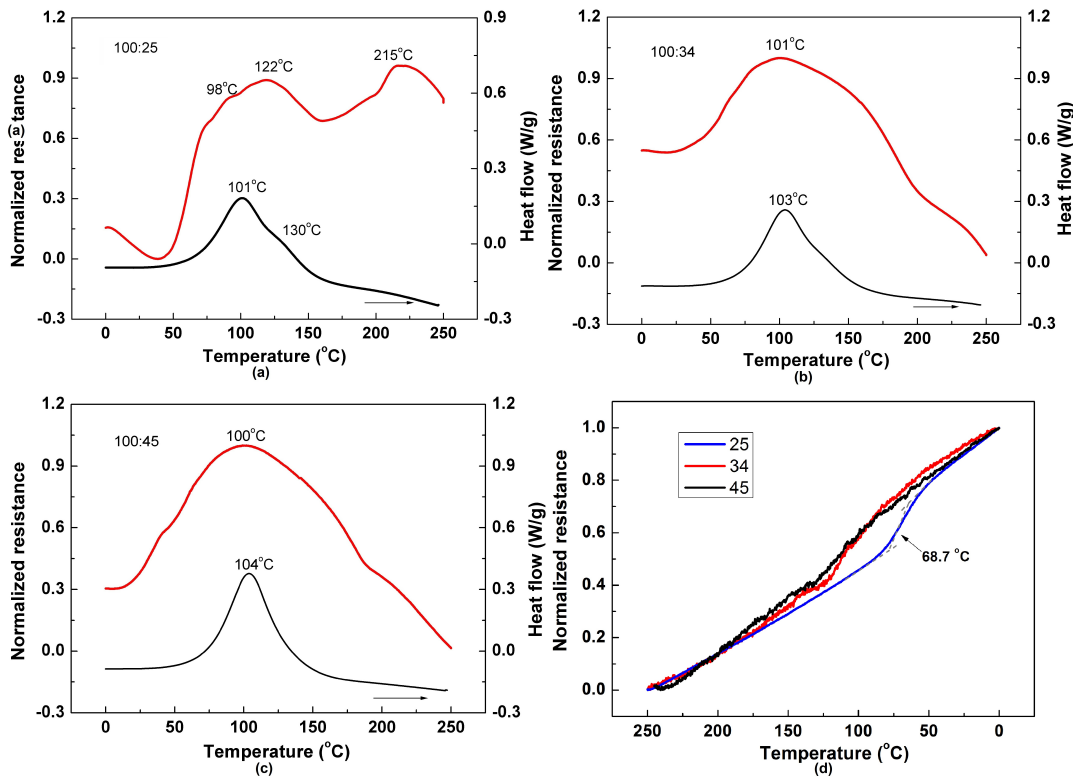


Figure 4.26: The changes of resistance and heat flow for various systems during dynamic polymerization: (a) 100:25; (b) 100:34; (c) 100:45; (d) the observation of glass transition during cooling process after the first dynamic cure, the gray dash lines are auxiliary lines used to evaluate the glass transition temperature

which the sample was heated from 0 °C to 250 °C, at 3 K/min. Initially, the resistance decrease with viscosity of epoxy mixture; the unchanged heat flow indicates the chemical reaction could be neglected in this moment. Due to accelerated polymerization, the resistance and heat flow start to increase, which we define the initial point of resistance or heat flow increase as on-set point. Subsequently, the resistance curves of these three mixtures display various peaks, for the stoichiometric systems, besides

the main peak, a smaller shoulder is also visible which is consistent with the plot of heat flow. The main peak characterizes the reaction between the oxirane function and the primary amine hydrogens which begins near room temperature. The shoulder at higher temperature is associated with the reaction of the secondary amine hydrogens [147]. Owing to the less primary amine concentration than the stoichiometric system, the secondary amine reaction has a more significant effect to polymerization, the resistance of epoxy-rich system keeps increasing to the second peak at 122 °C following first peak at 98 °C and a small plateau, at the same time, the exothermal curve shows a shoulder either. In the FTIR result of epoxy-rich system (Figure 4.27), the normalized

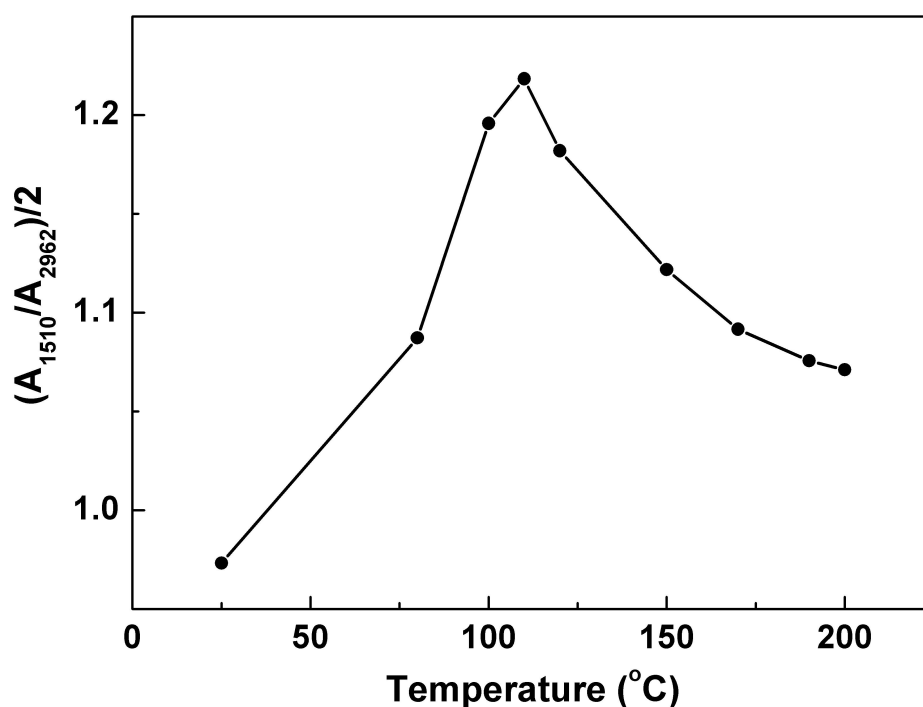


Figure 4.27: Plot of the normalized relative intensities of secondary amine group ( $1510\text{ cm}^{-1}$ ) versus temperature for epoxy-rich system during dynamic curing

relative intensity of secondary amine group ( $1510\text{ cm}^{-1}$ ) continuously increases below  $110\text{ }^{\circ}\text{C}$  and then significantly decreases, which means the reaction between epoxy and secondary amine functional groups has more contribution to the polymerization above  $110\text{ }^{\circ}\text{C}$ . Because of excess amine functional groups, the second peak of hardener-rich system in both resistance and exothermal curves disappear.

As the incipient formation of 3D molecular structure, the charge carriers from matrix are restricted, the tendency of the total resistance of measurement system is determined primarily by the NTC resistance of carbon nanotubes network which decrease with temperature increase. However, around 215 °C, the resistance of epoxy-rich system display another distinctive peak which is not present in stoichiometric and hardener-rich system. It might be the reason that the etherification reaction usually occurs in epoxy-rich systems, at higher temperature and in the later stages of cure, due to the amine groups being almost exhausted [148–150].

Table 4.2: The reaction parameters during polymerization

Resin:Hardener	$T_{on-set}$ (°C)		$T_{g\infty}$ (°C)		$E_a$ (kJ/mol)	
	R	DSC	R	DSC	R	DSC
100:25	36	37	69	62	48.0±6.1	52.9±1.3
100:34	24	29	113	111	60.8±7.1	58.3±3.3
100:45	10	24	111	112	52.0±13.0	56.3±10.6

Owing to the high sensitivity of CNTs network, this interphase sensor could be used to observe the glass transition of cured resin. Figure 4.26(d) shows the resistance change during cooling process from 250 °C to 0 °C, at 5 K/min, after the resin being cured. For the cured resin, the total resistance is mainly determined by the semiconductive interphase which approximately linearly increase with an decrement in temperature, because most of the charge carriers of matrix have been restricted by a highly crosslinked, three-dimensional network. With an decrement in temperature, the glass transition occurs, the amorphous liquid changes into the amorphous solid, the motion of molecular chains are “freezed” and the microstress is produced by the transistor of states. These factors influence the conductivity of CNT network, consequently, there is a steep increase in the resistance. The steepest increase in the resistance over the glass transistor range is found in epoxy-rich system, which indicates the more amount of amorphous materials and the lower crosslink density in this system than those in the stoichiometric and hardener-rich systems. Through making an inflexion point, the  $T_g$

could be evaluated, the results is listed in Table 4.2. From resistance results, we found the  $T_g$  of both hardener-rich system and epoxy-rich system are lower than that of stoichiometric system, associated with lower crosslink density and excess free volume in off-stoichiometric system [151].

Based on the Kissinger equation [152], the kinetic parameters are obtained by the variation of the peak temperature of resistance or exotherm,  $T_p$ , with respect to the heating rate  $\Psi$ :

$$E_a = -R \left[ \frac{d(\ln(\Psi/T_p^2))}{d(1/T_p)} \right] \quad (4.20)$$

where,  $E_a$  is the activation energy of the cure reaction,  $R$  the gas constant. Here, the heating rate  $\Psi$  is 1, 3, 5 K/min, respectively. The calculated activation energy through two methods is listed in Table 4.2. The calculated activation energy for the curing reaction through the resistance results is in good agreement with the DSC results. The small discrepancy may be attributed to the fact that resistance experiments required a much larger sample size than that was used in the DSC measurements [153].

#### 4.5.2 Monitoring the crystallization of thermoplastic polymer

As expected, the change of charge carriers mobility caused by melt and crystallization would also lead to the varied electrical resistance of crystalline polymeric materials, therefore, the MWNTs-glass fibre could be used to follow those processes. We put the PET film onto the MWNTs-glass fibre, then simultaneously recorded the resistance during the heating and cooling procedures.

##### 4.5.2.1 Non-isothermal crystallization

Figure 4.28 shows the evolution of the resistance during a non-isothermal cooling experiment which was carried out from 310 to 20 °C, at 3 K/min. The gray line in the Figure 4.28 is the absolute value of the normalized resistance derivation of tempera-

ture,  $|dR_N/dT|$ , which characterizes the rate of resistance change in a unite temperature. The slopes of both two ends of shadowed part almost keep constant, which means the resistance decreases at constant rate. But the latter is smaller. The low mobility is accounted for by the localization of the carriers within the structure and the impedance of carriers at crystalline-amorphous interphases. The carrier transport mechanism in polythene is consistent with a hopping transfer of electrons, the change of mobility,  $\mu$ , with temperature exhibits thermal activation characteristics and is described by an expression of the form [154]:

$$\mu = \mu_0 \exp\left(\frac{-W}{kT}\right) \quad (4.21)$$

where,  $W$  and  $k$  are the potential energy barrier, Boltzmann constant, respectively. With a decrement in temperature, the increased viscosity of polymer makes the higher  $W$ . Before the shadowed part, the faster increase of resistance is caused by the combine of the reduction of the carriers' mobility in liquid polymer and NTC effect of CNTs. After the shadowed part, *NTC* effect of CNTs is main reason for the increment of resistance.

At the shadowed part, the  $|dR_N/dT|$  is continuously declining which is attributed to the amorphous-semicrystallization transition. The trapping of crystalline/amorphous interphase and the increased barriers to carrier transport confine the displacement of the charge carriers in the amorphous phase of PET. Consequently, the rate of resistance change keeps reducing during crystallization process. The dark shadowed part shows the highest rate of the slope decline, which indicates the primary crystallization, the nucleation and growth of spherulites. And the temperature in the fastest declining point of the slope is consistent with the exothermal peak of DSC. Then, the rate of slope decline in light shadowed part becomes slower owing to the secondary crystallization process in amorphous interstices [155, 156]. Furthermore, the smaller constant of slope between melt temperature (about 240 °C) and the shadowed part might relate to the formation of mesomorphic precursor phase [157].

During second heat cycle, the slopes of resistance-temperature of semicrystalline

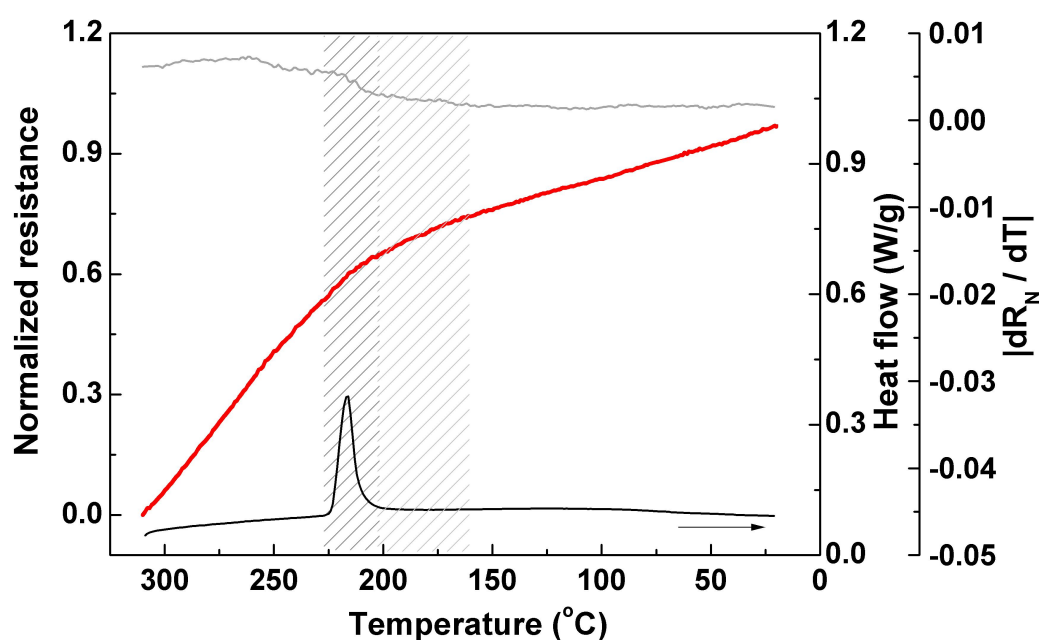


Figure 4.28: The changes of resistance and heat flow during non-isothermal crystallization of PET. The red and black curves are the normalized resistance and heat flow curves, respectively. The shadowed part means the crystalline process. The gray line is the absolute value of the normalized resistance derivation of temperature

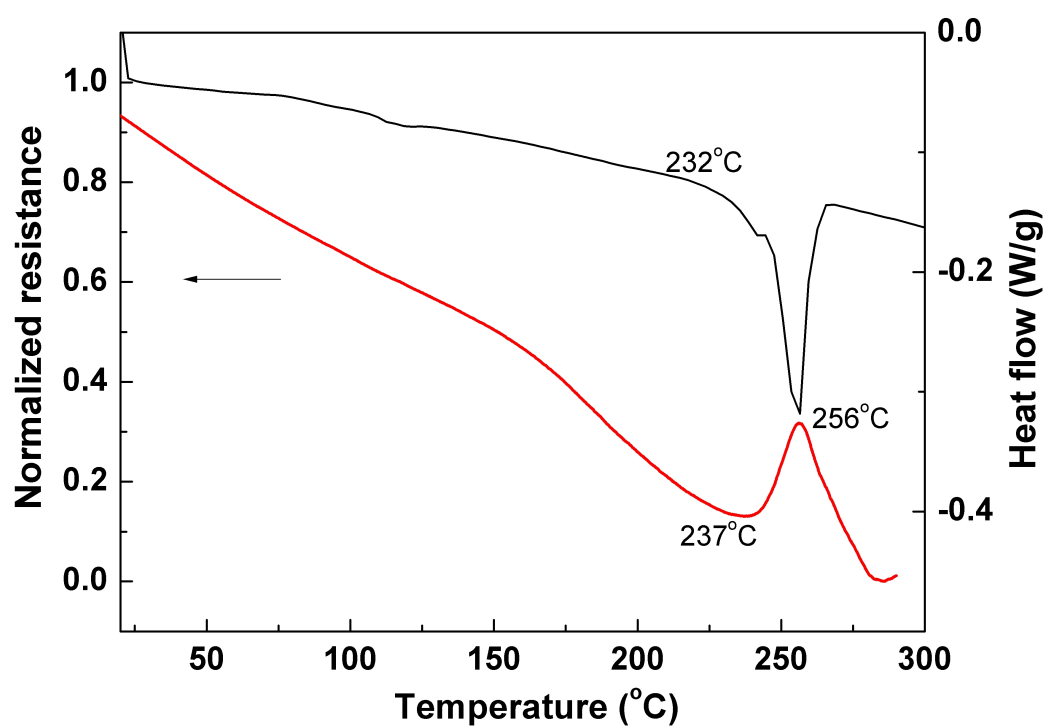


Figure 4.29: The changes of resistance and heat flow during the melting process of PET

PET vary in Figure 4.29, which caused by glass transition. A peak associated with melting of PET is observed at the end of the curve which is close to the DSC result. Because some interjunctions of the CNTs network are destroyed by flowing liquid, the resistance significantly increase.

#### 4.5.2.2 Isothermal crystallization

For analysis of the isothermal crystallization, the samples were heated to 310 °C, held for 10 min to erase thermal history effects, and then cooled rapidly (30 K/min) to the desired temperature for isothermal crystallization. Figure 4.30 shows the relationship between resistance and crystalline process, initially, the resistance sharply decreases with temperature. During isothermal stage at 230 °C, the resistance firstly reaches a plateau; subsequently, the resistance starts to rise which means the appearance of the crystalline phase. The crystalline phase leads to a decrease in the molecular mobility of the amorphous chains, which provokes a increase in the resistance. Besides, it is also the reason that the displacement of charged carriers in amorphous and the structure of CNTs network are modified by presence of crystalline entities [158, 159]. After crystallization, the resistance reaches the higher plateau.

For isothermal process at 220 °C, instead of the isothermal plateau, the continuous increasing of resistance indicates the occurrence of the fast crystallization. When the crystallization is almost completed, the resistance reaches the plateau. Through the simultaneous optical images in Figure 4.30, the process of the gradual growth of crystals can be captured at higher crystalline temperature, while the process of growth of crystals is too fast to be identified for the crystallization at lower temperature. The onset time of crystallization is delayed in DSC results relative to the resistance results, which probably caused by different mechanism and single fibre.

In summary, the MWNTs-glass fibre was used as a *in-situ* sensor to characterize the physical/chemical change of polymer through monitoring the low mobility of charge carriers in insulative materials. Owing to the high sensitivity to micro stress/strain,



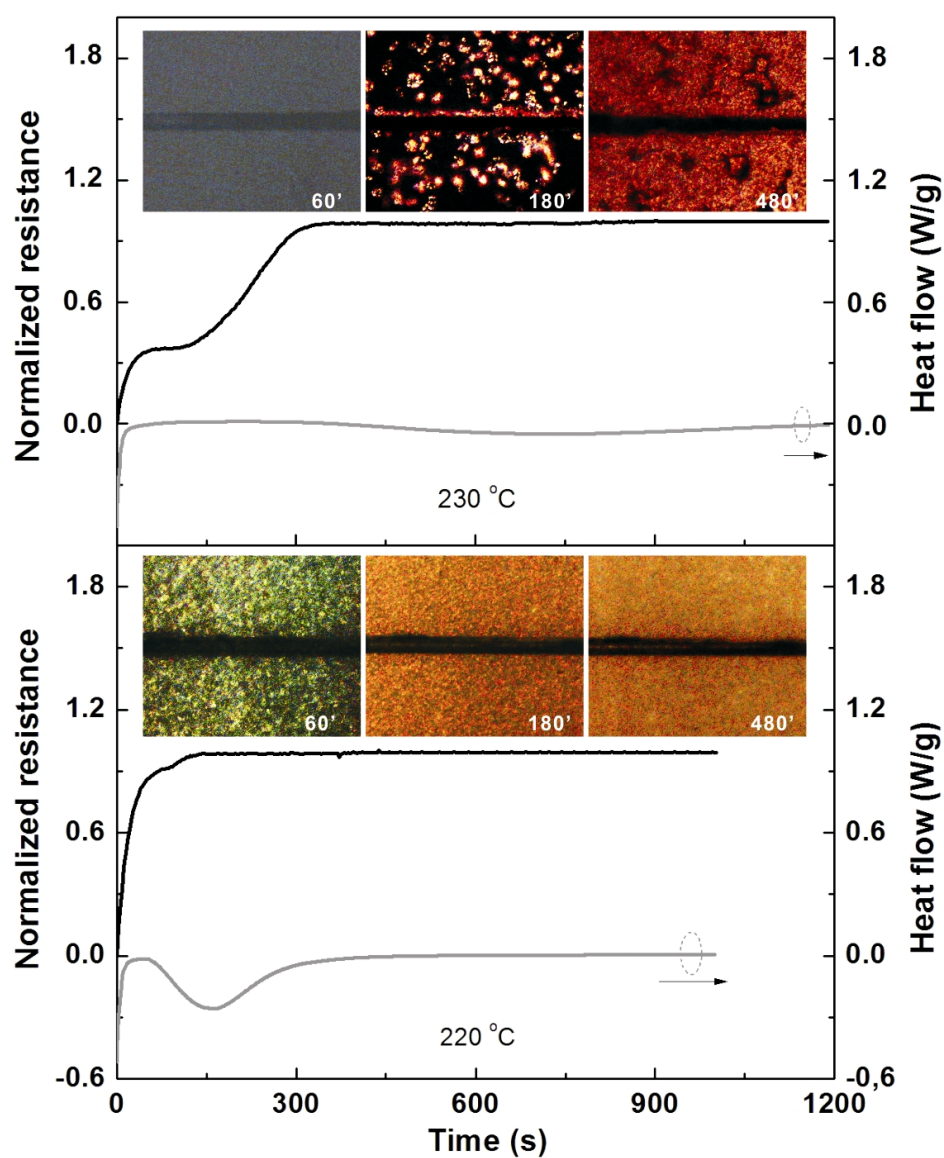


Figure 4.30: The changes of resistance and heat flow for the isothermal crystallization of PET at 220 °C and 230 °C, respectively. The inserted figures are the simultaneous optical images of isothermal crystallization of PET

the interphase can “feel” the motion of restricted molecular chains, therefore, the glass transition was interpreted by the resistance measurement for the first time.

## 5 Summary and Outlook

### 5.1 Summary

Carbon nanotubes have been introduced into the interphase between insulative glass fibre and polymer matrix to functionalize the traditional composite. Owing to the distribution of network structure of CNTs, the interphase can transfer the signals about various internal changes of material. Consequently, the MWNT-glass fibre shows a unique opportunity as a micro-scale multifunctional sensor. The following conclusions can be drawn:

- For the first time, carbon nanotubes were deposited onto the surface of the insulative glass fibre through electrophoretic deposition (EPD) and dip coating (DIP) method and a conductive pathway can be created by the randomly oriented carbon nanotube networks on the curved fibre surface. The electrical resistance value of coated fibres reached the semiconductive range.
- The electrical resistance values of single fibres coated by EPD scattered much smaller than that by dip coating, which indicates the EPD coating was more homogeneous and continuous. It is confirmed by SEM and AFM images that the quality of EPD coating is better.
- The coated fibres through EPD method also achieved the higher interfacial shear strength without degradation of the fibre strength compared with the control fibre and DIP fibre. The interfacial shear strength of single EPD fibre composites exhibited more than 30 % improvement, irrespective of whether the coating in-

cludes silane coupling agent or not.

- Related to the differently treated glass fibres, three interphase structures were proposed, which were consistent with fragment length results of Weibull distribution analysis. The EPD method produced mid-homogeneous coating, resulting in heterogeneous interphase coexistence similar with the structure of biological bone. The deposition of MWNTs by dip coating created inhomogeneous interphases, led to a decrease of the single fibre tensile strength and inhomogeneous interphase stress distribution.
- The semiconductive MWNTs-glass fibre demonstrated the high sensitivity to the stress/strain through the simultaneous measurement of the electrical resistance under tensile loading. The strain sensitivity factor,  $GF$ , of MWNTs-glass fibre is much higher than those of conventional metallic strain gages with geometrical piezoresistive effect, which display a potential as *in-situ* micro sensor in materials.
- The semiconductive interphase was formed when the MWNTs-glass fibre was embedded in polymer matrix. This semiconductive interphase is very sensitive to the deformation of material, therefore, an *in-situ* strain sensor was manufactured to real-time monitor the microcrack in composites instead of external sensors. At the same time, the *in-situ* strain sensor showed a unique ability of predicting the fracture of material in advance.
- Furthermore, three individual MWNTs-glass fibres were embedded into the matrix, the resistance increases sharply and step-wise with the three fibres broken one by one, which acted as three variable resistors connected in parallel. Obviously, the multi-individual fibre composite improves the early warning capability and sensitivity with regards to the “material’s health”.
- Monitoring the resistance variation of the single fibre composite was conducted under cyclic loading with progressively increasing the strain peaks in order to further investigate the response of *in-situ* sensor to the interphase damage pro-

cess. The relatively large difference in deformation among each cycle highlights the accumulation of damage, which gives insight into the mechanism of resistance change.

- Utilizing the microcrack associated with fibre breakage, a new concept electromechanical switch was manufactured and the “junction-break” mechanism was proposed to characterize the switch. The electric circuit turned “ON” or “OFF” with the closing or opening of microcrack, which followed the connection or disconnection of CNTs network concentrated in the fibre/matrix interphase.
- The electromechanical switch could be actuated by heat resource either, which further confirmed the “junction-break” mechanism. Since the shrinking of microcrack caused by thermal expansion of composite, the switch achieves the conversion ON-OFF state. The preliminary experiment of visible light illumination driving the switch confirmed the probability of exploring other kind of actuated energy.
- Without high electrical field, the MWNTs-glass fibre was used as an *in-situ* physical-chemical sensor to characterize the processes of polymerization or crystallization of polymers through monitoring the low mobility of charge carriers in insulative materials. The glass transition was interpreted by the resistance measurement for the first time.

## 5.2 Outlook

Introducing nano-scale material into the interphase of composites is a promising approach to develop multifunctional materials. It will be continued the intensive study in the functionalizing of the traditional and green composites in following routes:

- The more detail for the present research will also be investigated. The lowest concentration of CNTs dispersion for the formation of conductive path onto glass will be investigated through a series of comparative experiments. Besides, some important parameters, such as the response time of single fibre sensor in composites, service life of micro-switch will be further studied.
- Because the MWNT-glass fibres can be arranged along the various orientations, the anisotropy of multifunctional composites will be prepared in the future. The different properties at various directions, such as electrical conductivity, thermal conductivity and so on, will be analyzed.
- Besides carbon nanotubes, other kinds of nano-scale materials will be applied to achieve more various functions, for instance, graphene, a single sheet composed of  $sp^2$ -hybridized carbon, has drawn great attention owing to its outstanding electronic, optical, thermal and mechanical properties. The unique 2D structure and excellent electronic properties of graphene, particularly its high mobility, and the handy availability of functionalized graphene, together with its chemical stability, render it a competitive alternative as the electron-accepting material in Organic photovoltaic applications [160]. Therefore, graphene can be introduced into the interphase between fibre and matrix to develop a new photoelectric materials.
- Biological materials are usually complex macromolecular assemblies, often surrounding the cells in an organ in the form of an extracellular matrix. The interphases between these building blocks can increase resistance to fracture, join materials of different character, make them deform more easily and provide

motility [161]. One design strategy to improve the mechanical property of composites is mimicking the structure of biomaterial. A gradient interphase is one of research subjects in next step, which mitigate the incompatibilities between glass fibre and polymer matrix is to gradually change materials properties. Controlling the concentration of nanoparticle dispersions might be a feasible approach. Additionally, green composites combining nanoparticle and nature material, such as nature fibre, will become the other interesting investigation in the future work.

# Appendix

## List of Figures

1.1	Overview of the work plan . . . . .	3
2.1	Applications of GFRPs . . . . .	5
2.2	Pictures of glass fibre spinning and sizing devices . . . . .	7
2.3	Structure of DGEBA . . . . .	9
2.4	Chemical reactions for a epoxy-amine system . . . . .	10
2.5	Schematic diagram of interphase in FRP . . . . .	12
2.6	Propagations of cracks in composite with different interphase . . .	13
2.7	Different test methods of interfacial strength for single fibre model composite . . . . .	14
2.8	Structures of CNTs . . . . .	17
2.9	The Stone-Wales transformation . . . . .	18
3.1	Schematic illustrations of MWNTs dispersion and EPD device . .	26
3.2	Streaming Potential of MWNTs dispersion . . . . .	28
3.3	The picture of the tensile test device for single filament . . . . .	30
3.4	Single fibre electrical resistance test . . . . .	31
3.5	Three failure modes of interphase . . . . .	33
3.6	The schematic diagram of single fibre pull-out test equipment . .	34
3.7	Device of tensile test for single fibre model composites . . . . .	36
4.1	Morphologies of coated glass fibres by different methods . . . . .	40
4.2	Electrical double layer distortion and thinning mechanism for elec- trophoretic deposition . . . . .	41
4.3	Designation of interphase inspired by biological bone structure . .	43
4.4	Critical aspect ratio of single fibre composites in fragmentation test	44
4.5	The interfacial shear strength based on pull-out test under different treatment conditions . . . . .	45

4.6	Images and strength of interphase between MWNTs-glass fibre and matrix . . . . .	48
4.7	Weibull distribution of fragmentation length of single fibre in composite . . . . .	49
4.8	Three types proposed interphase and various failure modes of interphase . . . . .	51
4.9	Sensitivity of single MWNTs-glass fibre for strain . . . . .	54
4.10	Single MWNTs-glass fibre strain sensor . . . . .	56
4.11	Optimized strain sensor with multi-individual fibres . . . . .	57
4.12	Single MWNTs-glass fibre used as sensor in glass facade . . . . .	58
4.13	The <i>in-situ</i> sensor response to cyclic tensile loading . . . . .	59
4.14	Schematic of microcrack bridged by MWNTs in a single fibre/epoxy composite . . . . .	62
4.15	Performance of the micro switch of single fibre model composite based on “junction-break” mechanism . . . . .	63
4.16	SEM images display the CNT network bridge in switch . . . . .	64
4.17	Analysis of stress for fibre in single fibre composite. . . . .	64
4.18	The behavior of electromechanical switch actuated by temperature. . . . .	67
4.19	Dependence of the electrical resistance on temperature of the single MWNTs-glass fibre and single MWNTs-glass fibre composite . . . . .	68
4.20	The switch actuated by visible light . . . . .	69
4.21	The schematic diagram of chemical sensor . . . . .	73
4.22	The change of electrical resistance dependent on temperature . . . . .	75
4.23	The resistance change during isothermal polymerization . . . . .	76
4.24	The time-temperature-transformation ( <i>TTT</i> ) cure diagram. . . . .	78
4.25	The relative degree of conversion for polymerization . . . . .	79
4.26	The changes of resistance and heat flow during dynamic polymerization . . . . .	80
4.27	Plot of the normalized relative intensities of secondary amine group versus temperature for epoxy-rich system . . . . .	81
4.28	The changes of resistance and heat flow during non-isothermal crystallization of PET . . . . .	85
4.29	The changes of resistance and heat flow during the melting process of PET . . . . .	85
4.30	The changes of resistance and heat flow during isothermal crystallization of PET . . . . .	87



## List of Tables

2.1	Weight percentage of components in different types of glass fibre [21] . . . . .	6
2.2	Properties for different types of glass fibre [21] . . . . .	8
3.1	Surface treatment conditions of AR glass fibres . . . . .	28
3.2	Mechanical properties of AR-glass fibre and epoxy matrix . . . . .	35
4.1	Average single fibre tensile strength for different gauge length ( $L_0$ )	46
4.2	The reaction parameters during polymerization . . . . .	82

## Bibliography

- [1] BERG, J. ; JONES, F. R.: The role of sizing resins, coupling agents and their blends on the formation of the interphase in glass fibre composites. In: *Composites Part A: Applied Science and Manufacturing* 29 (1998), S. 1261 – 1272
- [2] WAMBUA, P. ; IVENS, J. ; VERPOEST, I.: Natural fibres: can they replace glass in fibre reinforced plastics? In: *Composites Science and Technology* 63 (2003), S. 1259 – 1264
- [3] MAEDER, E. ; JACOBASCH, H. J. ; GRUNDKE, K. ; GIETZELT, T.: Influence of an optimized interphase on the properties of polypropylene/glass fibre composites. In: *Composites Part A: Applied Science and Manufacturing* 27 (1996), S. 907–912
- [4] CHO, J. ; CHEN, J. Y. ; DANIEL, I. M.: Mechanical enhancement of carbon fiber/epoxy composites by graphite nanoplatelet reinforcement. In: *Scripta Materialia* 56 (2007), S. 685–688
- [5] SHAHID, N. ; VILLATE, R. G. ; BARRON, A. R.: Chemically functionalized alumina nanoparticle effect on carbon fiber/epoxy composites. In: *Composites Science and Technology* 65 (2005), S. 2250–2258
- [6] ZHANG, J. ; LIU, J. W. ; ZHUANG, R. C. ; MAEDER, E. ; HEINRICH, G. ; GAO, S. L.: Single MWNT-glass fiber as strain sensor and switch. In: *Advanced Materials* 23 (2011), S. 3392–3397
- [7] SALVETAT-DELMOTTE, J.-P. ; RUBIO, A.: Mechanical properties of carbon nanotubes: a fiber digest for beginners. In: *Carbon* 40 (2002), S. 1729 – 1734
- [8] TREACY, M. M. J. ; EBBESEN, T. W. ; GIBSON, J. M.: Exceptionally high Young's modulus observed for individual carbon nanotubes. In: *Nature* 381 (1996), S. 678–680
- [9] WONG, E. W. ; SHEEHAN, P. E. ; LIEBER, C. M.: Nanobeam mechanics: elasticity, strength, and toughness of nanorods and nanotubes. In: *Science* 277 (1997), S. 1971–1975
- [10] SCHADLER, L. S. ; GIANNARIS, S. C. ; AJAYAN, P. M.: Load transfer in carbon nanotube epoxy composites. In: *Applied Physics Letters* 73 (1998), S. 3842–3844

- [11] RUAN, S. L. ; GAO, P. ; YANG, X. G. ; YU, T. X.: Toughening high performance ultrahigh molecular weight polyethylene using multiwalled carbon nanotubes. In: *Polymer* 44 (2003), S. 5643 – 5654
- [12] NORWOOD, L. S. ; HOLLAWAY, L. (Hrsg.): *Handboo of polymer composites for engineers*. Cambridge CBI 6AH. England : Woodhead Publishing Ltd, 1994. – 21–33 S.
- [13] REINHART, T. J. ; PETERS, S. T. (Hrsg.): *Handbook of composites*. London SE1 8HN, United Kingdom : Chapma and Hall, 1998. – 22–23 S.
- [14] HAMERTON, I. ; DOLBEY, R. (Hrsg.): *Recent developments in epoxy resins*. Shropshire SY4 4NR, United Kingdom : Rapra Technology Limited, 1997. – 58 S.
- [15] DRZAL, L. T. ; MADHUKAR, M. S.: Fibre-matrix adhesion and its relationship to composite mechanical properties. In: *Journal of Material Science* 28 (1993), S. 569–610
- [16] MADHUKAR, M. S. ; DRZAL, L. T.: Fiber-matrix adhesion and its effect on composite mechanical properties. III. longitudinal (0) compressive properties of graphite/epoxy composites. In: *Journal of Composite Materials* 26 (1992), S. 310–333
- [17] GARDINER, G.: The making of glass fibre. In: *Composites Technology* (2009)
- [18] STARR, T. F. ; STARR, T. F. (Hrsg.): *Glass-fibre directory and databook*. London SE1 8HN, UK : Chapma and Hall, 1997. – vii S.
- [19] WALLENBERGER, F. T. ; WALLENBERGER, F. T. (Hrsg.) ; BINGHAM, P. A. (Hrsg.): *Fiberglass and glass Technology: Energy-Friendly Compositions and Applacation*. Bd. 1. New York, USA : London: Springer, 2009. – 3–60 S.
- [20] <http://en.wikipedia.org/wiki/Fiberglass>
- [21] HARTMAN, D. ; GREENWOOD, M. E. ; MILLE, D. M.: High Strength Glass Fibers / Owens Corning Corporation. 1996. – Forschungsbericht
- [22] <http://www.hexcel.com/products/allproducts>
- [23] VEPA, R. ; VEPA, R. (Hrsg.): *Dynamics of Smart Structures*. John Wiley and Sons, 2010
- [24] POCIUS, A. V. ; POCIUS, A. V. (Hrsg.): *Adhesion and adhesives technology: an introduction*. Hanser Gardner Publication, 2002

- [25] PASCAULT, J.-P. ; WILLIAMS, R. J. J. ; PASCAULT, J.-P. (Hrsg.) ; WILLIAMS, Roberto J. J. (Hrsg.): *Epoxy polymers: new materials and innovations*. Weinheim, German : Wiley-VCH, 2010. – 1–12 S.
- [26] WELDON, D. G.: *Failure analysis of paints and coatings*. The Atrium, Southern Gate, Chichester, West Sussex, PO19 8SQ, United Kingdom : John Wiley and Sons, 2009. – 73–79 S.
- [27] <http://sunilbhangale.tripod.com/epoxy.html>
- [28] VANLANDINGHAM, M. R. ; EDULJEE, R. F. ; GILLESPIE JR., J. W.: Relationships between stoichiometry, microstructure, and properties for amine-cured epoxies. In: *Journal of Applied Polymer Science* 71 (1999), S. 699–712
- [29] PICCAROLO, S. ; BRUCATO, V. ; KIFLIE, Z.: Non-Isothermal Crystallization Kinetics of PET. In: *POLYMER ENGINEERING AND SCIENCE* 40 (2000), S. 1263–1272
- [30] GAO, S. L. ; MAEDER, E.: Characterisation of interphase nanoscale property variations in glass fibre reinforced polypropylene and epoxy resin composites. In: *Composites Part A: Applied Science and Manufacturing* 33 (2002), S. 559 – 576
- [31] TANG, L. G. ; KARDOS, J. L.: A review of methods for improving the interfacial adhesion between carbon fiber and polymer matrix. In: *Polymer Composites* 18 (1997), S. 100–113
- [32] HAYES, S. A. ; LANE, R. ; JONES, F. R. ; FOUND, M. S. (Hrsg.): *Experimental techniques and design in composite materials 4*. Swets and Zeitlinger B. V., Lisse, The Netherlands : A. A. Balkema, 2002. – 157–158 S.
- [33] JANCAR, J. ; KARGER-KOCSIS, J. (Hrsg.) ; FAKIROV, S. (Hrsg.): *Nano- and micro-mechanics of polymer blends and composites*. Ohio 45244-3029, USA : Hanser Publications, 2009. – 241–248 S.
- [34] FRIIS, E. A. ; HAHN, D. L. ; COOKE, F. W. ; HOOPER, S. J. ; ARMANIOS, E. A. (Hrsg.): *Composite materials: fatigue and fracture*. American Society for Testing and Materials, 1997. – 364–366 S.
- [35] GRANDE, D. H. ; MANDELL, J. F. ; HONG, K. C. C.: Fibre-matrix bond strength studies of glass, ceramic, and metal matrix composites. In: *Journal of Materials Science* 23 (1988), S. 311–328
- [36] HULL, D. ; CLYNE, T. W.: *An introduction to composite materials*. Cambridge : Cambridge University Press, 1996. – 135–137 S.

- [37] KIM, J.-K. AND MAI, Y.-W.: *Engineered interfaces in fiber reinforced composites*. Kidlington, Oxford OX5 1GB, United Kingdom : Elsevier Science Ltd, 1998. – 1–38 S.
- [38] TSAI, J.-L. ; WU, M.-D.: Organoclay effect on mechanical responses of glass/epoxy nanocomposites. In: *Journal of Composite Materials* 42 (2008), S. 553–568
- [39] COLEMAN, J. N. ; KHAN, W. J. U. and Blau B. U. and Blau ; GUN'KO, Y. K.: Small but strong: A review of the mechanical properties of carbon nanotube-polymer composites. In: *Carbon* 44 (2006), S. 1624 – 1652
- [40] MA, P.-C. ; KIM, J.-K.: *Carbon nanotubes for polymer reinforcement*. 6000 Broken Sound Parkway NW, Suite 300, United States of America : CRC Press, 2011. – 1–34 S.
- [41] THOSTENSON, E. T. ; REN, T.-W. Z. F. and C. Z. F. and Chou: Advances in the science and technology of carbon nanotubes and their composites: a review. In: *Composites Science and Technology* 61 (2001), S. 1899 – 1912
- [42] NARDELLI, M. B. ; I., Yakobson B. ; J., Bernholc: Brittle and Ductile Behavior in Carbon Nanotubes. In: *Phys. Rev. Lett.* 81 (1998), Nr. 21, S. 4656–4659
- [43] YAKOBSON, B. I. ; SAMSONIDZE, G. ; SAMSONIDZE, G. G.: Atomistic theory of mechanical relaxation in fullerene nanotubes. In: *Carbon* 38 (2000), S. 1675 – 1680
- [44] SCHAEFER, H.-E.: *Nanoscience. The science of the small in physics, engineering, chemistry, biology and medicine*. Heidelberg, Germany : Springer, 2010. – 220–223 S.
- [45] SALVETAT, Jean-Paul ; KULIK, Andrzej J. ; BONARD, Jean-Marc ; BRIGGS, G. Andrew D. ; STOECKLI, Thomas ; MÉTÉNIER, K. ; BONNAMY, S. ; FORRÓ, L.: Elastic modulus of ordered and disordered multiwalled carbon nanotubes. In: *Advanced Materials* 11 (1999), S. 161–165
- [46] SALVETAT, J.-P. ; BRIGGS, G. A. D. ; BONARD, J.-M. ; BACSA, R. R. ; KULIK, A. J. ; STOECKLI, T. ; BURNHAM, N. A. ; FORRÓ, L.: Elastic and shear moduli of single-walled carbon nanotube ropes. In: *Physical Review Letter* 82 (1999), S. 944–947
- [47] YU, M.-F. ; FILES, B. S. ; AREPALLI, S. ; RUOFF, R. S.: Tensile loading of ropes of single Wall carbon nanotubes and their mechanical properties. In: *Phys. Rev. Lett.* 84 (2000), S. 5552–5555
- [48] AJAYAN, P. M.: Nanotubes from Carbon. In: *Chemical Reviews* 99 (1999), S. 1787–1800

- [49] TANS, S. J. ; DEVORET, M. H. ; DAI, H. J. ; THESS, A. ; SMALLEY, R. E. ; GEERLIGS, L. J. ; DEKKER, C.: Individual single-wall carbon nanotubes as quantum wires. In: *Nature* 386 (1997), S. 474–477
- [50] DAI, H. J. ; DRESSELHAUS, M. S. (Hrsg.) ; DRESSELHAUS, G. (Hrsg.) ; AVOURIS, Ph. (Hrsg.): *Carbon nanotubes: synthesis, structure, properties, and applications*. Heidelberg, German : springer, 2001. – 29–51 S.
- [51] ZHOU, C. W. ; KONG, J. ; DAI, H. J.: Electrical measurements of individual semiconducting single-walled carbon nanotubes of various diameters. In: *Applied Physics Letters* 76 (2000), S. 1597–1599
- [52] LANGER, L. ; BAYOT, V. ; GRIVEI, E. ; ISSI, J.-P. ; HEREMANS, J. P. ; OLK, C. H. ; STOCKMAN, L. ; VAN HAESSENDONCK, C. ; BRUYNSERAEDE, Y.: Quantum transport in a multiwalled carbon nanotube. In: *Physical Review Letter* 76 (1996), Nr. 3, S. 479–482
- [53] PONCHARAL, P. ; WANG, Z. L. ; UGARTE, D. ; HEER, W. A.: Electrostatic deflections and electromechanical resonances of carbon nanotubes. In: *Science* 283 (1999), S. 1513–1516
- [54] KUNDURU, V. ; YADAV, Y. ; PRASAD, S. ; MORRIS, J. E. (Hrsg.): *Nanopackaging: nanotechnologies and electronics packaging*. New York, United States of American : Springer, 2008. – 356 S.
- [55] BERBER, S. ; KWON, Y-K ; TOMÁNEK, D.: Unusually high thermal conductivity of carbon nanotubes. In: *Physical Review Letter* 84 (2000), S. 4613–4616
- [56] KIM, P. ; SHI, L. ; MAJUMDAR, A. ; MCEUEN, P. L.: Thermal transport measurements of individual multiwalled nanotubes. In: *Phys. Rev. Lett.* 87 (2001), S. 215502
- [57] POP, E. ; MANN, D. ; WANG, Q. ; GOODSON, K. ; DAI, H. J.: Thermal conductance of an individual single-wall Carbon nanotube above room temperature. In: *Nano Letters* 6 (2006), S. 96–100
- [58] WANG, J. ; WANG, J.-S.: Carbon nanotube thermal transport: Ballistic to diffusive. In: *Applied Physics Letters* 88 (2006), S. 111909
- [59] PANG, L. S. K. ; SAXBY, J. D. ; CHATFIELD, S. P.: Thermogravimetric analysis of carbon nanotubes and nanoparticles. In: *The Journal of Physical Chemistry* 97 (1993), S. 6941–6942
- [60] AJAYAN, P. M. ; O., Stephan ; C., Colliex ; D., Trauth: Aligned Carbon Nanotube Arrays Formed by Cutting a Polymer Resin—Nanotube Composite. In: *Science* 265 (1994), S. 1212–1214

- [61] MA, P. C. ; SIDDIQUI, N. A. ; MAROM, G. ; KIM, J. K.: Dispersion and functionalization of carbon nanotubes for polymer-based nanocomposites: A review. In: *Composites Part A* 41 (2010), S. 1345–1367
- [62] SHAFFER, M. S. P. ; WINDLE, A. H.: Fabrication and characterization of carbon nanotube/poly(vinyl alcohol) Composites. In: *Advanced Materials* 11 (1999), S. 937–941
- [63] GRIMMER, C. ; DHARAN, C.: High-cycle fatigue of hybrid carbon nanotube/glass fiber/polymer composites. In: *Journal of Materials Science* 43 (2008), S. 4487–4492
- [64] BAUGHMAN, R. H. ; CUI, C. X. ; ZAKHIDOV, A. A. ; IQBAL, Z. ; BARISCI, J. N. ; SPINKS, G. M. ; WALLACE, G. G. ; MAZZOLDI, A. ; DE ROSSI, D. ; RINZLER, A. G. ; JASCHINSKI, O. ; ROTH, S. ; KERTESZ, M.: Carbon nanotube actuators. In: *Science* 284 (1999), S. 1340–1344
- [65] CHA, S. N. ; JANG, J. E. ; CHOI, Y. ; AMARATUNGA, G. A. J. ; KANG, D.-J. ; HASKO, D. G. ; JUNG, J. E. ; KIM, J. M.: Fabrication of a nanoelectromechanical switch using a suspended carbon nanotube. In: *Applied Physics Letters* 86 (2005), S. 083105
- [66] GAO, L. M. ; THOSTENSON, E. T. ; ZHANG, Z. G. ; CHOU, T.-W.: Sensing of damage mechanisms in fiber-reinforced composites under cyclic loading using carbon nanotubes. In: *Advanced Functional Materials* 19 (2009), S. 123–130
- [67] ZHAO, H. B. ; ZHANG, Y. Y. ; BRADFORD, P. D. ; ZHOU, Q. ; JIA, Q. X. ; YUAN, F.-G. ; ZHU, Y. T.: Carbon nanotube yarn strain sensors. In: *Nanotechnology* 21 (2010), S. 305502
- [68] HU, N. ; MASUDA, Z. ; YAMAMOTO, G. ; FUKUNAGA, H. ; HASHIDA, J. H. T. and Qiu Q. T. and Qiu: Effect of fabrication process on electrical properties of polymer/multi-wall carbon nanotube nanocomposites. In: *Composites Part A: Applied Science and Manufacturing* 39 (2008), S. 893 – 903
- [69] E., Flahaut ; R., Bacsa ; PEIGNEY, A. ; LAURENT, C.: Gram-scale CCVD synthesis of double-walled carbon nanotubes. In: *Chemical Communications* 12 (2003), S. 1442–1443
- [70] VAISMAN, L. ; WAGNER, H. D. ; MAROM, G.: The role of surfactants in dispersion of carbon nanotubes. In: *Advances in Colloid and Interface Science* 128-130 (2006), S. 37 – 46
- [71] ZHANG, J ; ZHUANG, R. C. ; LIU, J. W. ; MAEDER, E. ; HEINRICH, G. ; GAO, S. L.: Functional interphases with multi-walled carbon nanotubes in glass fibre/epoxy composites. In: *Carbon* 48 (2010), S. 2273 – 2281

- [72] BOCCACCINI, A. R. ; ZHITOMIRSKY, I.: Application of electrophoretic and electrolytic deposition techniques in ceramics processing. In: *Current Opinion in Solid State and Materials Science* 6 (2002), S. 251 – 260
- [73] BOCCACCINI, A. R. ; CHO, J. ; ROETHER, J. A. ; THOMAS, E. J. B. J. C. and Minay M. B. J. C. and Minay ; SHAFFER, M. S. P.: Electrophoretic deposition of carbon nanotubes. In: *Carbon* 44 (2006), S. 3149 – 3160
- [74] BIEST, O. O. d. ; VANDEPERRE, L. J.: Electrophoretic deposition of materials. In: *Annual Review of Materials Science* 29 (1999), S. 327–352
- [75] SARKAR, P. ; NICHOLSON, P. S.: Electrophoretic Deposition (EPD): mechanisms, kinetics, and application to ceramics. In: *Journal of the American Ceramic Society* 79 (1996), S. 1987–2002
- [76] BEKYAROVA, E. ; THOSTENSON, E. T. ; YU, A. ; KIM, H. ; GAO, J. ; TANG, J. ; HAHN, H. T. ; CHOU, T.-W. ; ITKIS, M. E. ; HADDON, R. C.: Multiscale carbon nanotube - carbon fiber reinforcement for advanced epoxy composites. In: *Langmuir* 23 (2007), S. 3970–3974
- [77] BOCCACCINI, A. R. ; CHICATUN, J. F. and C. F. and Cho ; BRETCANU, O. ; ROETHER, J. A. ; NOVAK, S. ; CHEN, Q. Z.: Carbon nanotube coatings on bioglass-based tissue engineering scaffolds. In: *Advanced Functional Materials* 17 (2007), S. 2815–2822
- [78] SANTILLÁN, M. J. ; CANEIRO, A. ; LOVEY, F. C. ; QUARANTA, N. ; BOCCACCINI, A. R.: Electrophoretic codeposition of  $\text{La}_{0.6}\text{Sr}_{0.4}\text{Co}_{0.8}\text{Fe}_{0.2}\text{O}_{3-\delta}$  and carbon nanotubes for developing composite cathodes for intermediate temperature solid oxide fuel cells. In: *International Journal of Applied Ceramic Technology* 7 (2010), S. 30–40
- [79] TAKAOKI, N. ; TAKAHISA, T. ; YUJI, H. ; MASAKI, Y. ; KOJI, W.: Effects of alumina hydrates formed by hydration of hydraulic alumina on green strength and microstructure of porous alumina ceramics. In: *Journal of the Ceramic Society of Japan* 114 (2006), S. 214–216
- [80] GAO, S. L. ; ZHUANG, R. C. ; ZHANG, J. ; LIU, J. W. ; MAEDER, E.: Glass fibers with carbon nanotube networks as multifunctional sensors. In: *Advanced Functional Materials* 20 (2010), S. 1885–1893
- [81] MORCOM, M. ; ATKINSON, K. ; SIMON, G. P.: The effect of carbon nanotube properties on the degree of dispersion and reinforcement of high density polyethylene. In: *Polymer* 51 (2010), S. 3540 – 3550
- [82] DART, S. L. ; PETERSON, L. E.: An improved vibroscope. In: *Textile Research Journal* 22 (1952), S. 819–822



- [83] DIMAKI, M. ; BOGGILD, P.: Investigation of parameters controlling the dielectrophoretic assembly of carbon nanotubes on microelectrodes. In: *Journal of Nanoscience and Nanotechnology* 8 (2008), S. 1973–1978
- [84] NETRAVALI, A. N. ; HENSTENBURG, R. B. ; PHOENIX, S. L. ; SCHWARTZ, P.: Interfacial shear strength studies using the single-filament-composite test. I: Experiments on graphite fibers in epoxy. In: *Polymer Composites* 10 (1989), S. 226–241
- [85] KELLY, A. ; TYSON, W. R.: Tensile properties of fibre-reinforced metals: Copper/tungsten and copper/molybdenum. In: *Journal of the Mechanics and Physics of Solids* 13 (1965), S. 329 – 338, in1–in2, 339–350
- [86] PISANOVA, E. V. ; ZHANDAROV, S. F. ; DOVGYALO, V. A.: Interfacial adhesion and failure modes in single filament thermoplastic composites. In: *Polymer Composites* 15 (1994), S. 147–155
- [87] ZHOU, X. F. ; NAIRN, J. A. ; WAGNER, H. D.: Fiber-matrix adhesion from the single-fiber composite test: nucleation of interfacial debonding. In: *Composites Part A: Applied Science and Manufacturing* 30 (1999), S. 1387 – 1400
- [88] MULLIN, J. V. ; MAZZIO, V. F.: The effects of matrix and interface modification on local fractures of carbon fibers in epoxy. In: *Journal of the Mechanics and Physics of Solids* 20 (1972), S. 391 – 394
- [89] MILLER, B. ; MURI, P. ; REBENFELD, L.: A microbond method for determination of the shear strength of a fibre-resin interface. In: *Composite Science and Technology* 28 (1987), S. 17–32
- [90] JENSCHKE, W.: Bedienungsanleitung und technische Programmbeschreibung zum Programm Pullout 2, Version 2.0. / Leibniz-Institut für Polymerforschung Dresden e. V., Abt. FK. 2003. – Forschungsbericht
- [91] BANG, K. G. ; KWON, J. W. ; LEE, D. G. ; LEE, J. W.: Measurement of the degree of cure of glass fiber–epoxy composites using dielectrometry. In: *Journal of Materials Processing Technology* 113 (2001), S. 209–214
- [92] DERYAGUIN, B. V. ; LANDAU, L. D.: A theory of the stability of strongly charged lyophobic sols and of the adhesion of strongly charged particles in the solution of electrolytes. In: *Acta Physicochim: USSR* 14 (1941), S. 633
- [93] VERWEY, E. J. W. ; OVERBEEK, J. Th. G.: *Theory of the stability of lyophobic colloids*. Amsterdam : Elsevier, 1948
- [94] BESRA, L. ; LIU, M.: A review on fundamentals and applications of electrophoretic deposition (EPD). In: *Progress in Materials Science* 52 (2007), S. 1 – 61

- [95] GUPTA, H. S. ; WAGERMAIER, W. ; ZICKLER, G. A. ; RAZ-BEN AROUSH, D. ; FUNARI, S. S. ; ROSCHGER, P. ; WAGNER, H. D. ; FRATZL, P.: Nanoscale deformation mechanisms in Bone. In: *Nano Letters* 5 (2005), S. 2108–2111
- [96] DUNLOP, J. W. C. ; WEINKAMER, R. ; FRATZL, P.: Artful interfaces within biological materials. In: *Materials Today* 14 (2011), S. 70 – 78
- [97] KATZ, J. L.: Anisotropy of Young's modulus of bone. In: *Nature* 283 (1980), S. 106–107
- [98] SETO, J. ; GUPTA, H. S. ; ZASLANSKY, P. ; WAGNER, H. D. ; FRATZL, P.: Tough lessons from bone: extreme mechanical anisotropy at the mesoscale. In: *Advanced Functional Materials* 18 (2008), S. 1905–1911
- [99] RHO, J.-Y. ; KUHN-SPEARING, L. ; ZIOUPOS, P.: Mechanical properties and the hierarchical structure of bone. In: *Medical Engineering & Physics* 20 (1998), S. 92 – 102
- [100] GAO, S. L. ; MAEDER, E. ; PLONKA, R.: Nanocomposite coatings for healing surface defects of glass fibers and improving interfacial adhesion. In: *Composites Science and Technology* 68 (2008), S. 2892 – 2901
- [101] XU, X. J. ; THWE, M. M. ; SHEARWOOD, C. ; LIAO, K.: Mechanical properties and interfacial characteristics of carbon-nanotube-reinforced epoxy thin films. In: *Applied Physics Letters* 81 (2002), S. 2833–2835
- [102] PARK, S.-J. ; JIN, J.-S.: Effect of Silane Coupling Agent on Interphase and Performance of Glass Fibers/Unsaturated Polyester Composites. In: *Journal of colloid and interface science* 242 (2001), S. 174 – 179
- [103] SHAM, M.-L. ; KIM, J.-K.: Surface functionalities of multi-wall carbon nanotubes after UV/Ozone and TETA treatments. In: *Carbon* 44 (2006), S. 768 – 777
- [104] SIDDIQUI, N. A. ; SHAM, M.-L. ; TANG, B. Z. ; MUNIR, A. ; KIM, J.-K.: Tensile strength of glass fibres with carbon nanotube-epoxy nanocomposite coating. In: *Composites Part A: Applied Science and Manufacturing* 40 (2009), S. 1606 – 1614
- [105] GAO, S. L. ; MAEDER, E. ; ABDKADER, A. ; OFFERMANN, P.: Sizings on alkali-resistant glass fibers: environmental effects on mechanical properties. In: *Langmuir* 19 (2003), S. 2496–2506
- [106] MALLICK, P. K.: *Fiber-reinforced composites: materials, manufacturing, and design*. Marcel Dekker, New York : CRC Press, 1993. – 130 S.

- [107] CADEK, M. ; COLEMAN, J. N. ; BARRON, K. V. and H. V. and Hedicke ; BLAU, W. J.: Morphological and mechanical properties of carbon-nanotube-reinforced semicrystalline and amorphous polymer composites. In: *Applied Physics Letters* 81 (2002), S. 5123–5125
- [108] GALIOTIS, C. ; YOUNG, R. J. ; YEUNG, P. H. J. ; BATCHELDER, D. N.: The study of model polydiacetylene/epoxy composites. In: *Journal of Materials Science* 19 (1984), S. 3640–3648
- [109] ASLOUN, E. M. ; NARDIN, M. ; SCHULTZ, J.: Stress transfer in single-fibre composites: effect of adhesion, elastic modulus of fibre and matrix, and polymer chain mobility. In: *Journal of Materials Science* 24 (1989), S. 1835–1844
- [110] CHAN, K. S. ; PAGE, R. A.: Creep damage development in structural ceramics. In: *Journal of the American Ceramic Society* 76 (1993), S. 803–826
- [111] LINCOLN, J. E. ; MORGAN, R. J. ; SHIN, E. E.: Fundamental investigation of cure-induced microcracking in carbon fiber/bismaleimide cross-ply laminates. In: *Polymer Composites* 22 (2001), S. 397–419
- [112] MUNCH, E. ; LAUNEY, M. E. ; ALSEM, D. H. ; SAIZ, E. ; TOMSIA, A. P. ; RITCHIE, R. O.: Tough, bio-inspired hybrid materials. In: *Science* 322 (2008), S. 1516–1520
- [113] ZHAO, Q. ; WOOD, J. R. ; WAGNER, H. D.: Stress fields around defects and fibers in a polymer using carbon nanotubes as sensors. In: *Applied Physics Letters* 78 (2001), S. 1748–1750
- [114] KATERELOS, D. G. ; GALIOTIS, C.: Axial strain redistribution resulting from off-axis ply cracking in polymer composites. In: *Applied Physics Letters* 85 (2004), S. 3752–3754
- [115] WEN, S. H. ; CHUNG, D. D. L.: Electrical-resistance-based damage self-sensing in carbon fiber reinforced cement. In: *Carbon* 45 (2007), S. 710 – 716
- [116] HU, N. ; KARUBE, Y. ; YAN, C. ; MASUDA, Z. ; FUKUNAGA, H.: Tunneling effect in a polymer/carbon nanotube nanocomposite strain sensor. In: *Acta Materialia* 56 (2008), S. 2929 – 2936
- [117] WANG, S. ; CHUNG, D. D. L.: Self-monitoring of strain and damage by a carbon-carbon composite. In: *Carbon* 35 (1997), S. 621 – 630
- [118] GAO, L. M. ; CHOU, T.-W. ; THOSTENSON, E. T. ; ZHANG, Z. G.: A comparative study of damage sensing in fiber composites using uniformly and non-uniformly dispersed carbon nanotubes. In: *Carbon* 48 (2010), S. 3788 – 3794

- [119] FROGLEY, M. D. ; ZHAO, Q. ; WAGNER, H. D.: Polarized resonance Raman spectroscopy of single-wall carbon nanotubes within a polymer under strain. In: *Physical Review B* 65 (2002), S. 113413
- [120] THOSTENSON, E. T. ; CHOU, T.-W.: Carbon nanotube networks: sensing of distributed strain and damage for life prediction and self healing. In: *Advanced Materials* 18 (2006), S. 2837–2841
- [121] PHAM, G. T. ; PARK, Y.-B. ; LIANG, Z. Y. ; ZHANG, C. ; WANG, B.: Processing and modeling of conductive thermoplastic/carbon nanotube films for strain sensing. In: *Composites Part B: Engineering* 39 (2008), S. 209 – 216
- [122] <http://www.expressindia.com/latest-news/glass-panel-falls-at-t3-close-shave-for-passengers/778605/>
- [123] <http://www.physorg.com/news192197798.html>
- [124] BRUNNER, B.: Sensor predicts glass breakage / Fraunhofer Institute for Silicate Research. 2010. – Forschungsbericht
- [125] ZHUANG, R. C. ; DOAN, T. T. L. ; LIU, J. W. ; ZHANG, J. ; GAO, S. L. ; MAEDER, E.: Multi-functional multi-walled carbon nanotube-jute fibres and composites. In: *Carbon* 8 (2011), S. 2683–2692
- [126] RYU, S.-W. ; KIM, C.-J. ; KIM, S. ; SEO, M. ; YUN, C. H. ; YOO, S. ; CHOI, Y.-K.: Fullerene-Derivative-Embedded nanogap Field-Effect-Transistor and its nonvolatile memory application. In: *Small* 6 (2010), S. 1617–1621
- [127] WHITNEY, J. M. ; DRZAL, L. T. ; JOHNSTON, N. J. (Hrsg.): *Toughened Composites ASTM STP 937*. Philadelphia, PA, USA : American Society for Testing and Materials, 1987. – 179 S.
- [128] RAMIREZ, F. A. ; CARLSSON, L. A. ; ACHA, B. A.: A method to measure fracture toughness of the fiber/matrix interface using the single-fiber fragmentation test. In: *Composites Part A: Applied Science and Manufacturing* 40 (2009), S. 679 – 686
- [129] EBBESEN, T. W. ; LEZEC, H. J. ; HIURA, H. ; BENNETT, J. W. ; GHAEMI, H. F. ; THIO, T.: Electrical conductivity of individual carbon nanotubes. In: *Nature* 382 (1996), S. 54–56
- [130] LI, C. Y. ; THOSTENSON, E. T. ; CHOU, T.-W.: Dominant role of tunneling resistance in the electrical conductivity of carbon nanotube-based composites. 91 (2007), S. 223114

- [131] WANG, H.-B. ; LI, S.-J. ; YU, T.-Y.: On the thermal behavior and mechanism of residual microstress buildup at the matrix interface in filled epoxy resins. In: *Polymer Engineering & Science* 33 (1993), S. 474–479
- [132] QIU, J. J. ; ZHANG, C. ; WANG, B. ; LIANG, R.: Carbon nanotube integrated multifunctional multiscale composites. In: *Nanotechnology* 18 (2007), S. 275708
- [133] CHU, X. X. ; WU, Z.X. ; HUANG, R. J. ; ZHOU, Y. ; LI, L. F.: Mechanical and thermal expansion properties of glass fibers reinforced PEEK composites at cryogenic temperatures. In: *Cryogenics* 50 (2010), S. 84 – 88
- [134] WARFIELD, R. W. ; PETREE, M. C.: Polymerization of a Thermosetting Polymer in an Electric Field. In: *Nature* 199 (1963), S. 67–68
- [135] WARFIELD, R. W. ; PETREE, M. C.: Dependence on temperature of the electrical resistivity of thermosetting polymers. In: *Nature* 187 (1960), S. 316–317
- [136] RWEI, F. H. S. P. and Ku K. S. P. and Ku ; CHENG, K. C.: Dispersion of carbon black in a continuous phase: Electrical, rheological, and morphological studies. In: *Colloid & Polymer Science* 280 (2002), S. 1110–1115
- [137] MILLER, B.: Polymerization behavior of silver-filled epoxy resins by resistivity measurements. In: *Journal of Applied Polymer Science* 10 (1966), S. 217–228
- [138] ZHANG, T. ; MUBEEN, S. ; MYUNG, N. V. ; DESHUSSES, M. A.: Recent progress in carbon nanotube-based gas sensors. In: *Nanotechnology* 19 (2008), S. 332001
- [139] YAMADA, T.: *Carbon nanotubes: science and applications*. Boca Raton London New York Washington, D.C : CRC Press, 2005. – 214 S.
- [140] FAVA, R. A. ; HORSFIELD, A. E.: The interpretation of electrical resistivity measurements during epoxy resin cure. In: *Journal of Physics D: Applied Physics* 1 (1968), S. 117
- [141] WARFIELD, R. W. ; PETREE, M. C.: Electrical resistivity of polymers. In: *Polymer Engineering & Science* 1 (1961), S. 80–85
- [142] ULBRICHT, H. ; MOOS, G. ; HERTEL, T.: Physisorption of molecular oxygen on single-wall carbon nanotube bundles and graphite. In: *Physical Review B* 66 (2002), S. 075404
- [143] ZHAO, J. J. ; LU, J. P. ; HAN, J. ; YANG, C.-K.: Noncovalent functionalization of carbon nanotubes by aromatic organic molecules. In: *Applied Physics Letters* 82 (2003), S. 3746–3748

- [144] WISANRAKKIT, G. ; GILLHAM, J. K.: The Glass Transition Temperature ( $T_g$ ) as an Index of Chemical Conversion for a High- $T_g$ , Amine/Epoxy System: Chemical and Diffusion-Controlled Reaction Kinetics. In: *Journal of Applied Polymer Science* 41 (1990), S. 2885–2929
- [145] ENNS, J. B. ; GILLHAM, J. K.: Time-temperature-transformation (TTT) cure diagram: Modeling the cure behavior of thermosets. In: *Journal of Applied Polymer Science* 28 (1983), Nr. 8, S. 2567–2591
- [146] SIMON, S. L. ; GILLHAM, J. K.: Reaction kinetics and TTT cure diagrams for off-stoichiometric ratios of a high- $T_g$  epoxy/amine system. In: *Journal of Applied Polymer Science* 46 (1992), S. 1245–1270
- [147] GALY, J. ; SABRA, A. ; PASCAULT, J.-P.: Characterization of epoxy thermosetting systems by differential scanning calorimetry. In: *Polymer Engineering & Science* 26 (1986), S. 1514–1523
- [148] WU, L. X. ; HOA, S. V. ; MINH-TAN ; TON-THAT: Effects of composition of hardener on the curing and aging for an epoxy resin system. In: *Journal of Applied Polymer Science* 99 (2006), S. 580–588
- [149] MEYER, F. ; SANZ, G. ; ECEIZA, A. ; MONDRAGON, I. ; MIJOVIC, J.: The effect of stoichiometry and thermal history during cure on structure and properties of epoxy networks. In: *Polymer* 36 (1995), S. 1407 – 1414
- [150] DUSEK, K. ; BLEHA, M.: Curing of epoxide resins: Model reactions of curing with amines. In: *Journal of Polymer Science: Polymer Chemistry Edition* 15 (1977), S. 2393–2400
- [151] PALMESE, C. R. ; MCCULLOUGH, R. I.: Effect of Epoxy-Amine Stoichiometry on Cured Resin Material Properties. In: *Journal of Applied Polymer Science*, 46 (1992), S. 1863–1873
- [152] KISSINGER, H. E.: Reaction Kinetics in Differential Thermal Analysis. In: *Anal.Chem.* 29 (1957), Nr. 11, S. 1702–1706
- [153] HE, Y.: DSC and DEA studies of under®ll curing kinetics. In: *Thermochimica Acta* 367-368 (2001), S. 101–106
- [154] DAVIES, D. K.: Carrier transport in polythene. In: *Journal of Physics D: Applied Physics* 5 (1972), S. 162
- [155] SPERLING, L. H. ; SPERLING, L. H. (Hrsg.): *Introduction to Physical Polymer Science, 4th Edition*. John Wiley and Sons, Inc, 2006
- [156] STROBL, G. R. ; STROBL, G. R. (Hrsg.): *The Physics of Polymers: Concepts for Understanding Their Structures and Behavior*. Springer, 2007

- 
- [157] MUTHUKUMAR, M. ; REITER, G. (Hrsg.) ; STROBL, G.R. (Hrsg.): *Progress in understanding of polymer crystallization*. Springer, 2006
- [158] COBURN, J. C. ; BOYD, R. H.: Dielectric relaxation in poly(ethylene terephthalate). In: *Macromolecules* 19 (1986), S. 2238–2245
- [159] GONNET, J-M. ; GUILLET, J. ; SIRAKOV, I. ; FULCHIRON, R. ; SEYTRE, G.: “In-situ” monitoring of the non-isothermal crystallization of polymers by dielectric spectroscopy. In: *Polymer Engineering & Science* 42 (2002), S. 1159–1170
- [160] WAN, X. J. ; LONG, G. K. ; HUANG, L. ; CHEN, Y. S.: Graphene – A Promising Material for Organic Photovoltaic Cells. In: *Advanced Materials* 23 (2011), Nr. 45, S. 5343–5358
- [161] DUNLOP, J. W. C. ; WEINKAMER, R. ; P., Fratzl: Artful interfaces within biological materials. In: *Materialstoday* 14 (2011), Nr. 3, S. 70–78

# Publication

## Journal

- Jie Zhang, Jianwen Liu, Rongchuan Zhuang, Edith Maeder, Gert Heinrich, Shanglin Gao. Single MWNT-Glass Fiber as Strain Sensor and Switch. **Advanced Materials**, 2011, 23, 3392-3397.
- Jie Zhang, Rongchuan Zhuang, Jianwen Liu, Edith Maeder, Gert Heinrich, Shanglin Gao. Functional interphases with multi-walled carbon nanotubes in glass fibre/epoxy composites. **Carbon**, 2010, 48, 2273-2281.
- Shang-lin Gao, Rong-Chuan Zhuang, Jie Zhang, Jian-Wen Liu, Edith Maeder. Glass Fibers with Carbon Nanotube Networks as Multifunctional Sensors. **Advanced Functional Materials**. 2010, 20, 1885-1893.
- Rong-chuan Zhuang, Thi Thu Doan, Jian-Wen Liu, Jie Zhang, Shang-Lin Gao, Edith Maeder. Multi-functional multi-walled carbon nanotube-jute fibres and composites. **Carbon**. 2011, 49, 2683-2692.

## Conference

- J. Zhang, S. L. Gao, E. Maeder, J. W. Liu. Multifunctional Intephase between MWNTs-glass fibre and epoxy matrix. European Center for Nanostructured Polymers. 2011
- J. Zhang, S. L. Gao, E. Maeder, G. Heinrich, J. W. Liu, R. C. Zhuang. Functional epoxy composites with mwnts-glass fibres. 18th international conference on composite materials. 2011.
- J. Zhang, S. L. Gao, E. Maeder, G. Heinrich. Glass Fibre with Carbon Nanotube Networks in Epoxy: Functional Interphase. Spring school Fulda DFG project SPP 1369. 2010.
- J. Zhang, S. L. Gao, R. C. Zhuang, J. W. Liu, E. Maeder, G. Heinrich. Deposition of multi-walled carbon nanotube coatings on glass fibre surfaces to functionalize glass fibre/epoxy interphases. International Conference on Functional Nanocoatings. 2010.



- S. L. Gao, R. C. Zhuang, J. Zhang, J. W. Liu, E. Maeder. Functional Nanocoatings with Carbon Nanotubes on Glass Fibre. International Conference on Functional Nanocoatings. 2010.
- R. C. Zhuang, S. L. Gao, T. T. L. Doan, J. Zhang, J. W. Liu, E. Maeder. Jute Fibres and Composites with Multifunctional Sensing Capability. 7th Asian-Australasian conference on Composite Materials. 2010
- J. Zhang, S. L. Gao, R. C. Zhuang, J. W. Liu, E. Maeder. Carbon nanotube coatings on glass fibre surfaces for modifying glass fibre/epoxy interphases structure and adhesion strength. DFG program SPP 1369 conference. 2009.
- S. L. Gao, R. C. Zhuang, J. Zhang, J. W. Liu, J. Rausch and E. Maeder. Carbon nanotube network on glass fibre as multifunctional sensor. 4th China-Europe Symposium on Processing and Properties of Reinforced Polymers. 2009
- S. L. Gao, R. C. Zhuang, J. Zhang, J. W. Liu, E. Maeder. Glass fibre with carbon nanotube networks as multifunctional sensor. 17th international conference on composite materials. 2009.
- E. Maeder, S. L. Gao, J. Rausch, R. C. Zhuang, J. Zhang, J. W. Liu, C. Schefler, R. Plonka. Multifunctional effects by nanostructured interphases. DFC-10 Deformation and Fracture of Composites Conference. 2009.
- S. L. Gao, R. C. Zhuang, J. Zhang, J. W. Liu, J. Rausch, E. Maeder. in Proc. Euradh 2008/Adhesion 2008.